PHONON CONDUCTIVITY METRICS FOR COMPACT, LINKED-CAGE,
LAYERED, AND FILLED-CAGE CRYSTALS, USING AB INITIO,
MOLECULAR DYNAMICS AND BOLTZMANN TRANSPORT TREATMENTS

by

Baoling Huang

A dissertation submitted in partial fulfillment
of the requirements for the degree of
Doctor of Philosophy
(Mechanical Engineering)
in the University of Michigan
2008

Doctoral Committee:

        Professor Massoud Kaviany, Chair
        Professor Jasprit Singh
        Professor Ctirad Uher
        Assistant Professor Anton Wan der Van

Acknowledgements

When I first came to University of Michigan, Ann Arbor, I knew my life would be changed completely. The experience in the following years confirmed my presentiment. My knowledge, working custom, and philosophy have been changed significantly for better suitability with academic research and life in United States. When I recall those people who have contributed directly or indirectly to my research and those who have affected and been affecting my life and attitudes, I am thankful to many. First of all, my advisor, Professor Massoud Kaviany, provided me with continuous and unconditional support and motivation through these years. He opened the door of a new academic field for me and taught me many great things, including working attitudes, social communications, and research philosophy. I acknowledge him for his kindness, patience, willingness to help me in any field. Professor Ctirad Uher taught me the co-evaporation techniques for thin films and the techniques for the measurement of phonon and electron transport properties. Professor Anton Van der Van has provided many insightful comments and suggestions to my research. Professor Jasprit Singh, Eitan Geva, Leopoldo A Pando Zayas taught courses that were very helpful to me for learning about quantum mechanics and solid state physics.

Professor Michael Falk helped me to understand some problems on molecular dynamics. Doctor Kai Sun introduced SEM technique to me. I am also thankful to the administrative staffs of the Department of Mechanical Engineering, Laura Elgas, Kelly Talcott, and Cynthia Quann-White, who have been a constant and reliable source of help.

Time flies away without being noticed. I have been in the research group for four years and become a senior member. This period is a happy time for me, because I have met many great people here. Some get along with me for a long time and become my great friends. Some just have come into my life and research and then gone. But all of them are important for me. I have always benefited from their knowledge, innovation, patience and selflessness. Particularly, Alan J.H. McGaughey helped me to learn molecular dynamics simulations and gave me many insightful suggestions. Luciana W. da Silva taught me the co-evaporation techniques for films. Xiulin Ruan had a lot of very helpful discussion with me about solid state physics. Brendan O'Connor helped me to modify my manuscripts. Yanbin Chen helped me with SEM techniques. Of course, I would also like to make a grateful acknowledgement for my wife (Yue Xiang), my son (Andy Huang), my parents and my parents-in-law. Their support is very essential for my study and research.

Table of Contents

List of Figures

x

List of Tables

List of Appendices

Nomenclature

a mean atomic distance, potential parameter

b constant

c concentration

c_v heat capacity per volume

d distance

e_c charge of electron

f distribution function

g perturbation of distribution

h Planck constant

k thermal conductivity

k_{B} Boltzmann constant

l distance, length

m mass

n number density

P pressure

q charge

r	distance
s	bond order
$\mathbf{s}$	unit vector
t	time)
$\mathbf{u}$	velocity, displacement
u, v	lattice parameter)
$\dot{w}$	heat current
z_e	effective atomic charge
A	coefficient, cross area
B	coefficient
C	coefficient
C	elastic constant
D	density of states, diameter
$\mathbf{D}$	force matrix
E_p	bulk modulus
E_Y	Young's modulus
E	energy
$E_{e,g}$	band gap
E_F	Fermi energy
$\boldsymbol{G}$	reciprocal lattice vector
H	height
H	Hamiltonian

I	spectral density
J	current
K	force constant
$\mathbf{K}_p$	thermal conductivity tensor
$\mathbf{M}$	dipole moments
M	atomic weight
$\mathbf{M}$	interaction matrix
N	number of particles, atomic number, valley number
N_c	number of atoms in a primitive cell
N_{L}	Lorenz constant
Q	heat flow
$\mathbf{R}$	position vector
R_c	cut-off radius
T	temperature
V	volume
Z	figure of merit

Greek symbols

α_{S}	Seebeck coefficient
β	Wolf method parameter, thermal expansion coefficient
χ	electronegativity
δ	average diameter of atoms

ϵ	emissivity
ε	deviation
γ_{G}	Grüneisen constant
$\dot{\gamma}$	transition rate
Γ	force constant
$\hbar$	Plank constant
κ	wave vector
κ_s	compressibility
λ	mean free path, screening distance
μ	chemical potential
ν	Poisson ratio, phonon frequency
ω	angular frequency
σ	Stefan-Boltzmann constant
σ_e	electrical conductivity
$\dot{\omega}$	heat current
ρ	density
ρ_e	electrical resistivity
τ	relaxation time
φ	potential energy, voltage

Subscripts

a	atomic

att	attractive
b	grain boundary, bound
A	average
A	acoustic
c	cell, cut-off, carrier
d	defects
e	equilibrium, effective, electron
ch	chromel
con	constantan
cov	covalent
cu	copper
C	coulomb
C-P	Cahill-Pohl
D	Debye
eq	equivalent
ext	external
g	group
h	heater, hole
i	summation index, particle label
ion	ionic
j	summation index, particle label
lg	long-range

loss	loss
max	maximum
L	longitudinal
O	optical
p	phonon
PO	polar optical phonon
rep	repulsive
sh	short-range
T	transversal
U	U process
v	vacancy
κ	wave vector
α	polarization
β	species
$\perp$	vertical
$\parallel$	parallel
θ	bond angle
φ	torsion angle

Superscripts

*	complex conjugate
$\sim$	deviation from average value

Abbreviations

BCC	body-centered cubic
BDC	benzenedicarboxylate
BTE	Boltzmann transport equation
CBE	conduction band edge
DFT	density functional theory
DOS	density of states
PDOS	partial density of states
FCC	face-centered cubic
FAU	faujasite
G-K	Green-Kubo
GGA	generalized-gradient density approximation
HVB	highest valence band
HCACF	heat current autocorrelation function
IR	infrared
LAPW	full potential, linearized augmented plane-wave method
LCB	lowest conduction band
LDA	local density approximation
LO	local orbital
LTA	zeolite A
L-J	Lennard-Jones

MD   molecular dynamics

MOF   metal organic framework

NIR-FT Near InfraRed-Fourier Transform

PZ   Perdew-Zunger

RFT   response function theory

RMS   root mean square

SO   spin-orbit

SOD   sodalite

TE   thermoelectric

Chapter 1

Introduction

1.1 Structure Metrics and Thermal Design

The lattice thermal conductivities of crystals are of both practical and theoretical importance. They are essential for reliability and performance of energy conversion systems, thermal insulators and conductors, microdevices, and microelectronic systems. For example, in thermal insulators and thermoelectric low thermal conductivity is desired while in other electronic devices high thermal conductivity is desired. The lattice conductivity is often obtained by the measurements of bulk crystals. However, some crystals, such as zeolites, cannot be grown large enough for a direct measurement, and their thermal conductivities are often extracted from indirect measurements with large uncertainty [25]. Furthermore, to synthesize a new material with the desired thermal properties, or to improve the performance of existing materials, a fundamental understanding of thermal transport in the crystals (and its relation to the atomic structure) is needed. Though the thermal transport properties of materi-

als have been studied for a long time, the correlations between the thermal transport properties and the structures are not very clear yet. How does the structure of a material affect the thermal transport? And how can we design a new material with desired thermal transport properties? These questions are being raised more and more often with the fast development in thermal management, thermoelectrics, and micro electro-mechanical systems. However, so far no general attempt has been made on the structural metrics of phonon conductivities of crystals. The recent progress in experimental techniques, and more importantly the exponential advancement in the quantum mechanical computation techniques in recent decades, have begun to offer the possibility examining the interactions occurring in the microscale and the transportation of energy carriers in the atomic structure.

1.2   Thermal Conduction in Solids

Thermal conduction in solids is traditionally described by the Fourier law of conduction, which is a phenomenological law and assumes the heat flux is proportional to the temperature gradient ∇T, i.e.,

$$\boldsymbol{q}_k \equiv \boldsymbol{K} \cdot \nabla T, \tag{1.1}$$

where $\boldsymbol{q}_k$ is the conduction heat flux, $\boldsymbol{K}$ is the thermal conductivity tensor. Then, the conduction thermal transport is direct determination of the thermal conductivity tensor $\boldsymbol{K}$, which is generally considered as an inherent property of the materials only. However, when the dimenstion of material becomes small (about 100 nm), $\boldsymbol{K}$ also depends on the dimensions and structures. The limits of the Fourier law is due to its

macroscopic nature and its validity is based on the following assumptions [26, 27]:

(1) the system can be modeled as a continuum;

(2) the heat carrier transport is diffusive and the heat carriers can be fully scattered by other carriers before they can reach the boundary or interface of the system;

(3) the relaxation time is much shorter than the system transition time;

(4) non-linearity is negligible when a temperature gradient is applied.

The first two conditions are normally violated at small dimension scales and low temperatures. The third condition is violated in fast transient phenomena, while the fourth condition can be violated when a large temperature gradient is applied. At small length or short time scales, more fundamental approaches are necessary, e.g., the Boltzmann transport equations (BTE), Monte Carlo (MC) method, or molecular dynamics (MD) simulations. Dealing with the atoms and energy carriers, these methods also offer the ability to investigate the thermal transport at the atomic level and at short times, and are extremely useful in understanding the relationship between atomic structure and thermal conductivity.

Heat is transferred by energy carriers moving in a system. There are 4 types of energy carriers, i.e., phonons (lattice vibration treated as quasi-particles), electrons, fluid particles, and photons (classical electromagnetic wave treated as quasi-particles). Phonons or electrons dominate heat transfer in solids. In insulators, phonons are the only energy carriers; in metals or semiconductors, both phonons and electrons contribute to the thermal transport but electrons are overwhelming in metals while phonons are normally dominant in semiconductors. This work mainly focuses on the heat transfer by phonons, while Chapter 4 also deals with the thermal transport by

electrons.

In classical mechanics, lattice vibration can be decomposed as a superposition of normal modes of vibration. A phonon is a quantum of lattice vibration due to the collective movement of atoms in solids. It is a quasi-particle treatment of the lattice vibration wave characterized by frequency and wavelength; therefore, phonons do not have mass but have energy and momentum. A phonon mode is characterized by the frequency ω and wave vector $\boldsymbol{\kappa}$ of the corresponding vibration wave. This definition correlates phonon with crystalline materials. In amorphous materials, there exists no long-range periodicity even though there may be some short-range periodicity, and the wave vector $\boldsymbol{\kappa}$ is no longer a good quantity to describe the vibrations. However, the atomic vibrations in amorphous materials can still be decomposed into a superposition of a series of normal modes of vibration and the energy exchange of each mode is also quantized. Thereafter, normally the "phonon" concept can still apply for amorphous material, but in this treatment, phonons only have energy. As a quasi-particle, phonons are said to possess zero spin and be bosons, i.e., in a thermal equilibrium phonons follow the Bose-Einstein distribution

$$f_p^{\circ} = \frac{1}{e^{E_p/k_{\mathrm{B}}T} - 1}, \tag{1.2}$$

where $E_p = \hbar\omega$ is the energy of phonon, k_{B} is the Boltzmann constant.

The vibrations of neighboring atoms may be in phase or out of phase, resulting in the acoustic and optical phonons (denoted with subscript A and O, respectively). Normally the optical phonons have a small group velocity and contribute little to the thermal transport. So many models only consider the transport of acoustic phonons

[2]. When phonons move in a crystal, they may suffer scatterings by other phonons (Umklapp processes), and by electrons, grain boundaries, impurities and imperfections. The scatterings by the last three mechanisms significantly depend on the sample quality. To be more general and also useful for thermal material design, this work mainly concentrates on thermal transport limited by interphonon scatterings.

Electron is a charged subatomic particle. Electron is a fermion with a spin of $1/2$ and follows the Fermi-Dirac distribution

$$f_e^\circ = \frac{1}{e^{(E_e - \mu)/k_{\mathrm{B}}T} + 1},$$ (1.3)

where μ is the chemical potential. In good electrical conductors, the thermal conductivity contribution from electrons relates to the electrical conductivity by the Wiedemann-Franz law, where the ratio of electrical thermal conductivity and electrical conductivity is proportional to temperature. The prefactor for this proportionality depends on the Fermi energy, as will be discussed in Chapter 3. The scattering mechanisms for electrons are mainly scattering by phonons, other electrons, ionic charge, grain boundaries, defects, and imperfections. At high temperatures, for moderately doped semiconductors, the electron-phonon scattering dominates the electrical thermal transport.

1.3 Length, Time and Temperature Scales for Investigation

A thermal system can be characterized by its length, time and temperature scales. For phonons, there are four length scales [27]:

(1) the wavelength of the energy carrier Λ;

(2) the wave packet size l of the carrier;

(3) the mean free path of the carrier λ;

(4) the system size L.

This thesis investigates the thermal conductivity structure metrics based on Eq. (1.1). Therefore, first the system must be large enough to be described as a macroscopic system, i.e., $L \gg \lambda$; second, the thermal transport is described in terms of energy carriers, e.g., phonons, as discussed by McGaughey and Kaviany [28], the phonon particle treatment is only valid when $\lambda > l > \Lambda$; third, this thesis only deals with the steady state thermal transport and no transient phenomenon is considered. Furthermore, infinitely small temperature gradient is assumed and the linear response function theory is adopted, e.g., Green-Kubo fluctuation-dissipation theory.

This thesis concentrates on thermal transport at moderate or high temperature range (typically higher than 1/5 of the Debye temperature), where there occur a large range of applications. So, even though some quantum language or tools are used in the thesis, the systems considered are generally of classical nature.

1.4   Thermal Materials

Bulk single crystals can be divided into two major categories:
1) compact crystals, e.g., NaCl and diamond, which has a simple basis and there is no functional microstructure in the lattice. Due to their simplicity and wide property range, they are normally the most common crystals in various fields;
2) micro-structured crystals, which has a complex basis or special bond arrangement and the resulting internal microstructure, e.g., large cage, lamina, etc. These crystals normally have special transport properties due to their unusual structures.

We are interested in both categories. Specially, in the second category, we consider layered, linked-cage, and cage/filled-cage crystals, which constitute a major part of the second category. The layered crystals consist of layers (e.g., graphite and Bi_2Te_3), while cage crystals consist of interconnected cages (e.g., skutterudites and clathrates). The linked-cage crystals consist of a cage linked by long bridges, such as metal-organic frameworks (MOFs) and zeolites. The linked-cage crystals, e.g., MOFs, are promising in hydrogen storage, and the layered and filled-cage semiconductor crystals are important in low- and high-temperature thermoelectricity.

Figure 1.1 shows the room-temperature phonon conductivities of some crystalline solids in the four categories, namely compact, layered, linked-cage, and cage/filled-cage, with respect to density. From Fig. 1.1, the range of thermal conductivities and densities for compact crystals is very wide. The cross-plane thermal conductivities of layered crystals are normally low (of the order of 1 W/m-K) while the in-plane thermal conductivities are much higher. The linked-cage crystals, such as MOFs,

7
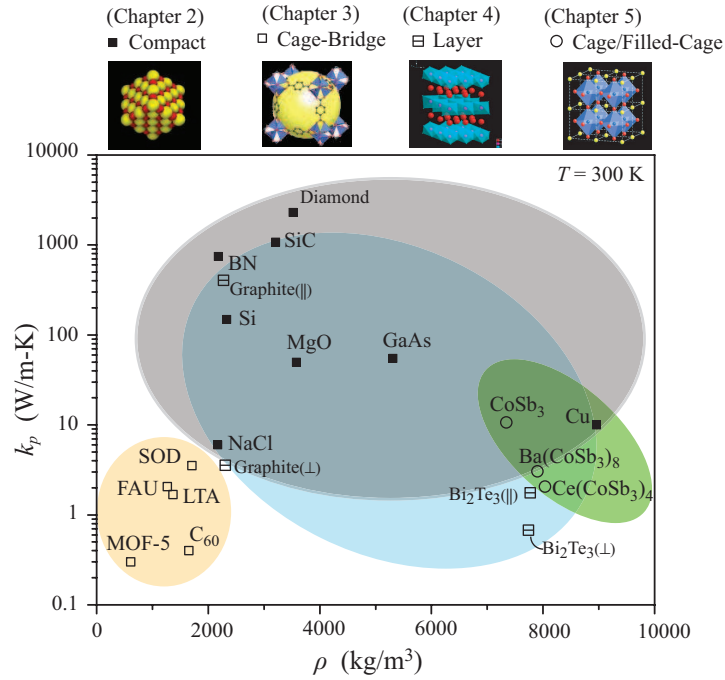
Figure 1.1: Experimental phonon conductivity of some crystalline solids with respect to their density at $T = 300$ K. The values for metals are derived by subtracting the electronic contribution from the total thermal conductivity.

zeolites, generally have low thermal conductivities as well as low density. The cage crystals have a relatively low thermal conductivity, while the values for the filled-cage crystals are significantly lower. Figure 1.1 does suggest some correlation between the crystalline structure and its phonon conductivity, for example, materials with large density normally have a low thermal conductivity while materials with too low a density also have a very low phonon conductivity. However, without insight into the atomic structure and how it affects the phonon transport, it is very hard to predict phonon conductivity and suggest thermal material design.

1.5 Thermal Transport Investigation

The common approaches for investigating the phonon conductivity in a crystal fall into three categories, all of which are based on the Fourier law.

The first approach for predicting the phonon conductivity is to use an atomistic technique, such as molecular dynamics (MD) simulations. MD requires only the inputs of the configuration of atoms and suitable interatomic potentials. It is in principle a very fundamental method and often used as a tool for understanding thermal transport, in some cases the prediction using MD agree well with experiments (at relatively high temperatures) [29, 30, 31]. However, accurate interatomic potentials are vital for MD, and the potentials used in MD are often obtained by fitting to *ab initio* calculations or to experimental results for bulk properties, which is often very challenging, especially for complex polyatomic crystals [32]. Also, MD is often very cumbersome and time-consuming, and the numerical results generally cannot provide much explicit information for the structure design and optimization. Furthermore, classical MD assumes all the phonon modes are excited, so they are invalid at very low temperatures where the quantum effects become important.

The second approach is to use the continuum transport theory and the kinetic theory, such as the Boltzmann transport equation (BTE) approach of Callaway [33] and Holland [34]. These approaches use the relaxation time approximation and the phonon concept, and can be used to predict the phonon transport in systems with wide range of dimension and temperature rather quickly. The expressions are relatively simple and can analytically illustrate some key quantities that affect the phonon transport.

9

As mentioned in Section 1.2, these methods are valid as long as the requirement for the quasi-particle treatment of vibrations is satisfied. On the other hand, they require a good understanding of the underlying phonon scattering processes. Many such approaches have some parameters that must be obtained empirically, e.g., by fitting to the experimental data or the results of more fundamental calculations[33, 34, 35]. Therefore they are very useful to analyze the thermal transport of known samples, but are not suitable for the prediction or design of new materials.

The third method is similar to the second one, but it seeks for the analytical expressions for the relaxation time models and tries to reduce the inputs. In this way, the effects of some structure parameter can be included explicitly and the results are more general. The modelling for relaxation times needs the fundamental and thorough understanding of the scattering process and is often extremely challenging. Some assumptions often have to be made to simplify the model.

This work adopts a multiscale approach, which involves all the three approaches together with the first principle calculations. Because MD simulations allow insight into the nature of phonon transportation at atomic level on a standard platform and the effects of different structure parameters can be decoupled and studied individually in simulations, we choose MD simulations along with the Green-Kubo method as the major approach for the atomic-level thermal transport investigation. The interatomic potentials are mainly fitted with the energy surface calculated by *ab initio* calculations. Phonon spectrum techniques and continuum models are used for the data analysis and the construction of structural metrics of phonon conductivity.

1.6 Methodology

1.6.1 Force Field Development

Appropriate interatomic force field are vital to the MD simulations. It determines the quality of the MD simulation results as well as the efficiency of the calculation. Normally the interatomic potentials are obtained empirically, i.e., fitted with available experimental results. This procedure is more or less an art rather than a science, since the available experimental results are normally few and the choice of appropriate macroscale properties is also a challenge. It is difficult to obtain the force field that can be used to predict all the macroscopic properties accurately. It is normal that the force field fitted with some macroscopic experiment results can predict some related quantities quite well, but fail in estimating some quantities that are physically different from the data used in the fitting procedure. So, for fitting with the experimental results, one has to choose the relevant data set very carefully. An alternative approach is to fit the interatomic potentials with the energy surface or other microscopic/macroscopic properties from the first-principle calculations. In many fields, the first-principle calculations are reliable and are often regarded as "numerical experiments". Using first-principle calculations may avoid some system errors or unexpected interference and noise, e.g., the impurity or imperfection in the samples, and sometimes are even more accurate than some experimental results in the literature. Fitting interatomic force field based on the first principle calculations is relatively more flexible and insightful, for example, one can arbitrarily move atoms and obtain the entire energy surface, or change some atoms while keeping the lattice
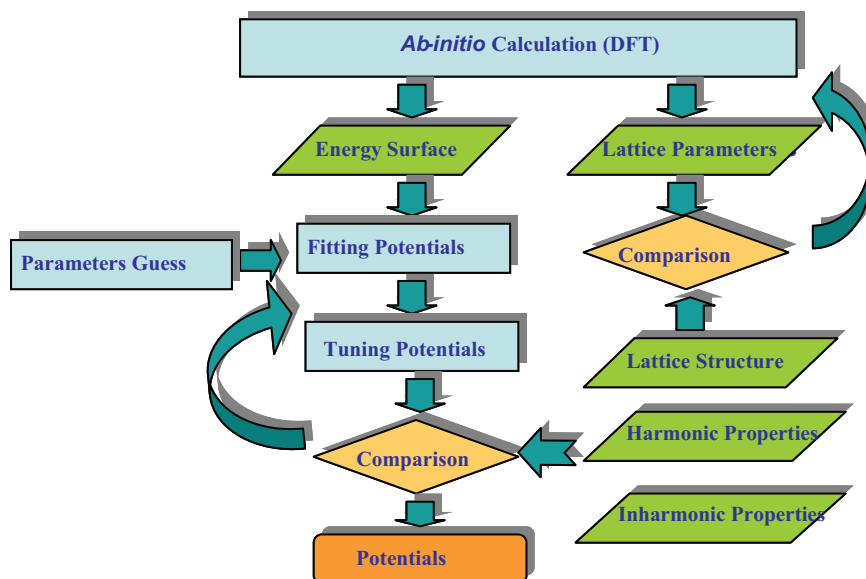
Figure 1.2: Strategy to develop the potentials required by molecular dynamics simulation from the *ab initio* calculations.

structure unchanged, or obtain some information from a new structure or even an imaginary structure. Also, all the data are obtained on the same platform and should be consistent. Furthermore, one may be able to obtain far more data or information than the available experimental results. In one word, the first-principle calculations offer the ability to fit the force field more accurately with much less limitations and the ability to gain insight into the atomic structure, compared with the traditional fitting with experimental results.

This work adopts the force-field fitting procedure based on the first-principle calculations. Figure 1.2 shows the strategy to develop the force field required in MD simulations, on the basis of the *ab initio* calculations. First, by moving different atoms along some specified direction, the energy surface of the structure is obtained from the *ab initio* calculations in the framework of Density Functional Theory (DFT).

Some presumed potential forms with initial parameters are then used as the first guess to fit the energy surface. During the fitting, the parameters as well as the potential forms are changed to reproduce the energy surface. Some experimental results or macroscopic properties calculated directly from DFT are also used to further check the fitted interatomic potentials. This procedure is repeated until the fitted force field converges.

1.6.2 Green-Kubo Method

In MD simulations the phonon conductivity can be computed either using nonequilibrium MD (NEMD) or equilibrium MD (EMD). The two most commonly applied methods for computing phonon conductivity are the "direct method" and the Green-Kubo (G-K) method.

The direct method closely resembles an experimental technique based on an application of the Fourier law[30]. The direct method is a steady-state, nonequilibrium method in which a steady 1-D heat flux is imposed on a system. From the resulting temperature gradient, the thermal conductivity is directly obtained using the Fourier law [Eq. (1.1)]. The direct method normally has strong nonlinear response behavior and significant size effects. Unless the simulation cell is many times larger than the mean free path, the scattering from the heat source and heat sink contributes more to the thermal resistivity than does the intrinsic anharmonic phonon-phonon scattering. Therefore, large atomic system are typically required to obtain an accurate prediction of the bulk phase thermal conductivity (it is better suited to the study of

thin films)[30]. For a complex crystal with a large unit cell (such as MOF-5), the computational demands would be tremendous.

The thermal conductivity limited by the phonon-phonon scatterings can also be determined using the G-K fluctuation-dissipation method, in which the thermal conductivity is related to the time decay of the heat current autocorrelation function (HCACF). The thermal conductivity tensor $\boldsymbol{K}_p$ is given by

$$\boldsymbol{K}_p = \frac{1}{k_{\mathrm{B}} V T^2} \int_0^\infty \langle \dot{\boldsymbol{w}}(t) \dot{\boldsymbol{w}}(0) \rangle, \tag{1.4}$$

where k_{B} is the Boltzmann constant, V is the volume of the simulation system, T is the system temperature, and $\langle \dot{\boldsymbol{w}}(t) \cdot \dot{\boldsymbol{w}}(0) \rangle$ is the HCACF. A slow-decaying HCACF indicates the heat current fluctuations can spread over a long time before vanishing, i.e., a long phonon relaxation time. The heat current $\dot{\boldsymbol{w}}$ is defined as

$$\dot{\boldsymbol{w}} = \frac{\mathrm{d}}{\mathrm{d}t} \sum_{i=1}^N \boldsymbol{r}_i E_i, \tag{1.5}$$

where $\boldsymbol{r}$ and E are the position vector and the total energy of a particle (atom) (excluding the site energy), respectively.

The G-K method has been used to investigate the thermal properties of dielectric materials such as diamond[31], silicon[30, 36], zeolites[29], and amorphous silicon[37]. This approach is based on fluctuation-dissipation theory and is an equilibrium method. The linear response behavior of the G-K method leads to accurate results using smaller atomic system than required in the direct method.[30] However, the HCACF normally converges very slowly compared with the direct method, and long correlation time and in turn more raw data are needed to obtain accurate results. The G-K method is also advantageous as it allows for the decomposition

of the thermal conductivity into contributions associated with acoustic and optical phonons[29]. This ability makes it possible to relate the structure parameters with phonon transportation and allows the comparison between different systems, so it is chosen for this work.

1.7 Objective and Scope of Thesis

The main objectives of this study is to develop an understanding of the structure metrics of thermal conductivity in dielectric and semiconductor crystals at the atomic level. A comprehensive, multiscale approach is developed for this investigation, which combines the first principle calculation, molecular dynamics (MD), Boltzman transport equations (BTE), and the kinetic theory.

The following chapters are divided based on the atomic structure of the solid, i.e., compact, layered, linked-cage, and filled-cage.

Chapter 2 develops an understanding of the structural metrics of high-temperature phonon conductivity for compact crystals. Based on the Slack model, an atomic structure-based model is developed and the relationship between the atomic structure and phonon transport is explored by modeling the Debye temperature T_{D} and the Grüneisen parameter γ_{G}. Under the assumption of homogeneous deformation, T_{D} is estimated according to a simplified force constant matrix and a phenomenological combinative rule for force constants, which is applicable to an arbitrary atomic pair. Also, γ_{G} is estimated from a general Lennard-Jones potential form and the combination of the bonds. The elemental electronegativity, element mass, and the

arrangement of bonds are found to be the dominant factors to affect the Debye temperature; while the elemental electronegativity and the arrangement of bonds are important in determining the anharmonicity. Based on this atomic-level model, the structural metrics of crystals with low or high lattice conductivity are discussed, and some strategies for thermal design and management are suggested.

Chapter 3 explores the phonon conductivity of a nanoporous, metal-organic framework (MOF) crystal with a phenylene bridge, MOF-5, over a wide temperature range using MD simulations and the G-K method. The force field for MOF is developed using *ab initio* calculations and experimental results. The temperature dependence of the thermal conductivity is discussed and analyzed. It is found that the mean free path of the majority of phonons in MOF-5 has a close relationship with the lattice parameter. To interpret the results, an analytical thermal conductivity relation is derived, which reduces to the Cahill-Pohl and Slack models under appropriate assumptions. A critical frequency is proposed, which determines the relative contributions of the short- and long-range acoustic phonons. The relationship between the long-range acoustic phonon contribution and the special linked-cage structure is discussed.

Chapter 4 investigates the phonon and electron transport in layered Bi_2Te_3 structure using a multiscale approach, combining the first-principle calculations, MD, and BTE. The MD simulations along with the Green-Kubo autocorrelation decay method are used to calculate the phonon thermal conductivity in both in-plane and cross-plane directions. The required classical interatomic potentials for Bi_2Te_3 are developed using the first-principle calculations and experimental results. The contributions from

the acoustic and optical phonons are identified and their dependence on temperature and polarization is discussed and modelled. The electrical transport is calculated using the full-band structure from the linearized augmented plane wave method, BTE, and the energy-dependent relaxation time models with the non-parabolic Kane energy dispersion. Temperature dependence of the energy gap is found to be important for the prediction of the electrical transport in the intrinsic regime. Appropriate modelling of relaxation times is also found to be essential for the calculation of the electrical and thermal transport, especially in the intrinsic regime. The maximum of the Seebeck coefficient is modelled by a simple expression containing the band gap. The electron scatterings by the acoustic, optical, and polar-optical phonons and the resulting electron thermal conductivity are discussed.

Chapter 5 continues to explore the phonon conductivity for caged $CoSb_3$ skutterudite and its filled structure. Both of the force field for the empty $CoSb_3$ structure and that for filled $CoSb_3$ are developed based on the first-principle calculations together with the response function theory. The interaction between the filler and the host is analyzed to clarify the role of the filler. Then the vibrational spectrum for both the empty and full-filled structure is explored. The MD simulation along with the G-K method is used to directly predict the phonon conductivity of the empty and filled structure. The effects of fillers are then analyzed and a solution model for the partially-filled structure is proposed.

In Chapter 6, the highlights of the work is summarized, and the future directions of related research are suggested.

Chapter 2

Atomic Structure Metrics for Phonon Conductivity of Compact Crystals

2.1 Slack Model

Starting from the derivation by Julian [38], in which the variational principle is used to obtain an analytical relaxation time for the rare-gas solids, Slack proposed that when heat is mainly carried by acoustic phonons scattered via the three-phonon process, the thermal conductivity of crystals with constant volume at high temperatures (normally above 1/4∼1/5 of the Debye temperature) can be given by the relation [39, 2]

$$k = \frac{3.1 \times 10^4 \langle M \rangle \delta T_{\mathrm{D},\infty}^3}{T \langle \gamma_{\mathrm{G}}^2 \rangle N_c^{2/3}}. \tag{2.1}$$

Here $\langle M \rangle$ is the mean atomic weight of the atoms in the primitive cell, δ^3 is the average volume per atom, $T_{\mathrm{D},\infty}$ is the high-temperature Debye temperature, T is the temperature, N_c is the number of atoms in a primitive cell, and $\langle \gamma_{\mathrm{G}}^2 \rangle$ is the mode-averaged square of the Grüneisen parameter at high temperatures. Note that $T_{\mathrm{D},\infty}$ used by Slack is extracted from the phonon density of states (DOS) D_p [2], i.e.,

$$T_{\mathrm{D},\infty}^2 = \frac{5h^2}{3k_{\mathrm{B}}^2} \frac{\int_0^\infty \nu^2 D_p(\nu)\mathrm{d}\nu}{\int_0^\infty D_p(\nu)\mathrm{d}\nu}, \qquad (2.2)$$

where h is the Planck constant, k_{B} is the Boltzmann constant, and ν is the phonon frequency. However, $T_{\mathrm{D},\infty}$ cannot be conveniently determined for it requires the information of DOS. Since the difference between $T_{\mathrm{D},\infty}$ and the Debye temperature T_{D} (at 0 K) extracted from the elastic constant or the measurement of heat capacity is normally small, it is customary to use T_{D} instead of $T_{\mathrm{D},\infty}$ in Eq. (3.10). Also $\langle \gamma_{\mathrm{G}}^2 \rangle$ is often replaced by $\langle \gamma_{\mathrm{G}} \rangle^2$ (later, for simplicity we use γ_{G} to denote $\langle \gamma_{\mathrm{G}} \rangle$), which can be determined from thermal expansion data at high temperatures.

Equation (3.10) is widely tested with pure non-metallic crystals and the overall agreement is good, even for complex crystals [39, 2]. The Slack relation illuminates how the atomic structure affects the thermal transport and provides a useful guide to tailoring the thermal transport properties.

McGaughey and Kaviany [29] showed that the lattice thermal conductivity can be decomposed into three parts:

$$k_p = k_{p,\mathrm{A},lg} + k_{p,\mathrm{A},sh} + k_{p,\mathrm{O}}. \qquad (2.3)$$

Here $k_{p,\mathrm{A},lg}$ is the contribution from long-range acoustic phonons, whose mean-free path is larger than one half of their wavelength; $k_{p,\mathrm{A},sh}$ is the contribution from

short-range acoustic phonons, whose mean-free path is minimized to one half of their wavelength; and $k_{p,\mathrm{O}}$ is the contribution from optical phonons. Our previous work [4], has pointed out that the Slack relation corresponds to $k_{p,\mathrm{A},lg}$ and is valid only when the short-range acoustic or optical phonons are not important. This condition is not always satisfied for crystals with low thermal conductivity, such as zeolites and metal-organic frameworks (MOFs). As will be discussed in Chapter 3, to identify the relative contributions of these different mechanisms, a critical angular frequency ω_c based on Klemens' model [4] is used, which is given as [4]

$$\omega_c \simeq \frac{2.37 \times 10^{-27} \langle M \rangle u_{p,g}^3}{3\pi^2 \delta \gamma_{\mathrm{G}}^2 k_{\mathrm{B}} T},\qquad(2.4)$$

where $u_{p,g}$ is the average phonon group velocity. The Slack relation is valid only when ω_c is comparable with the Debye frequency ω_{D} and long-range acoustic phonons dominate the thermal transport.

To use the Slack relation, T_{D} and γ_{G} must be known, which is the main difficulty in the estimation of the lattice conductivities of new materials. Since these two parameters directly relate the atomic structure to thermal transport, the knowledge of their relations provides more insightful information for the thermal design, and allows for the estimation of thermal transport properties of new materials.

In this work, we report a simple microscopic model to estimate T_{D} and γ_{G}. A phenomenological combinative rule for force constants is proposed, which can be used to derive the force constant of an arbitrary pair bond from the existing experimental data. Then a model for the phonon group velocity and the Debye temperature of complex crystals is derived on the basis of the dynamical matrix, in which the effects

of the lattice and bases are decomposed by the equivalent force constant. Using a general potential form for a bond, the Grüneisen parameters of different types of bonds are discussed, and then a relation for the equivalent Grüneisen parameter of the equivalent bond is developed, which can be applied for complex crystals. For linked-cage structures, where the Slack relation may not be applicable, a simple phonon mean-free path model based on the kinetic theory is also proposed, which shows good agreement with experiments and MD.

2.2 Combinative Rule for Force Constants of an Arbitrary Pair-Bond

The vibration energy is transferred in a crystal through interactions among the atoms, which can be theoretically calculated by quantum mechanical methods. However, a quantum mechanical method deals with the electron clouds of the atoms, and is very cumbersome for a system involving many particles. Based on the Born-Oppenheimer approximation [32], the force field method uses empirical potentials (fitted to experiments or quantum mechanic calculations), such as Lennard-Jones and Buckingham potentials, to describe the interactions in the system. In most solids, when the temperature is well below the melting point, the particles only slightly oscillate around their equilibrium positions and many of their behaviors (including the elastic behavior) can be well described in the framework of the harmonic approximation [14]. In this approximation, the energy of the system can normally be

decomposed into four terms corresponding to the bond stretching, bending, torsion and the non-bonded interactions [32], i.e.,

$$
\begin{aligned}
E \;=\; & \sum_i \frac{\Gamma_i}{2}(\Delta r_i)^2 + \sum_j \frac{\Gamma_{\theta,j}}{2}(\Delta \theta_j)^2 + \\
& \sum_l \frac{\Gamma_{\phi,l}}{2}(\Delta \phi_l)^2 + \sum_n \frac{\Gamma_{m,n}}{2}(\Delta r_{m,n}),
\end{aligned}
\tag{2.5}
$$

where Γ, Γ_θ, Γ_ϕ and Γ_m are the force constants of the bond length r, bond angle θ, torsion angle ϕ, and the distance between molecules r_m. Normally, the stretching interaction is much stronger than the other interactions (by a factor of more than ten), so for a rigid structure, the elastic characteristics are mainly determined by the stretching force constants. The bending and torsion interactions are also important for structure stability and deformation.

Since atomic interaction is determined by the electronic structure, potentials and force constants are expected to be transferable if the bond type and surroundings are similar [40]. Here we present a phenomenological combinative rule for the stretching and the van der Waals force constants.

The general form of two-body potentials can be written as

$$
\varphi_{AB}(r) = \varphi_{AB,rep}(r) - \varphi_{AB,att}(r),
\tag{2.6}
$$

where φ_{AB} is the potential energy of the bond A-B, and the subscripts rep and att represent the repulsive and the attractive terms. The repulsive term is due to the Pauli exclusion principle or the electrostatic interactions. It has been shown that the exchange repulsive term for two different atoms can be given as the geometric mean

of the corresponding terms for two pairs of equivalent atoms [41], i.e.,

$$\varphi_{AB,rep}(r) = [\varphi_{AA,rep}(r)\varphi_{BB,rep}(r)]^{1/2}, \tag{2.7}$$

The attractive term is due to the interactions of dipoles, electrostatics, or a combination of them. The exchangeability of the dipolar and electrostatic interactions is apparent, thus a similar combinative rule is suggested for the attractive term, i.e.,

$$\varphi_{AB,att}(r) = [\varphi_{AA,att}(r)\varphi_{BB,att}(r)]^{1/2}. \tag{2.8}$$

The potential near the equilibrium position can be described by the general Lennard-Jones (L-J) potential model

$$\varphi(r) = \frac{\alpha}{r^m} - \frac{\beta}{r^n}, \tag{2.9}$$

where m and n depends on the interaction type, and their values will be discussed in Section 2.4. The force constant Γ and the bond length r_0 at the equilibrium position are given as

$$\begin{aligned}
\Gamma &= -\frac{mn\varphi_\circ}{r_\circ^2} = \frac{m(m-n)\alpha}{r_\circ^{m+2}} = n(m-n)\beta(\frac{\beta n}{\alpha m})^{\frac{2+n}{m-n}} \\
r_\circ &= (\frac{\alpha m}{\beta n})^{\frac{1}{m-n}},
\end{aligned} \tag{2.10}$$

where $-\varphi_\circ$ is the potential energy at the equilibrium position. Equation (2.10) shows that the force constant at the equilibrium position is proportional to $\varphi_\circ$, when the bond type and the bond length are similar. Note that at the equilibrium position, the ratio of the magnitudes of the contributions from the repulsive term and the attractive term is $(m+1)/(n+1)$. Therefore, for $m \gg n$ (e.g, for ionic bond), the force constant is mainly determined by the repulsive term.

23

From Eqs. (2.7), (2.8) and (2.10), if Γ_{AA} is defined as the force constant of the potential function $\varphi_{AA}(r) = \varphi_{AA,rep}(r) - \varphi_{AA,att}(r)$, the force constant of A-B bond Γ_{AB} and its equilibrium bond length $r_{\circ,AB}$ can be given as

$$\Gamma_{AB} = (\Gamma_{AA}\Gamma_{BB})^{1/2}, \; r_{\circ,AB} = (r_{\circ,AA}r_{\circ,BB})^{1/2}. \qquad (2.11)$$

Note that for ions, the A-A bond may not actually exist. However, due to the similarity of the electronic configuration of the ions in different compounds, we may assign a virtual potential φ_{AA} to the ions, e.g., keeping the interaction due to Pauli exclusion principle as the repulsive term and setting the attractive term as $\varphi_{AA,att} = q^2/r$, where q is the ionic charge. The properties of the virtual potential (e.g., Γ_{AA}) can be extracted from the compounds. In this way, the combinative rule [Eqs. (2.7) and (2.8)] is still valid. Similar relations like Eq. (2.11) have been derived by Feranchuk et al. [42] using 12-6 L-J potential, but they did not consider the effects of bond order and the long-range electrostatic interactions. In addition, it is not appropriate to describe ionic bonds or covalent bonds using 12-6 L-J potential, as will be discussed later.

Note that this combinative rule is only applicable for the bonds with the same bond type (m and n are close) and bond order. In real compounds, a bond with the same atom configuration can have different bond orders. For example, C=O has the bond order of 2, and C-O has the bond order of 1. It is observed that the force constant is approximately proportional to the bond order [43], that is

$$\Gamma_{AB,s} = s\Gamma_{AB,1}, \qquad (2.12)$$

where $\Gamma_{AB,s}$ is the force constant of the bond between A and B with the bond order

24

of s. Thus Eq. (2.12) can be rewritten as

$$\Gamma_{AB,s} = s(\Gamma_{AA,1}\Gamma_{BB,1})^{1/2}. \tag{2.13}$$

Consequently, we have

$$\Gamma_{AC,s} = s\frac{(\Gamma_{AB,1}\Gamma_{BC,1})^{1/2}}{\Gamma_{BB,1}}. \tag{2.14}$$

According to Eq. (2.12), the potential energy φ can be assumed proportional to s, and r_e is expected to be independent of s. For ionic bonds, when this assumption is used, the resulting combinative rule for ionic bond length agrees well with the experiments (the error is less than 3%) [42]. However, this assumption is only moderately accurate for covalent bonds, because the L-J potential does not accurately describe the changes of electron clouds and the energy in the entire range of atomic distance. Generally, for covalent bonds, r_e will decrease slightly when s increases. Paolini [44] developed an empirical bond order-bond length relationship for covalent bonds

$$r_{e,s} = r_{e,1} - 0.78(s^{0.33} - 1), \tag{2.15}$$

where $r_{e,s}$ is the equilibrium bond length (in Angstrom) with the bond order of s. Equation (2.15) shows good agreements with the experimental results for many bonds [44] and can be used for the estimation of the bond length.

Table 2.1: Electronegativity, equilibrium bond length, and force constants of element pairs (list in order of atomic number) with the bond order of 1. The data are extracted from [1]. The symbols C and V represent covalent and van der Waals interactions, and the unlabeled are the values for ionic interactions.

Atom	χ	$r_{e,1}$, Å	Γ, N/m	Atom	χ	$r_{e,1}$, Å	Γ, N/m
H	2.20	0.74[C]	575.67[C]	Br	2.96	2.28[C]	250.83[C], 539.78
He	-	1.04[C]	411.74[C]	Kr	3.00	4.03[V]	1.43[V]
Li	0.98	2.67	25.48	Rb	0.82	3.79	8.25
Be	1.57	1.39	120.62	Sr	0.95	3.05	26.57
B	2.04	1.76[C]	354.90[C]	Y	1.22	-	70.05
C	2.55	1.54[C]	510.5[C]	Zr	1.33	8.41	141.43
N	3.04	1.46[C]	771.20[C]	Nb	1.60	2.36	108.25
O	3.44	1.46[C]	593.57[C] 1305	Ru	1.02	2.17	56.53
F	3.98	1.41[C]	473.82[C] 1960	Ag	1.93	2.59	59.09
Ne	-	3.10[V]	0.12[V]	Cd	1.69	4.28	44.93
Na	0.93	3.08	17.28	In	1.78	2.86	34.41
Mg	1.31	3.89	41.60	Sn	1.96	2.80	58.34
Al	1.61	2.47	49.15	Sb	2.05	2.82[C]	70.64[C]
Si	1.90	2.34[C]	109.04[C]	Te	2.10	2.74[C]	119.46[C]
P	2.19	2.20[C]	201.50[C]	I	2.66	2.66[C]	172.73[C] 343.06
S	2.58	2.08[C]	250.65[C] 536.92	Xe	2.60	4.36[V]	1.74[V]
Cl	3.16	1.98[C]	330.42[C] 705.81	Cs	0.79	4.47	6.97
Ar	-	3.76[V]	0.80[V]	La	1.10	2.83	53.41
K	0.82	3.90	9.84	Ce	1.12	2.74	169.30
Ca	1.00	4.28	34.61	Pr	1.13	-	48.25
Sc	1.36	2.40	77.60	Eu	1.20	-	31.11
Ti	1.54	2.17	107.71	Tb	1.10	-	72.63
V	1.63	2.09	103.03	Ho	1.23	3.11	77.21
Cr	1.66	2.17	87.18	Yb	1.10	2.89	33.74
Mn	1.55	2.59	46.40	Lu	1.27	2.63	78.69
Fe	1.83	2.04	62.53	Hf	1.30	2.44	103.98
Co	1.88	3.20	116.61	Ta	1.50	2.36	179.07
Ni	1.91	2.96	130.00	W	2.36	-	202.54
Cu	1.90	2.22	65.82	Ir	2.20	2.36	110.01
Zn	1.65	3.41	81.15	Au	2.54	2.47	106.80
Ga	1.81	2.43	99.38	Hg	2.00	3.30	32.61
Ge	2.01	2.16	121.79	Tl	1.62	3.07	31.60
As	2.18	2.42	120.48	Pb	2.33	3.03	39.91
Se	2.55	2.34[C]	108.54[C]	Bi	2.02	3.07	49.08
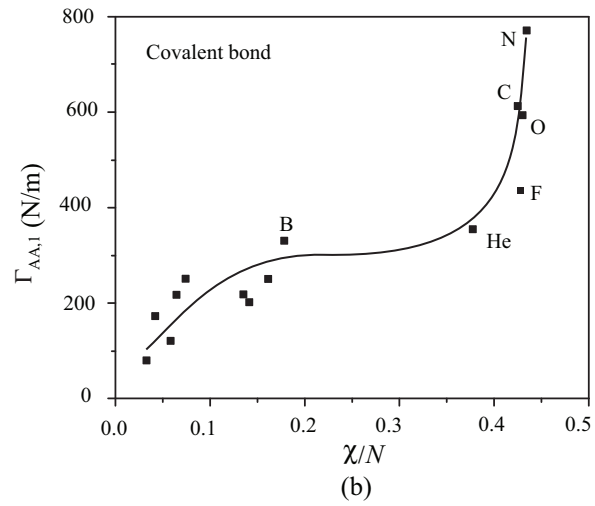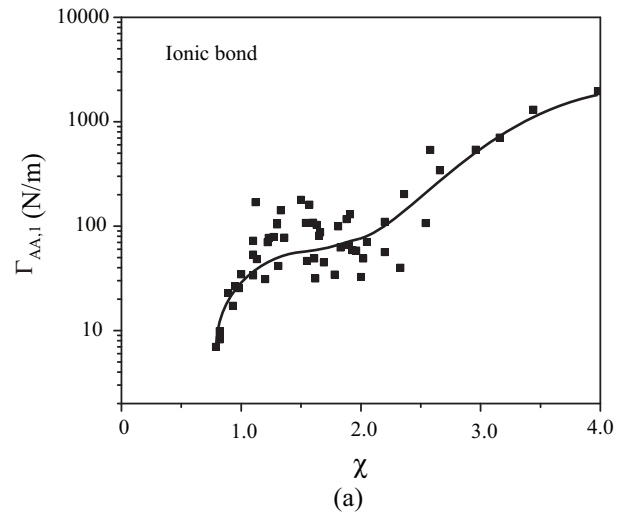
Figure 2.1: (a) Variation of calculated ionic force constant $\Gamma_{AA,1}$ with respect to the electronegativity. (b) Variation of the calculated covalent force constant $\Gamma_{AA,1}$ with respect to the ratio of the electronegativity and atomic number. The data are extracted from the spectra of diatomic molecules [1]. The lines are used to guide the eyes.

Table 2.1 lists the force constant $\Gamma_{AA,1}$, electronegativity χ, and equilibrium bond length $r_{e,1}$. $\Gamma_{AA,1}$ is extracted from the experimental spectra of diatomic molecules [1] according to Eqs. (2.13) and (2.14) [the ionic $\Gamma_{AA,1}$ of elements, e.g., O and S, is an average of the values extracted from their compounds]. $r_{e,1}$ is extracted from the bond lengths of the diatomic molecules [1]. Table 2.1 shows that $\Gamma_{AA,1}$ of ionic bonds for the elements with high electronegativity χ (e.g., O and Cl) are normally twice that of the corresponding covalent bond. This indicates that the virtual potential of ions is steeper than the covalent potential of the corresponding atoms near the equilibrium position. The electronegativity χ can be used to determine the bond type. Bonds between atoms with a large electronegativity difference (≥ 1.7), are usually considered to be ionic, while values between 1.7 and 0.4 are considered polar covalent, and values below 0.4 are considered non-polar covalent bonds [45]. For metallic elements, even though $\Delta\chi$ is small, their electron structures are similar to those in the ionic crystals, for the conduction electrons can move about [46].

Figure 2.1(a) shows that generally the ionic $\Gamma_{AA,1}$ increases as the electronegativity increases. The alkali metals have the lowest $\Gamma_{AA,1}$, while the halogen elements have the highest $\Gamma_{AA,1}$. When $1.0 < \chi < 2.5$, most transition metal elements and semiconducting elements have a $\Gamma_{AA,1}$ around 50 N/m, which is a relatively low value. In general, $\Gamma_{AA,1}$ decreases while the atomic radius increases. However, Fig. 2.1(b) shows for covalent bonds $\Gamma_{AA,1}$ seems to relate to the ratio of χ/N (N is the atomic number) rather than χ. Nitrogen has the highest covalent $\Gamma_{AA,1}$.

Figure 2.2 compares the experimental results of some bonds in diatomic molecules along with the calculated values. The mean square error is less than 8%, and the

overall agreement is good.
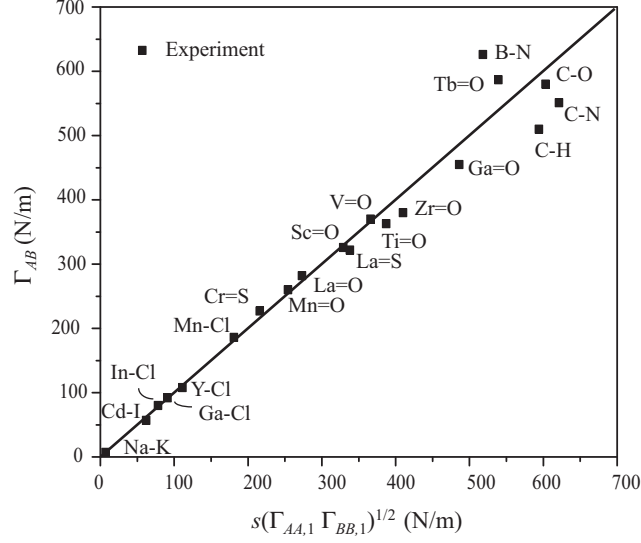
Figure 2.2: Comparison of calculated force constants and the corresponding values from the experimental spectra, for some atomic pairs [1].

Note that the above force constants and equilibrium bond lengths are derived from the data of gaseous diatomic molecules, where the intermolecular effects are negligible. For crystal bonds, long-range interactions (mainly electrostatic interactions) from the surroundings may significantly affect the equilibrium bond length and force constant. For example, Na-Cl in a NaCl molecule has a force constant of 110 N/m and a bond length 2.36 Å[1], while the distance between the nearest Na and Cl ions in a NaCl crystal at $T = 300$ K is 2.83 Å, and the effective force constant of each Na-Cl pair derived from the bulk modulus is only 20 N/m [47]. Thus, a relation between the force constant of a bond in a gaseous diatomic molecule and that in a crystal must be developed to account for the effects of long-range interactions. Here, only the effect of electrostatic interactions is considered. Our approach is to include long-

29

range interactions in an effective bond potential of the nearest neighboring atoms. A bond (in a diatomic molecule) with a form in Eq. (2.9) is considered. Since the repulsive term is a very short-range interaction, we assume only the long-range attractive term is affected by the surroundings. This effective bond in a crystal can then be represented as

$$\langle\varphi\rangle(r) = \frac{\alpha}{r^m} - \eta\frac{\beta}{r^n}, \tag{2.16}$$

where η is the correction factor due to the long-range interactions (in simple ionic structures, it is related to the Madelung constant). However, η is difficult to determine for complex crystal structures. In practice, according to this assumption and Eq. (2.10), the force constant of the bond in the crystal Γ'_{AB} can be simply calculated as

$$\Gamma'_{AB} = \Gamma_{AB}(\frac{r_\circ}{r'_\circ})^{m+2}, \tag{2.17}$$

where Γ_{AB} is the force constant of the bond in the diatomic molecule AB, and $r'_\circ$ is the equilibrium bond length in the crystal. For example, for NaCl, by setting $m = 6.3$ [using the approximation method Eq. (2.36)], and using the above bond length data, we have $\Gamma'_{\text{NaCl}} = 110 \times (2.36/2.83)^{(6.3+2)} = 24$ N/m, which is very close to 20 N/m derived from the bulk modulus [47]. For ionic bonds, m is large, and Eq. (2.17) indicates that Γ'_{AB} is very sensitive to the values of $r_\circ$ and r'_o, so the experimental values of r_o and r'_o will be preferred. When the experimental value of r_o is unavailable, the combinative rule [Eq. (2.11)] can be used.

2.3   Evaluation of Sound Velocity and Debye Temperature

If the force constants between atoms are known, the dynamical matrix can be readily constructed to determine the sound velocity. However, for complex polyatomic crystals, the calculation is still very cumbersome, and it is difficult to explicitly relate the numerical results to the complex structure. For the purpose of estimation and design, a simple model that can directly relate the sound velocity and the Debye temperature to the crystal structure is needed.

A real crystal structure can always be considered as an underlying lattice, together with a basis describing the arrangement of the atoms, ions, and molecules within a primitive cell [14]. The acoustic branches of the phonon dispersion correspond to the motion of the mass centers of the primitive cells [14]. Therefore, both the monatomic and polyatomic crystal structures can be modelled as a lattice with rigid bases connected by equivalent bonds with an equivalent force constant, as shown in Fig. 2.3.

2.3.1   Equivalent Force Constants

The elastic response of a solid can be divided into two parts, namely, (i) atomic vibrations at fixed volume, and (ii) unit cell volume fluctuations for a fixed atomic configuration (homogeneous deformation). The first part corresponds to the inhomogeneous deformation, in which the bending potentials and the torsion potentials may be important, especially in a flexible structure. The bending potential can also be
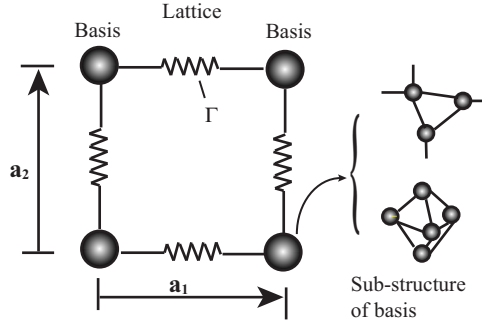
Figure 2.3: Decomposition of a complex crystal into lattice and bases, with equivalent bonds.

converted into an equivalent stretching potential between the atoms at the two ends. Since the force constant of the bending potentials and the torsion potentials are normally small, the equivalent force constant will be much reduced by the inhomogeneous deformation. It is difficult to obtain a general simple analytical solution for such an inhomogeneous deformation, and a numerical calculation using full dynamical matrix (including the bending potentials) is preferred for obtaining the equivalent force constant. However, for many solids, the crystallographic symmetries and the stability of a given phase with respect to small lattice deformations result in the diminishing effects from the first part [48], and the elastic behavior can be described using the equivalent force constants of the stretching potentials. In these cases, the bending potential and the torsion potential may contribute to the stability of the structure, but their contribution to the elastic response is negligible.

When only considering the bond stretching, it is apparent that only the transport of stretching along the translational unit vector $\mathbf{a}$ can contribute to the energy transport in this direction. Thus we define the force constant of a bond along a given unit

vector $\mathbf{a}$ as [49]

$$\Gamma_{\mu\nu,\mathbf{a}} = \frac{\partial^2 \varphi_{\mu\nu}}{\partial x_{\mathbf{a}}^2} = \frac{\partial^2 \varphi_{\mu\nu}}{\partial r_{\mu\nu}^2}(\frac{x_{\mathbf{a}}}{r_{\mu\nu}})^2 = (\mathbf{a} \cdot \mathbf{n}_{\mu\nu})^2 \Gamma_{\mu\nu}, \qquad (2.18)$$

where $x_{\mathbf{a}}$ is the projection of the bond length r along $\mathbf{a}$, and $\mathbf{n}_{\mu\nu}$ is the unit vector pointing from the particle μ to the particle ν. Eq. (2.18) shows that the projection of the force constant along $\mathbf{a}$ has a factor of $(\mathbf{a} \cdot \mathbf{n}_{\mu\nu})^2$.

The total deformation of the primitive cell is affected by all the bonds in it. Using Eq. (2.18), we may treat the bonds in a primitive cell as springs with the same $\Gamma_{\mu\nu,\mathbf{a}}$, and then convert the crystal primitive cell into a network composed of springs. This spring network can be simplified to obtain the equivalent force constant between two bases according to the following rules (we denote the force constants of two bonds as Γ_1 and Γ_2, and that of the equivalent bond of these two bonds as Γ_{eq}):

(i) when the two bonds are in series,

$$\Gamma_{eq}^{-1} = \Gamma_1^{-1} + \Gamma_2^{-1}, \qquad (2.19)$$

(ii) when the two bonds are parallel,

$$\Gamma_{eq} = \Gamma_1 + \Gamma_2. \qquad (2.20)$$

For a monatomic crystal, the primitive cell only includes one atom, and the equivalent force constant is just the force constant of the bond between the atoms.

2.3.2   Sound Velocity and Debye Temperature Model

From the lattice dynamics, the sound velocities of acoustic branches at the long-wavelength limit are the square roots of the eigenvalues of the matrix [14]

$$-\frac{1}{2M}\sum_{\mathbf{R}}(\mathbf{s}_\kappa \cdot \mathbf{R})^2 \mathbf{D}(\mathbf{R}), \ \ D_{i,j}(\mathbf{R}) = \frac{\partial^2 \varphi}{\partial u_i^0 \partial u_j^{\mathbf{R}}}, \tag{2.21}$$

where $\mathbf{s}_\kappa$ is the unit wave vector, $\mathbf{D}(\mathbf{R})$ is the force matrix, $\mathbf{R}$ is the position vector of the neighbor, u is the displacement of the mass center of the primitive cell from the equilibrium position (0 represents the origin), and M is the mass of the primitive cell.

Using the above simplified model for crystal structures, if only the stretching energy is considered, Eq. (2.5) can be rewritten as

$$\varphi = \sum_{\mathbf{R}}\frac{\Gamma_{\mathbf{R}}}{2}\{\mathbf{n}_{\mathbf{R}} \cdot [\mathbf{u}^{\mathbf{R}} - \mathbf{u}^0]\}^2, \ \ \mathbf{n}_{\mathbf{R}} = \frac{\mathbf{R}}{|\mathbf{R}|}, \tag{2.22}$$

where $\Gamma_{\mathbf{R}}$ is the equivalent force constant between the two bases. Thus $D_{i,j}(\mathbf{R}) = \eta_{i,j}\Gamma_{\mathbf{R}}$. Note that $\mathbf{R}$ is a linear function of the lattice constants, so the sound velocity will have the form

$$u_{p,g,i} = d(\mathbf{s}_{k,i},\{\mathbf{a}_i\})(\frac{\Gamma_i}{M})^{1/2}, \ \ \Gamma_i = \sum_{\mathbf{R}}[\eta(\mathbf{R},\mathbf{s}_{k,i})\Gamma_{\mathbf{R}}], \tag{2.23}$$

where $\{\mathbf{a}_i\}$ is the set of the translational vectors of the lattice. Note that Eq. (2.23) has the same form as the formula for the one-dimensional chain [49]. It is instructive to consider a plane wave travelling in a crystal, wherein the lattice is consisted of parallel planes perpendicular to the wave vector and the atoms in a plane will move in phase. The transportation along the wave vector is essentially one dimensional.

From the comparison with the formula of the one-dimensional chain [49], d is indeed the equivalent distance between the planes and normally is the linear function of the lattice constants. The effective force constant Γ is the summation of the projections of the equivalent force constant in the polarization $\mathbf{s}_{\kappa,i}$, that is, $\eta(\mathbf{R}, \mathbf{s}_{\kappa,i}) = (\mathbf{n_R} \cdot \mathbf{s}_{\kappa,i})^2$.

The average sound velocity $u_{p,g,\mathrm{A}}$ can be calculated as

$$u_{p,g,\mathrm{A}} = \left(\sum_{i=1}^{3} \frac{1}{3u_{p,g,i}^3}\right)^{-1/3}. \tag{2.24}$$

For cubic structures, the average sound velocity can be given as

$$u_{p,g,\mathrm{A}} = \frac{1}{3^{1/2}} a \left(\frac{\Gamma}{M}\right)^{1/2}, \tag{2.25}$$

where a is the lattice constant.

From the longitudinal and transversal sound velocity, we can obtain the polarization-dependent Debye temperature $T_{D,i}$ and the average Debye temperature T_D [14]

$$
\begin{aligned}
T_{\mathrm{D},i} &= u_{p,g,i} \frac{\hbar}{k_B} (6\pi^2 n_a)^{1/3} \\
&= \frac{d_i}{V_c^{1/3}} \left(\frac{\Gamma_i}{M}\right)^{1/2} \frac{\hbar}{k_B} (6\pi^2 N_c)^{1/3} \\
T_{\mathrm{D}} &= u_{p,g,A} \frac{\hbar}{k_B} (6\pi^2 n_a)^{1/3} = \left(\sum_{i=1}^{3} \frac{1}{3T_{\mathrm{D},i}^3}\right)^{-1/3},
\end{aligned} \tag{2.26}
$$

where n_a is the number density of atoms, N_c is the number of atoms in a primitive cell, and V_c is the volume of a primitive cell. Here $d_i/V_c^{1/3}$ is only a function of the ratio of lattice constants and the polarization, and the Debye temperature relates to the ratio of the lattice constants rather than their absolute values. It is apparent that if the lattice constant and other parameters are the same except the lattice type, the order of magnitude of T_D is $T_D(\mathrm{FCC}) > T_D(\mathrm{BCC}) > T_D(\mathrm{SC})$.

35

Figure 2.4 compares the calculated and experimental Debye temperatures [2] (determined from elastic constants or specific heat capacity measurements) of some crystals. The force constants used in the calculation are from the combinative rule and Table 2.1. The overall agreement is good. The force constant for metals are calculated according to Eq. (2.17). It is found that $m = 8$ gives good agreement with experimental values. Again, it is found that for metallic crystals, the force constant can be reduced significantly by the long-range electrostatic interaction (by a factor of about 5), which results in a low Debye temperature.
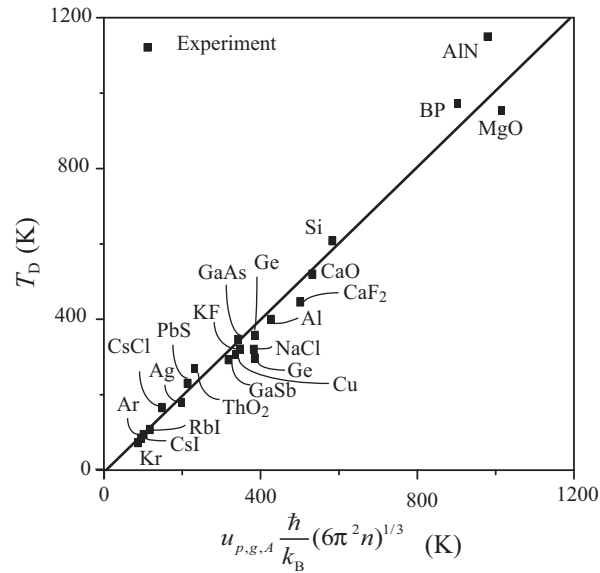
Figure 2.4: Comparison of the predicted and measured Debye temperature for some crystals. The force constants for metallic crystals are calculated according to Eq. (2.17) (m is set to 8). The experimental values are from [2].

2.4 Thermal Expansion and Grüneisen Parameter

The Grüneisen parameter has been used to represent the volume dependence of the normal mode frequencies. The overall Grüneisen parameter γ_G is defined as [14]

$$\gamma_G = \frac{\sum_{\kappa,\alpha} \gamma_{G,\kappa,\alpha} c_{v\alpha}(\kappa)}{\sum_{\kappa,\alpha} c_{v\alpha}(\kappa)}, \quad \gamma_{G,\kappa,\alpha} = -\frac{\partial \ln \omega_{\kappa,\alpha}}{\partial \ln V}, \quad (2.27)$$

where the subscript α denotes the branch of a normal mode, c_v is the heat capacity per normal mode, and V is the volume. In the Debye approximation, all the normal-mode frequencies scale linearly with the Debye temperature T_D, and therefore [14]

$$\gamma_G = \gamma_{G,\kappa,\alpha} = -\frac{\partial \ln \omega_D}{\partial \ln V}. \quad (2.28)$$

That is, γ_G represents the relative shift of the Debye angular frequency with respect to the volume.

We consider a crystal containing only one bond type. According to Eq. (2.23) and (2.28), since the Debye frequency $\omega_D \propto \Gamma^{1/2}$ and the volume $V \propto r_e^3$, we have

$$\gamma_G = -\frac{d \ln \Gamma}{6d \ln r_e}. \quad (2.29)$$

Note that γ_G only relates to the bond. Zallen etc. [50] defined a "bonding-scaling parameter" γ_G' as

$$\gamma_{G,i}' = -\frac{d \ln \Gamma_i'}{6d \ln r_i'}, \quad (2.30)$$

where Γ_i' and r_i' are the force constant and the equilibrium length of the bond i. For the crystals containing only one bond type, the Grüneisen parameter γ_G is equal to the bonding-scaling parameter γ_G'.

We can rewrite Eq. (2.30) in terms of a a small relative deviation fraction ε:

$$\Gamma_i'(\varepsilon) \simeq \Gamma_\circ'(1 - 6\gamma_G'\varepsilon), \tag{2.31}$$

where $\Gamma_\circ'$ is the initial equivalent force constant. It is apparent that γ_G' represents the intrinsic anharmonicity of a bond, i.e., the relative shift of the force constant with respect to the bond length. It seems reasonable that the γ_G' of each bond is independent of other bonds.

We again consider the crystal containing one bond type to obtain the bond-scaling parameter γ_G'. Ruffa [51] developed a thermodynamic description of Morse oscillators using a statistical treatment. Here a similar approach is applied for the Lennard-Jones oscillators representing the interatomic potentials. Consider an assembly of independent oscillators with the interatomic potential of Eq. (2.9), of which the natural angular frequency $\omega = (\Gamma/\mu)^{1/2}$ (μ is the reduced mass of the oscillator). If Eq. (2.9) is expanded in a Taylor series, the vibrational energy E_l and the mean atomic separation $\langle r_l \rangle$ of the motion with the principle quantum number l of this oscillator can be expressed as [52]

$$
\begin{aligned}
E_l &= \hbar\omega(l + \frac{1}{2}) - C_e\hbar^2\omega^2(l + \frac{1}{2})^2, C_e = \frac{5(m+n+3)^2}{48\varphi_\circ mn} \\
\langle r_l \rangle &= r_\circ + C_r r_\circ \hbar\omega(l + \frac{1}{2}), C_r = \frac{3(m+n+3)}{2\varphi_\circ mn}.
\end{aligned} \tag{2.32}
$$

Then, we have (see the derivation in Appendix A)

$$
\begin{aligned}
\gamma_G' &\simeq \gamma_{G,\circ}'[1 + C_e k_B T \frac{f_1(x_D)}{f(x_D)}], \ \gamma_{G,\circ}' = \frac{m+n+3}{6} \\
f(x_D) &= \int_0^{x_D} \frac{x^3 dx}{e^x - 1}, \ x_D = T_D/T \\
f_1(x_D) &= \int_0^{x_D} \frac{x^4(1 + e^x)dx}{(e^x - 1)^2}.
\end{aligned} \tag{2.33}
$$

38

Typically, the vibration energy is much smaller than the dissociation energy and $C_e k_B T$ is small, so the temperature dependence of γ'_G is weak. At high temperatures, γ'_G will reach $\gamma'_{G,o}$. It is very interesting to note that $\gamma'_{G,o}$ only depends on m and n, or the bond type.

(i) Ideal ionic bonds. The attractive potential is dominated by the electrostatic potential, and the lattice summation of the long-range electrostatic interactions does not change n (the Madelung term), thus $n = 1$. The repulsive term arises from the full-filled shells and the Pauli exclusion principle. The measurements for typical ionic bonds show $m = 6 \sim 10$ [14]. The midpoint $m = 8$ is a reasonable choice for the estimation, therefore $\gamma'_{G,o} = 2.0$. In fact, $\gamma'_{G,o} = 2.0$ agrees well with the high temperature γ_G values of many typical ionic crystals with one bond type [49, 2].

(ii) van der Waals interactions. The attractive term arises from the interaction between dipoles and varies as $1/r^6$, that is, $n = 6$. The widely-used 12-6 Lennard-Jones potential chooses $m = 12$ for the repulsive term. However, it is found that $m = 12$ makes the repulsive term very steep [32]. $m = 12$ gives $\gamma'_{G,o} = 3.5$, a much higher value than the measured results. For example, at high temperatures, γ_G of Ne, Ar, Kr, and Xe are 2.76, 2.73, 2.84, 2.65 [2], respectively. Considering the repulsive term of van der Waals interaction arises from the same mechanism (i.e., the filled outer shell) as in an ionic bond, it is reasonable to choose the same value 8 for m. This choice gives $\gamma'_{G,o} = 2.83$, which agrees much better with the above experimental results.

(iii) Non-polarized covalent bonds. The attractive term is due to the electrostatic interaction, therefore, $n = 1$. For m, the case is more complicated, because the

distribution of valence electrons differs substantially from that in isolated atoms or ions. The repulsive term includes the electrostatic term and the term due to the Pauli exclusion principle. In fact, the covalent bond is more appropriately described by the Morse potential [32]

$$\varphi = \varphi_\circ [e^{-2a_\circ(r-r_\circ)} - 2e^{-a_\circ(r-r_\circ)}]. \tag{2.34}$$

Ruffa [51] suggested an empirical relation: $a_\circ r_\circ = (m+4)/5$. For typical covalent bonds, $a_\circ r_\circ \simeq 1.0 \sim 1.2$, thus $m \simeq 1 \sim 2$. Since $m > n$, we choose $m = 2$ and obtain $\gamma'_{G,\circ} = 1.0$. This value is also in accord with the relation $\Gamma r^6 = \text{constant}$ for covalent bonds, as suggested by Herzberg [40].

The covalent bond between atoms with different electronegativities is partially polarized (ionic bonds can also be considered highly polarized covalent bonds). Using the relation of the percent of the ionic character c proposed by Pauling [45], γ'_G of a polarized bond can be given as

$$\gamma'_G = \gamma'_{G,AB} = (1-c)\gamma_{G,cov} + c\gamma'_{G,ion}, \ c = 1 - e^{-(\chi_A - \chi_B)^2/4}, \tag{2.35}$$

where $\gamma'_{G,cov}$ and $\gamma'_{G,ion}$ represent the bond-scaling parameters of a non-polarized covalent bond and the ideal ionic bond, respectively. Equation (2.35) together with Eq. (2.33) can also be used for the rough estimation of m in an interatomic potential:

$$m \simeq 8 - 6e^{-(\chi_A - \chi_B)^2/4}. \tag{2.36}$$

(iv) Metallic bonds. Though metallic crystals also include ions, they are very different from ionic crystals. The metals can be treated as ions immersed in a sea of free electrons [14]. Thus, the interactions between ions can be treated as the summation of the bare interactions between ions and the electron-ion interactions. Both the

repulsive term and attractive term include the long-range electrostatic interactions. However, due to the screening effects of free electrons, the interaction between ions decays faster than the pure coulomb interactions, thus, $m > 1$ and $n \geq 1$ (due to the attractions of ions to free electrons, repulsive term decays faster than the attractive term). The derivation of γ'_G for metallic bonds is complicated. To compare it with experimental results, one also needs to include the contribution from the free electrons (it may be small at high temperatures). However, since the screening effects increase with the increasing electron number density [14], we would expect that in the metals with high electron number density, $m \simeq 8$ and $1 \leq n \leq 6$. For simplicity, in this work we set $m = 8$ and $n = 1$ (the same values for ionic bonds). The resulting $\gamma_G = 2.0$ is close to the experimental results of many metals (the alkali metals have a γ_G close to 1.2, due to the poor screening effects).

(v) Other interactions. Some other interactions, e.g., ion-dipole interaction, may exist in some crystals. These interaction may be considered as the cross terms of the above interactions. Using the combinative rule for potentials [Eqs. (2.8) and (2.7)], we can have

$$m = \frac{(m_1 + m_2)}{2}, \ n = \frac{(n_1 + n_2)}{2}, \gamma'_G = \frac{(\gamma'_{G,1} + \gamma'_{G,2})}{2}, \tag{2.37}$$

where the subscripts 1 and 2 denote the individual interactions.

It can be seen that the order of magnitude of γ'_G for bonds is γ'_G(van der Waals bond) $> \gamma'_G$(ionic bond) $> \gamma'_G$(polarized covalent bond) $> \gamma'_G$(non-polarized covalent bond). Figure 2.5 compares the calculated high-temperature Grüneisen parameters of crystals containing only one bond type with the experimental results (at the Debye

temperature) [2], and the overall agreement is good. Note that for ionic crystals, Grüneisen parameters are slightly overestimated. One reason is that the temperature at which the measurements are performed is not high enough. For example, γ_G of NaCl at the Debye temperature is 1.57, but at 800 K, its value is 1.76 [53], compared to 1.71 given by Eq. (2.35). Another possible reason is that c in Eq. (2.35) determined by Pauling is not very accurate.
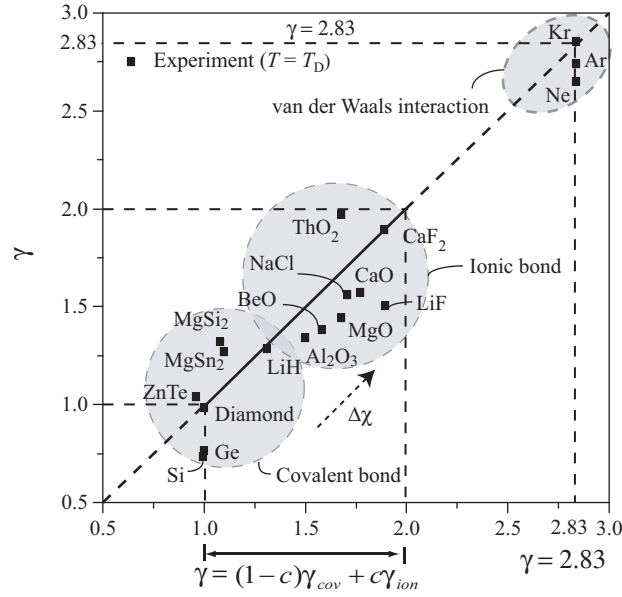
Figure 2.5: Comparison of predicted high temperature Grüneisen parameters with the experimental results at the Debye temperatures, for some crystals [2].

Note that Eq. (2.30) is valid for the equivalent force constant Γ, so the Grüneisen parameter γ_G of a crystal can be obtained by evaluating the equivalent γ_G' of the equivalent bond.

For two parallel bonds, Eqs. (2.20) and (2.31) lead to

$$\gamma_G' = \frac{\Gamma_{10}}{\Gamma_{10} + \Gamma_{20}}\gamma_{G,1}' + \frac{\Gamma_{20}}{\Gamma_{10} + \Gamma_{20}}\gamma_{G,2}', \tag{2.38}$$

where Γ_{10} and Γ_{20} represent the equilibrium force constants of bond 1 and 2. That is, the equivalent γ'_G of the parallel bonds is the summation of the $\gamma'_{G,i}$ of the bonds weighted by the fraction of force constants.

Similarly, for two bonds in series, the equilibrium requirement gives

$$\varepsilon_1 = \frac{\Gamma_{20}(r_1 + r_2)}{(\Gamma_{10} + \Gamma_{20})r_1}\varepsilon, \ \varepsilon_2 = \frac{\Gamma_{10}(r_1 + r_2)}{(\Gamma_{10} + \Gamma_{20})r_2}\varepsilon, \tag{2.39}$$

and Eqs. (2.19) and (2.31) lead to

$$\gamma'_G = (\frac{\Gamma_{20}}{\Gamma_{10} + \Gamma_{20}})^2 \frac{r_1 + r_2}{r_1}\gamma'_{G,1} + (\frac{\Gamma_{10}}{\Gamma_{20} + \Gamma_{10}})^2 \frac{r_1 + r_2}{r_2}\gamma'_{G,2}. \tag{2.40}$$

Equation (2.40) shows the equivalent γ'_G is related not only to the force constants and $\gamma'_{G,i}$, but also to the bond lengths. Note when $\varepsilon_1 = \varepsilon_2 = \varepsilon$ (homogeneous deformation), Eq. (2.40) can be reduced to

$$\gamma'_G = (\frac{\Gamma_{20}}{\Gamma_{10} + \Gamma_{20}})\gamma'_{G,1} + (\frac{\Gamma_{10}}{\Gamma_{20} + \Gamma_{10}})\gamma'_{G,2}, \tag{2.41}$$

which does not relate to the bond lengths.

Assuming $r_1 \simeq r_2$ and $\gamma'_{G,2}$ is the smaller one, the dependence of $\gamma'_G/\gamma'_{G,2}$ on the ratio of force constants Γ_{10}/Γ_{20} is plotted in Fig. 2.6.

Figure 2.6 shows that, the equivalent γ'_G of both the parallel and serial arrangement is always higher than $\gamma'_{G,2}$. For the parallel arrangement, $\gamma'_{G,2} \leq \gamma'_G \leq \gamma'_{G,1}$, the stronger bond contributes more to the equivalent γ'_G; when $\gamma'_{G,1}/\gamma'_{G,2} = 1$, the equivalent γ'_G is independent on Γ_{10}/Γ_{20}. For serial configuration, $\gamma'_{G,2} \leq \gamma'_G \leq 2\gamma'_{G,1}$, the weaker bond contributes more to γ'_G. For equivalent γ'_G, according to Eq. (2.40), the lowest value $2\gamma'_{G,1}\gamma'_{G,2}/(\gamma'_{G,1} + \gamma'_{G,2})$ is achieved when $\Gamma_{10}\gamma'_{G,1} = \Gamma_{20}\gamma'_{G,2}$, and the mismatch of $\Gamma_i\gamma'_{G,i}$ of neighboring bonds causes an increase in the anharmonicity.

To increase anharmonicity and reduce the sound velocity, the serial arrangement is preferred.
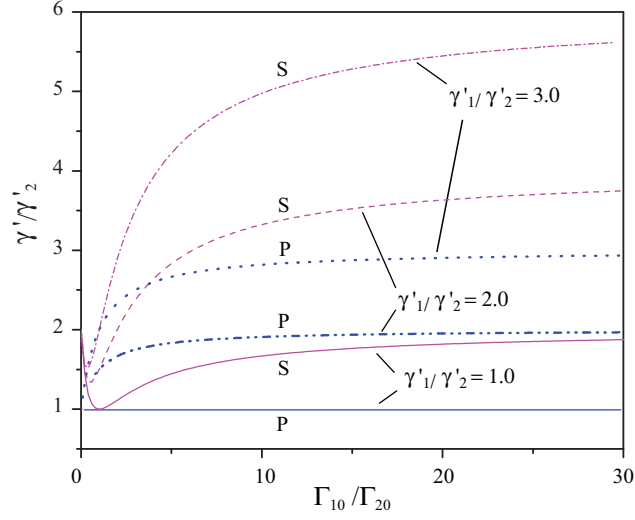
Figure 2.6: Variation of ratio of the equivalent bond-scaling parameter to the smaller bond-scaling parameter of the bonds $\gamma'_{\rm G}/\gamma'_{\rm G,2}$ with respect to the ratio of the force constants Γ_{10}/Γ_{20}. The symbols P and S denote the parallel and serial arrangements.

2.5   Prediction of Thermal Conductivity

Using the relations for $\gamma_{\rm G}$, α and $T_{\rm D}$, when ω_c is comparable with $\omega_{\rm D}$, the thermal conductivity can be readily calculated using the Slack relation. The predicted thermal conductivities of some crystals at high temperatures are listed in Table 2.2 and shown in Fig. 2.7(a), and the measured values and the values calculated by Slack [2] are also given. Note Slack used $T_{\rm D,\infty}$ calculated from the phonon density of states D_p, which is different from the measured $T_{\rm D}$ listed in Table 2.2. Table 2.2 shows that the thermal conductivities and the Debye temperatures estimated by our model agree well
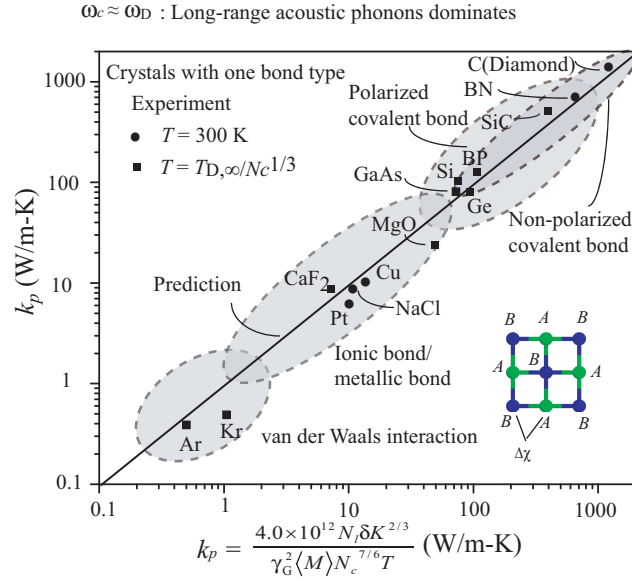
Figure 2.7: Comparison of the predicted lattice thermal conductivity of some compact crystals with the experimental results.

with the experimental results and the Slack results, but the Grüneisen parameters are normally overestimated in our model, as discussed in Section 2.4. The average mean square error between the estimated values and the experimental results is about 20%. Slack used $T_{D,\infty}$ along with the experimental γ_G (but 0.7 was used for Ge, Si, and SiC for better agreement with the experiments [2]), both of which are normally slightly lower than the values estimated in our model. Note that we also predict the lattice thermal conductivity of Al and Pt, by only considering the phonon-phonon scattering. The crystalline metals normally have a low lattice thermal conductivity, not only due to the strong scattering of phonons by free electrons, but also due to their large Grüneisen parameters and small force constants (caused by long-range electrostatic interactions).

Table 2.2: Predicted thermal conductivities and parameters of some crystals at given temperatures. The experimental results [2, 14] are shown in the parentheses, and the calculated results by Slack are shown in the brackets. Note that Slack used $T_{D,\infty}$ determined from the phonon density states, which is different from the experimental T_D listed here. Also Slack used the γ_G derived from experiments except diamond, SiC, Ge, GaAs, and BP (he chose 0.7 for these crystals for better agreement with the experiments). The values of m used in the calculations are all estimated using Eq. (2.36), rather than from the experimental results.

Crystals	T (K)	T_D	N_c	γ_G	k_p (W/m-K)
Ar	84	94 (85)	1	2.83 (2.73)	0.5 (0.4)[3.8]
Kr	66	87 (73)	1	2.83 (2.84)	1.1 (0.5)[0.4]
Diamond	300	2183 (2230)	2	1.0 (0.9)	1292 (1350)
Ge	235	382 (360)	2	1.0 (0.76)	95 (83)[89]
Si	395	584 (625)	2	1.0 (0.56)	76.7 (115)[93]
Cu	300	339 (315)	1	2.0	14.4 (10^b)
Pt	300	194 (230)	1	2.0	9.1 (6^b)
GaAs	220	367 (346)	2	1.01 (0.75)	72 (81)[77]
CaF$_2$	345	453(510)	3	1.89 (1.89)	7.0 (8.5)[9.1]
MgO	600	1034 (945)	2	1.68 (1.44)	53 (25) [28]
NaCl	230	382(330)	2	1.71(1.57)	11.1 (8.6)[6.3]
c-BN	300	1614	2	1.22	733 (748)
SiC	300	1212 (1079)	2	1.11 (0.76)	463 (490)[461]
BP	670	891 (982)	2	1.0	97.46 (110)[166]
PN[a]	300	890	2	1.16	329
CSe[a]	300	706	2	1.0	327

[a] assuming the crystal has the similar structure as BN, and the bond length is calculated from the combinative rule.

[b] the lattice conductivities are from reference [39]. They are obtained by subtracting the electrical thermal conductivity (derived from Wiedemann-Franz law) from the total thermal conductivity.

When $\omega_c \ll \omega_D$, the thermal transport is dominated by the short-range acoustic phonons and optical phonons. While the acoustic contribution can be calculated using a relation similar to the Cahill-Pohl relation [54, 4], the optical part is difficult to determine and it is comparable to the acoustic contribution [4, 29]. However, for some special atomic structures, the phonon mean-free path is limited by the crystal structure, and the thermal conductivities of such crystals often exhibit temperature-independence above the Debye temperature. According to the kinetic relation [14] $k = n_a c_v u_{p,g} \lambda / 3$ (c_v is the heat capacity per atom), if the phonon mean-free path λ can be determined from the characteristics of the structure, the thermal conductivity can also be easily calculated. This will be discussed in Chapter 3.

2.6 Summary and Conclusion

A simple atomic structure based model for the estimation of lattice thermal conductivity of crystals at moderate and high temperature is proposed. When the critical frequency ω_c is comparable with the Debye frequency ω_D, the thermal conductivity is obtained on the basis of the Debye temperature and the Grüneisen parameter calculated from the atomic configuration of the structure.

The calculation of the Debye temperature involves three steps: (i) estimation of the force constant of arbitrary pair of interacting atoms on the basis of a phenomenological combinative rule and data listed in Table 2.1; (ii) simplification of the network system of bonds using analogy with a spring system, and calculation of the equivalent bonds; (iii) calculation of the Debye temperature using the equivalent bonds and the

topology of the crystal.

The determination of the Grüneisen parameter consists of two steps: (i) estimation of the bond-scaling parameter of each single bond; (ii) estimation of the equivalent Grüneisen parameter using Eqs. (2.38) and (2.40) on the basis of the configuration of bonds. It is found that when $\Gamma \gamma'_G$ of the bonds match, the equivalent Grüneisen parameter achieves its minimum.

This simple atomic structure-based model can be used to quickly estimate the high-temperature thermal conductivity of crystals. On the other hand, some useful insights into the design of materials with desired properties can be extracted.

According to Eqs. (3.10) and (2.26), we have

$$ k = \frac{4.0 \times 10^{12} N_l \Gamma^{3/2} \delta}{\gamma_G^2 \langle M \rangle^{1/2} N_c^{7/6} T}, \tag{2.42} $$

where N_l is a constant related only to lattice type. Therefore, to increase the thermal conductivity, one may increase the equivalent force constant Γ and lattice constant a, while reducing the mean atomic weight $\langle M \rangle$, N_c, and the Grüneisen parameter γ_G. Here FCC is expected to achieve a high thermal conductivity. The opposite approaches can be used to achieve a low lattice thermal conductivity.

Evidently, molecular crystals will normally have a very low thermal conductivity because of the small Γ, large γ_G and N_c.

For ionic and covalent diatomic crystals, $\gamma_G = 2 - \exp(-\Delta\chi^2/4)$, then Eq. (2.43) can be rewritten as

$$ k = \frac{4.0 \times 10^{12} N_l \delta \Gamma^{3/2}}{[2 - \exp(-\Delta\chi^2/4)]^2 \langle M \rangle^{1/2} N_c^{7/6}}. \tag{2.43} $$

For compact structures, δ may be set as the mean diameter of the atoms.

Table 2.1 and Fig. 2.1(a) show that most metals have a low $\Gamma_{AA,1}$ around 50 N/m. Even when they bond with F (which has the highest $\Gamma_{AA,1}$), $\Gamma_{AB,1}$ is expected to be lower than 250 N/m. Also, metal elements normally have a heavy mass and ionic bonds have a relatively high $\Delta\chi$. In comparison, covalent bonds may have a higher $\Gamma_{AB,1}$, lower $\Delta\chi$, and those nonmetallic elements with a high $\Gamma_{AA,1}$ have a relatively light mass. Thus, for high thermal conductivity, covalent crystals are preferred. Among covalent crystals, the compounds of N and C are expected to have a high thermal conductivity, since N and C have the highest $\Gamma_{AA,1}$, moderate χ, light masses, and possibly high bond orders. In general, the sequence of lattice conductivity for crystals is: k_p(non-polarized covalent crystal) $> k_p$(polarized covalent crystal) $> k_p$(ionic crystal) $> k_p$(molecular crystal), as shown in Fig. 2.7(a). Furthermore, the oxidation states of the elements need to match and the mass difference should be small to achieve a small N_c. Materials satisfying these conditions are expected to have a high thermal conductivity, e.g., BN, AlN, BP and SiC, furthermore, it is expected that PN, and CSe would have a high thermal conductivity if they could be synthesized (listed in Table 2.2).

For thermoelectic materials or thermal insulators, lower phonon thermal conductivity is desired. In addition to the common strategies (e.g., using heavy atoms and making a complex unit cell), the following may be used as a guide:

(i) Adding flexible structures on the transport path. Flexible structures with bending or torsion motion often have a small Γ and high γ_G, thus they can both reduce the sound velocity and increasing the anharmonic scattering.

(ii) Making the bonds as perpendicular as possible to the transport path. This

can reduce the projection of the force constant, and lower the Debye temperature.

(iii) Enlarging the mismatch of $\Gamma\gamma_G$ of the neighboring bonds. Substituting some bonds with bonds with higher γ_G, or substituting some bonds to increase the mismatch of force constant, can increase the anharmonic scattering. For example, by replacing some covalent pairs with pairs with charges or larger electronegativity difference, the phonon thermal conductivity can be reduced, as observed by Cahill, et al. [54].

(iv) Arranging the bonds with high γ_G in series. This will help increase the anharmonic scattering.

This simple atomic structure model allows for the quick estimation of thermal transport properties, and can be used as a guide for the design of new materials with a desired lattice conductivity.

Chapter 3

Phonon Transport in Linked-Cage Crystals: Metal-Organic Frameworks

There exist many special structures that can limit the phonon mean-free path at high temperature. Some special substructures act as scatterers and limit the phonon mean-free path to be the distance between them. Here we discuss the linked-cage structure, which is common for nanoporous crystals, e.g., MOFs, zeolites, and many molecular crystals.

3.1   Linked-Cage Crystals: Metal-Organic Frameworks

The metal-organic frameworks (MOFs), a sub-family of the nanoporous crystals, are characterized by metal-oxygen cages (vertices) connected by organic bridges.[15, 55, 56, 57] MOFs currently attract intensive interest for their excellent potential for storing and separating gases (e.g., N_2, Ar, CO_2, CH_4, and H_2).[58, 59, 60] By changing the organic bridge and/or its functionalization, new MOFs can be designed and synthesized without changing the underlying topology. Recent work has focused on their structural properties,[55] adsorption characteristics,[55, 58, 59, 60] and the diffusion of light gases through them,[61] but their thermal transport characteristics have yet to be considered. Knowledge of the thermal conductivity of a MOF is crucial for predicting its behavior during the adsorption/desoprtion of gases and in other potential applications. Furthermore, the variety of MOFs available points towards the possibility of systematically designing materials with specified thermal properties. To prepare for such molecular design, an understanding of the relationship between a MOF structure and its thermal conductivity is required.

We report the investigation of the thermal transport in MOF-5 (shown in Fig. 3.1), which is the smallest of a series of MOFs that have a simple cubic crystal structure.[55] It is built from zinc-oxygen tetrahedra connected by 1,4-benzenedicarboxylate (BDC) bridges. It has a low density (610 kg/m^3), a large free cage volume (79%), and a pore diameter of 11.2 Å.[55]

In this investigation, MD will be used to predict the thermal conductivity of
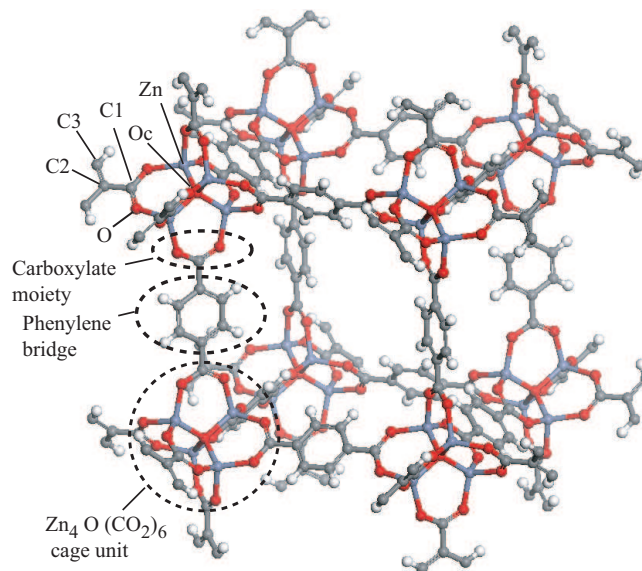
Figure 3.1: MOF-5 unit cell: $8[Zn_4O(BDC)_3]$. This is the $1 \times 1 \times 1$ system. The cage is built from four zinc-oxygen tetrahedra ($ZnOcO_3$), which share the Oc atom (located at the center of the cage). The O-C1-O group forms a carboxylate moiety, to which a phenylene group is attached. Note the distinction between the three carbon sites. The carboxylate moieties on either side of a phenylene ring are perpendicular. Thus, eight cages and twelve bridges are required to form the simple cubic unit cell, which has a lattice constant of 25.85 Å. The formal charges on the oxygen atoms at the center of the cage (Oc), the carboxylate-oxygen atoms (O), and the zinc atoms are -2, -0.5, and +2. The other species are charge neutral.

MOF-5. The data required for a BTE study is currently unavailable.

We first describe the development of the classical interatomic potentials (force fields) needed to perform MD simulations of MOFs. Using these potentials, the thermal conductivity of MOF-5 is predicted between temperatures of 200 K and 400 K. The thermal conductivity is decomposed into components associated with short- and long-range acoustic phonons and optical phonons. A model is formulated to explain the observed weak temperature dependence, and a critical frequency is introduced to separate the contributions of the two acoustic components. Finite size and quantum effects on the thermal conductivity prediction are also discussed. The relationship between the MOF-5 structure and its thermal behavior is explored, and a simplified structural model is proposed.

3.2 Classical Interatomic Potentials for MOF-5

To model the dynamics of MOF-5, the development of potentials for different interactions in MOF-5 is required. Previous MD studies have focused on the interaction of gases with the structure, and modelled the crystal as being rigid.[61] The main challenge in the construction of a potential set is related to the oxygen atom in the carboxylate moiety, which has a charge of -0.5. While potentials exist for Zn-O systems with formal charges,[62] parameters are not available for this reduced charge state. To construct the potentials, we fit selected algebraic expressions to energy surfaces obtained from *ab initio* calculations.

The *ab initio* calculations are performed with Gaussian 98.[63] First, to determine

Table 3.1: Structural parameters predicted by different *ab initio* methods/basis sets and the experimental data[15]. B3YLP/ 6-311g** gives the best agreement with the experimental data based on a sum of squares calculation. $S^2 = \sum_{i=1}^{9}[(s_i - s_{exp})/s_{exp}]^2$, where the summation is over the bond lengths and angles listed.

Method/ Basis	Bond lengths (Å)					Angles (degree)				S^2 (10^{-3})
	Oc-Zn	Zn-O	O-C1	C1-C2	C2-H	Oc-Zn-O	Zn-O-C1	O-C1-C2	C2-C3-H	
RHF/ sto-3g*	1.877	1.865	1.281	1.549	1.085	113.5	127.6	116.1	108.8	6.23
RHF/6-311g**	1.992	1.962	1.241	1.504	1.080	109.5	133.6	117.2	108.8	1.53
RHF/6-311+g**	1.996	1.981	1.242	1.506	1.080	109.5	133.3	117.1	108.8	1.95
RHF/LANL2DZ	2.044	1.973	1.271	1.504	1.077	108.9	135.3	119.4	109.1	4.81
B3YLP/6-311g**	**1.972**	**1.953**	**1.262**	**1.510**	**1.088**	**110.8**	**131.7**	**117.8**	**111.1**	**0.76**
B3YLP/6-311+g**	1.982	1.980	1.265	1.512	1.087	110.8	131.6	117.8	111.0	1.40
B3YLP/LANL2DZ	2.037	1.988	1.295	1.514	1.091	110.0	133.6	118.8	110.5	4.92
Experiment	1.936	1.941	1.252	1.498	1.090	111.1	132.3	118.1	109.5	

the appropriate method/basis set, the MOF-5 structure is relaxed using common formulations. The resulting structures are then compared to the experimental data, as shown in Table 3.1. Based on a sum of squares error calculation (compared to the experimental data), B3YLP/6-311g** is found to be most suitable. The energy surface of MOF-5 is then scanned using B3YLP/6-311g** by changing bond lengths and angles. The classical potentials are fitted to this data using the GULP software package.[64]

Table 3.2: Interatomic potentials for MOF-5. r, θ and ϕ are distance, bond angle and torsion angle. The C2 and C3 atoms are treated in the same way in the pair and angular potentials (denoted as C2/3). The cutoff radius of electrostatic terms is 10 Å. For all other terms, only bonded interactions are considered.

Interaction	Potential Model	Parameters
Pair		
Oc-Zn	$\frac{1}{r}q_{Oc}q_{Zn} + A\exp(-\frac{r}{r_\circ}) - Cr^{-6}$	$A = 770.127$ eV, $r_\circ = 0.357$ Å, $C = 0.00088$ eV-Å^6
Oc-O	$\frac{1}{r}q_{Oc}q_O$	
O-Zn	$\frac{1}{r}q_{Oc}q_{Zn} + A\exp(-\frac{r}{r_\circ}) - Cr^{-6}$	$A = 529.7$ eV, $r_\circ = 0.352$ Å, $C = 0.0$ eV-Å^6
Zn-Zn	$\frac{1}{r}q_{Zn}q_{Zn}$	
O-O	$\frac{1}{r}q_O q_O$	
O-C1	$\varphi_\circ\{[1 - \exp(-a(r - r_\circ))]^2 - 1\}$	$\varphi_\circ = 4.624$ eV, $a = 2.337$ Å^{-1}, $r_\circ = 1.28$ Å
C1-C2	$\varphi_\circ\{[1 - \exp(-a(r - r_\circ))]^2 - 1\}$	$\varphi_\circ = 5.439$ eV, $a = 1.669$ Å^{-1}, $r_\circ = 1.482$ Å
C2/3-C2/3	$\varphi_\circ\{[1 - \exp(-a(r - r_\circ))]^2 - 1\}$	$\varphi_\circ = 8.196$ eV, $a = 1.680$ Å^{-1}, $r_\circ = 1.388$ Å
Angular		
C2/3-C2/3-C2/3	$\frac{1}{2}k_\theta(\cos\theta - \cos\theta_\circ)^2$	$k_\theta = 11.732$ eV, $\theta_\circ = 120°$
O-C1-O	$\frac{1}{2}k_\theta(\cos\theta - \cos\theta_\circ)^2$	$k_\theta = 11.0$ eV, $\theta_\circ = 120°$
C1-C2-C3	$\frac{1}{2}k_\theta(\cos\theta - \cos\theta_\circ)^2$	$k_\theta = 9.599$ eV, $\theta_\circ = 120°$
Zn-O-C1	$\frac{1}{2}k_\theta(\cos\theta - \cos\theta_\circ)^2$	$k_\theta = 11.0$ eV, $\theta_\circ = 132.3°$
Torsional		
C2/3-C2/3-C2/3-C2/3	$k_\phi[1 - \cos(\phi - \phi_\circ)]$	$k_\phi = 1.735$ eV, $\phi_\circ = 0°$
O-C1-C2-C3	$k_\phi[1 - \cos(\phi - \phi_\circ)]$	$k_\phi = 1.587$ eV, $\phi_\circ = 0°$
O-C1-O-Zn	$k_\phi[1 - \cos(\phi - \phi_\circ)]$	$k_\phi = 1.732$ eV, $\phi_\circ = 0°$

The set of interatomic potentials includes two-body (pair), three-body (angular), and four-body (torsional) terms, as presented in Table 5.3. The C2 and C3 atoms are treated in the same way in the pair and angular potentials (denoted as C2/3). The C2/3-C2/3-C2/3 bending and C2/3-C2/3-C2/3-C2/3 torsion potentials are taken from Chelli et al.[65] Other than electrostatics, no two-body interactions are assumed for the non-bonded pairs of Oc-O, O-O, and Zn-Zn. These interactions are best captured with the three- and four-body potentials. The hydrogen atoms are not directly included in the model. The C3-H group is taken to be a rigid entity (by adding the hydrogen mass to the carbon mass), a common treatment for hydrogen atoms in MD.[32]

The MOF-5 structure is then relaxed under the new potentials with GULP. The resulting structural parameters are shown in Fig. 3.2, where they are compared with the experimental data. The average difference between the predicated data and the experimental data is 2%. The MOF-177, IRMOF-11, and IRMOF-16 structures have also been successfully relaxed in GULP using these potentials, indicating their transferability to other MOFs.

To further validate the potential, we compare the MD predicted infrared (IR) spectrum and that from experimental NIR-FT (Near InfraRed-Fourier Transform) measurements.[3] The range of the NIR-FT data is from 75 Trad/s to 375 Trad/s (400 cm^{-1} $\sim$ 2000 cm^{-1}). The MD predicted IR spectrum is obtained by taking the Fourier transform of the electrical flux autocorrelation function:[66, 67]

$$I(\omega) \quad \propto \quad \int_0^\infty \langle \frac{d\mathbf{M}(t)}{dt} \cdot \frac{d\mathbf{M}(0)}{dt} \rangle \cos(\omega t) dt, \qquad (3.1)$$
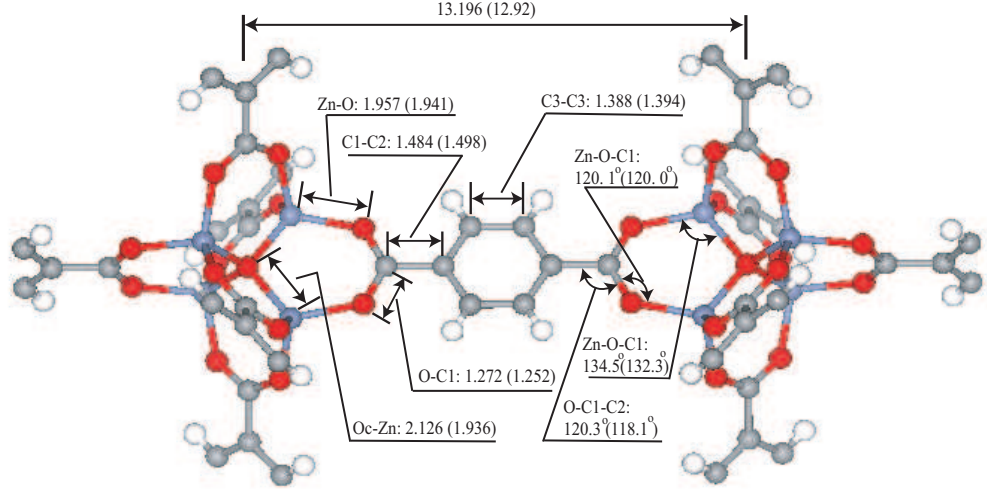
Figure 3.2: MOF-5 structure produced by optimization with GULP using the new potentials and the experimental data (in parentheses). The lengths are in Angstrom and the angles are in degrees.

where

$$\frac{d\mathbf{M}(t)}{dt} = \sum_{i=1}^{N} q_i \mathbf{u}_i(t). \tag{3.2}$$

Here, $I(\omega)$ is the spectral density, ω is angular frequency, $\mathbf{M}(t)$ is the summation of the individual dipole moments of all the atoms in the system, t is time, N is the number of atoms in the system, q_i is the charge on the ith atom, and $\mathbf{u}_i(t)$ is the velocity of ith atom. In Fig. 3.3, the two IR spectra are shown and the main band peaks are identified. The average deviation between the main band peaks predicted by MD and the associated experimental data is 3.5%, which we take to be good agreement.[68]
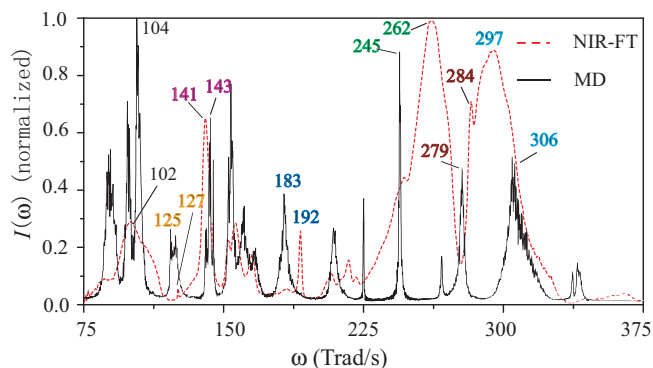
Figure 3.3: IR spectrum calculated from MD and the experimental (NIR-FT) results. The curves are normalized against the largest peak in each data set. The correspondence between peaks is established by comparing the partial density of states of the species calculated from MD (see Fig. 3.8) to the results of experiments,[3] and by visual comparison of the two spectra. The 127/125 peak is related to vibrations of the Oc atom, the 245/262 peak is associated with symmetric stretching of the carboxylate moiety, the 284/279 peak results from vibrations of the phenylene ring, and the 306/297 peak is associated with asymmetric stretching of the carboxylate moiety.

3.3 Simulation Details

3.3.1 Logistics

All data used for the thermal conductivity predictions come from simulations run in the NVE (constant mass, volume, and energy) ensemble. Unless noted, the simulation cell contains eight unit cells in a $2 \times 2 \times 2$ arrangement (2,624 atoms). Size effects will be discussed in Section 3.3.2.

The Verlet leapfrog algorithm is used to integrate the equations of motion with a time step of 0.2 fs. The Wolf method is applied to model the electrostatic interactions according to:[69]

$$\frac{q_i q_j}{r_{ij}} \simeq \frac{q_i q_j \text{erfc}(\beta r_{ij})}{r_{ij}} - \lim_{r_{ij} \to R_c} \left\{ \frac{q_i q_j \text{erfc}(\beta r_{ij})}{r_{ij}} \right\}, \qquad (3.3)$$

where r_{ij}, β, and R_c are the distance between atoms i and j, the damping parameter, and the cut-off radius. The Wolf method can significantly reduce the computation time compared to the traditional Ewald sum. Demontis et al.[70] suggest taking $R_c \geq 5b$ and $\beta \simeq 2/R_c$, where b corresponds to the largest of the nearest-neighbor distances between particles of opposite charge. For MOF-5, $b \simeq 2$ Å(see Fig. 3.2). Thus, we choose R_c to be 10 Å, and β to be 0.2 Å^{-1}. To find the zero-pressure lattice constant as a function temperature, simulations are run in the NPT (constant mass, pressure, and temperature) ensemble, and an average was taken over 20 ps of data. The Nose-Hoover thermostat and the Berendsen barostat are used to control the system temperature and pressure.[71]

3.3.2 Quantum effects

Below the Debye temperature, T_D, phonon mode populations in a quantum system are temperature dependent, but almost temperature independent in a classical system, such as MD.[35] By running the current simulations at temperatures above the Debye temperature, errors that may result from ignoring quantum effects when comparing to experimental data will be minimized.

The Debye temperature for a monatomic crystal is defined as [46]

$$T_{\mathrm{D}} = \frac{\hbar}{k_{\mathrm{B}}} u_{p,g} (6\pi^2 n)^{1/3}, \tag{3.4}$$

where $\hbar$ is the Planck constant divided by 2π, k_{B} is the Boltzmann constant, $u_{p,g}$ is the sound speed (an average phonon group velocity) and n is the atomic number density (N/V). For polyatomic crystals, Slack[2] ignored the optical branches and introduced a factor $1/N_c^{1/3}$ to Eq. (3.4) (N_c is the number of atoms in the unit cell). For MOF-5, where the mass and bond differences are not large between species, the correction to Eq. (3.4) is expected to be smaller than that proposed by Slack. Using Eq. (3.4) as given will thus somewhat overestimate the Debye temperature and provide a safe estimate of the temperatures for which the simulations will be comparable to experimental data.

To find the Debye temperature, a sound speed is required, which can be obtained from MD simulations using the following procedure. In the NVE ensemble, the adiabatic compressibility, κ_s, is given by [72]

$$\kappa_s = \left[\frac{2}{3}P + nk_{\mathrm{B}}T + \langle \sum_{i,j} \frac{\partial^2 \varphi}{\partial r_i \partial r_j} \rangle - \frac{N}{nk_{\mathrm{B}}T} \langle (\delta P)^2 \rangle \right]^{-1}, \tag{3.5}$$

where P is the pressure, φ is the total potential energy, and δP is the root-mean-square pressure fluctuation, i.e., $\langle (\delta P)^2 \rangle = \langle (P - \langle P \rangle)^2 \rangle$. At a temperature of 300 K, the adiabatic compressibility is found to be 7.09×10^{-10} Pa^{-1}. With the adiabatic compressibility, the longitudinal sound velocity $u_{p,g,\mathrm{L}}$ and transverse sound velocity $u_{p,g,\mathrm{T}}$ can be determined from[49, 73]

$$u_{p,g,\mathrm{L}} = \left[\frac{3(1 - 2\nu)}{\kappa_s \rho} \right]^{1/2} \tag{3.6}$$

61

$$u_{p,g,\mathrm{T}} \quad = \quad \left[\frac{3(1-2\nu)}{2(1+\nu)\kappa_s\rho} \right]^{1/2}, \qquad (3.7)$$

where ρ is density and ν is the Poisson ratio. For most solids, $\nu \simeq 0.3$. An average sound speed, $u_{p,\mathrm{A}}$, can be given by $3u_{p,\mathrm{A}}{}^{-1} = u_{p,g,\mathrm{L}}{}^{-1} + 2u_{p,g,\mathrm{T}}{}^{-1}$, which yields $u_{p,\mathrm{A}} =$ 1,184 m/s for MOF-5 at a temperature of 300 K, a reasonable value. Using Eq. (3.4) (replacing $u_{p,g}$ with $u_{p,\mathrm{A}}$), we have $T_{\mathrm{D}} \simeq 102$ K. We will consider temperatures between 200 K and 400 K (at 50 K intervals), well above the estimated T_{D}.

3.3.3   Thermal Conductivity Prediction

The thermal conductivity, k_p, is predicted using the Green-Kubo (G-K) method, where, for an isotropic material, it is given by [74]

$$k_p = \frac{1}{k_{\mathrm{B}}VT^2} \int_0^\infty \frac{\langle \dot{\boldsymbol{w}}(t) \cdot \dot{\boldsymbol{w}}(0) \rangle}{3}, \qquad (3.8)$$

where $\dot{\boldsymbol{w}}(t)$ is the heat current vector, and $\langle \dot{\boldsymbol{w}}(t) \cdot \dot{\boldsymbol{w}}(0) \rangle$ is the heat current autocorrelation function (HCACF). A slow-decaying HCACF indicates that the heat current fluctuations can spread over a long time before vanishing (i.e., a long phonon relaxation time). The heat current is given by

$$\dot{\boldsymbol{w}} = \frac{d}{dt} \sum_{i=1}^N \mathbf{r}_i E_i, \qquad (3.9)$$

where $\mathbf{r}_i$ and E_i are the position vector and the total energy of particle i.

At the beginning of a simulation for a thermal conductivity prediction, the system is run in the NVT ensemble to set the temperature. After 20 ps, when the system has reached equilibrium, the simulation is switched to run in the NVE ensemble, and the HCACF is obtained over 200 ps. At each temperature, three runs are performed
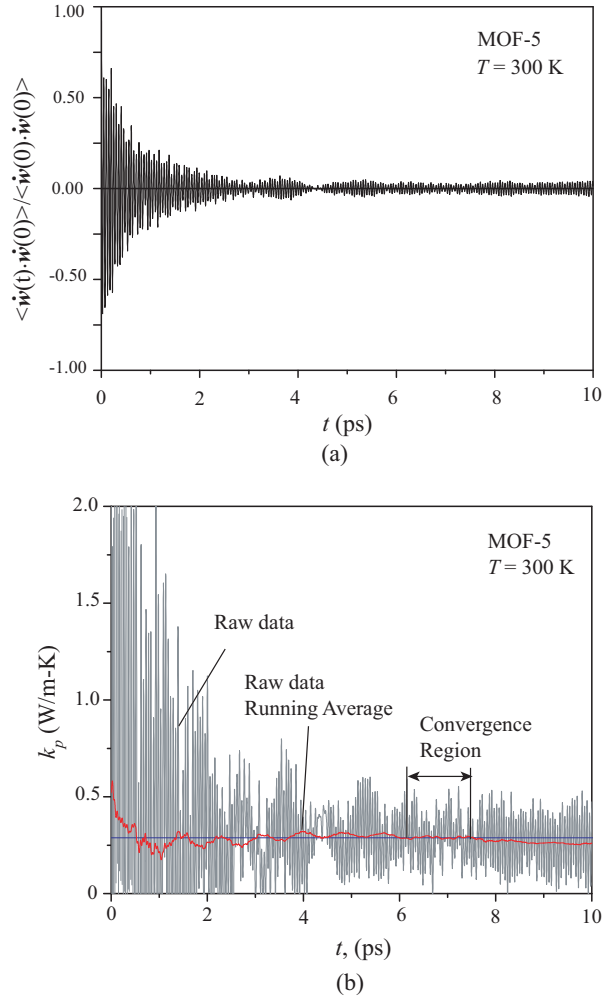
Figure 3.4: (a) Decay of the normalized HCACF for MOF-5 and (b) its integral (the thermal conductivity) at a temperature of 300 K.

unless noted. The thermal conductivity is then obtained from the integral of the HCACF.[29] A running average is applied to the integral to obtain a smooth behavior, allowing a convergence region to be defined. The decay of the normalized HCACF at a temperature of 300 K is shown in Fig. 3.4(a), and its integral, the thermal conductivity, is shown in Fig. 3.4(b). The HCACF vanishes after 6 ps. The MOF-5 HCACF has high frequency oscillations, believed to be related to optical phonons.[29]

Table 3.3: Variation of the predicted thermal conductivity of MOF-5 with respect to the simulation system size (number of cells and total number of atoms) and temperature. The number in the parentheses is the number of simulation runs and averaged to get the reported value and the uncertainty. The uncertainty for the $3 \times 3 \times 3$ system are estimated from the fluctuation of the HCACF in the converged region of the integral.

	k_p (W/m-K)		
	Simulation System Size		
T (K)	$1 \times 1 \times 1$ (328 atoms)	$2 \times 2 \times 2$ (2,624 atoms)	$3 \times 3 \times 3$ (8,856 atoms)
200	0.157 ± 0.015 (3)	0.287 ± 0.041 (3)	
250	0.167 ± 0.013 (3)	0.293 ± 0.027 (3)	
300	0.165 ± 0.007 (3)	0.308 ± 0.024 (4)	0.288 ± 0.044 (1)
350	0.150 ± 0.008 (3)	0.316 ± 0.008 (3)	0.291 ± 0.052 (1)
400	0.146 ± 0.008 (3)	0.317 ± 0.008 (3)	

3.3.4   Simulation-Size Effects

In a small simulation cell, there may not be enough phonon modes to establish scattering and transport representative of the associated bulk system.[28] Such size effects will lead to a thermal conductivity different from the infinite size (bulk) limit.[31, 30] The MD predicted thermal conductivities of MOF-5 are shown in Table 3.3, for simulation systems containing $1 \times 1 \times 1$, $2 \times 2 \times 2$ and $3 \times 3 \times 3$ unit cells (328, 2624, and 8856 atoms). The thermal conductivity of the $1 \times 1 \times 1$ system is much lower than that of the larger systems (by a factor of about two). The predictions for the $2 \times 2 \times 2$ system are very close to those for the $3 \times 3 \times 3$ system at temperatures of 300 K and 350 K, indicating that the $2 \times 2 \times 2$ system will suffice to give a converged
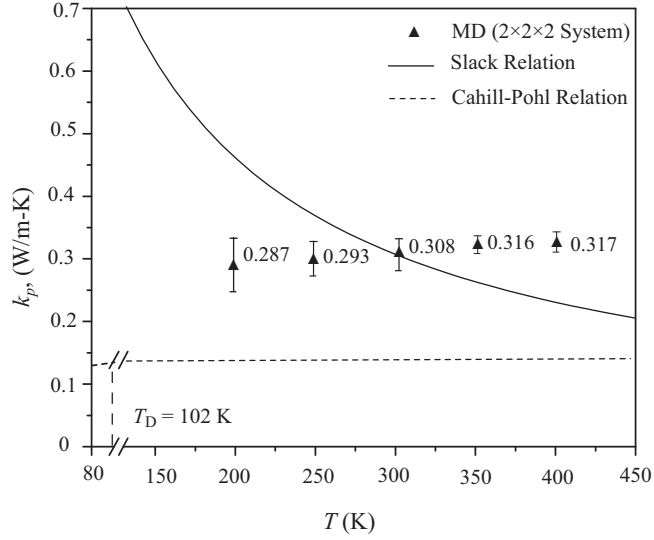
Figure 3.5: Temperature dependence of the thermal conductivity of MOF-5 predicted by MD. The Slack relation [Eq. (3.10)], using $\gamma_G = 0.45$ to fit the predicted thermal conductivity value at $T = 300$ K] and the Cahill-Pohl relation [Eq. (4.13)], using the MD predicted sound speeds] are also shown.

value.

3.4   Numerical Results and Analysis

3.4.1   Thermal Conductivity and Temperature Dependence

The $2 \times 2 \times 2$ data from Table 3.3 are plotted in Fig. 3.5. Also included in the plot are the thermal conductivity models of Slack[2] and Cahill and Pohl.[54]

Slack proposed that the thermal conductivity of crystals at temperatures above that of the experimental peak value can be approximated by the relation [39, 2]

$$k_S = \frac{3.0 \times 10^4 \langle M \rangle T_D^3}{Tn^{1/3}\gamma_G^2 N_c^{2/3}}, \tag{3.10}$$

65

where $\langle M \rangle$ is the mean atomic weight of the atoms in the unit cell (kg/kmol) and γ_G is the mode-averaged Grüneisen constant. This relation indicates that the thermal conductivity will decrease with increasing temperature as T^{-1} (other factors such as γ_G have a weak temperature dependence [39]), a prediction consistent with experimental data for many crystals.[39] The decrease in the thermal conductivity is a result of a decrease in the phonon mean-free path due to an increase in inter-phonon scattering, which itself is a result of the increasing anharmonicity brought about by the higher temperatures.[75, 76] The Slack model is plotted in Fig. 3.5 by fitting γ_G to the MD predicted thermal conductivity at a temperature of 300 K. The resulting value of γ_G is 0.45, lower than typical values between unity and two. The fit is primarily intended to allow for comparison between the trend of the Slack model and the MD data, and not as a prediction of γ_G.

Cahill and Pohl[54] developed a model for the thermal conductivity of amorphous materials by assuming that energy transfer only occurs between neighboring vibrational entities, so that the mean free path of all phonons is equal to one half of their wavelength. The thermal conductivity in this model is given by

$$k_\mathrm{CP} = \left(\frac{\pi}{6}\right)^{1/3} k_\mathrm{B} n^{2/3} \sum_{i=1}^{3} u_{p,g,i} \left(\frac{T}{T_{\mathrm{D},i}}\right)^2 \int_0^{T_{\mathrm{D},i}/T} \frac{x^3 e^x}{(e^x-1)^2} dx, \qquad (3.11)$$

and has been interpreted as a minimum solid phase thermal conductivity.[2] It is plotted in Fig. 3.5. The summation in the expression for k_CP is over the three vibration polarizations. The thermal conductivity predicted by Eq. (4.13) increases with increasing temperature, as more phonons modes are excited (a quantum effect,

related to the specific heat). When $T \gg T_{\mathrm{D}}$, Eq. (4.13) reaches its classical limit,

$$k_{\mathrm{CP},classical} = \frac{1}{2}\left(\frac{\pi}{6}\right)^{1/3} k_{\mathrm{B}} n^{2/3} \sum_{i=1}^{3} u_{p,g,i}. \qquad (3.12)$$

The thermal conductivity of MOF-5 at a temperature of 300 K is 0.31 ± 0.02 W/m-K, a very low value for a crystal. This value can be compared with the thermal conductivities of other nanoporous crystals, such as MD predictions for the zeolites sodalite (3.5 W/m-K), faujasite (2.1 W/m-K), and zeolite-A (1.7 W/m-K)[29], and experimental results for Tl_9BiTe_6 (0.39 W/m-K) [77] and amorphous silica (1.4 W/m-K) [78].

The thermal conductivity of MOF-5 is almost temperature independent. A power-law fit ($k \propto T^{\xi}$) yields a ξ value of 0.16, different from the T^{-1} high temperature dependence predicted by Eq. (3.10) and kinetic theory.[39] The behavior is more similar to that of an amorphous material. This result suggests that in the temperature range of 200 K to 400 K, the mean free path of most phonons in MOF-5 has been minimized. The quantitative difference between the MD prediction and the CP model will be discussed in the next section.

3.4.2 Thermal Conductivity Decomposition

A two-stage monotonic decay of the HCACF has been reported for crystals with a one-atom unit cell.[79, 80] In crystals with larger unit cells, optical phonons have been found to add high-frequency oscillations to the HCACF.[29] As such, we can decompose the HCACF of a crystal with a multi-atom unit cell into three parts

[acoustic short-range (A, sh), acoustic long-range (A, lg), and optical (O)] as[29]

$$\frac{\langle \dot{\boldsymbol{w}}(t) \cdot \dot{\boldsymbol{w}}(0) \rangle}{3} = A_{\mathrm{A},sh} \exp(-t/\tau_{\mathrm{A},sh}) + A_{\mathrm{A},lg} \exp(-t/\tau_{\mathrm{A},lg}) + \sum_i B_{\mathrm{O},i} \exp(-t/\tau_{\mathrm{O},i}) \cos(\omega_{\mathrm{O},i} t).$$

(3.13)

The coefficients A and B represent the strength of a given mode. The summation in the optical term corresponds to a sum over the peaks in the frequency spectrum of the HCACF.[29] Then, from Eq. (3.8), the thermal conductivity can be decomposed into three parts as

$$
\begin{aligned}
k_p &= \frac{1}{k_{\mathrm{B}} V T^2} \left(A_{\mathrm{A},sh} \tau_{\mathrm{A},sh} + A_{\mathrm{A},lg} \tau_{\mathrm{A},lg} + \sum_i \frac{B_{\mathrm{O},i} \tau_{\mathrm{O},i}}{1 + \tau_{\mathrm{O},i}^2 \omega_{\mathrm{O},i}^2} \right) \\
&\equiv k_{p,\mathrm{A},sh} + k_{p,\mathrm{A},lg} + k_{p,\mathrm{O}}.
\end{aligned}
$$

(3.14)

We first identify the optical phonon parameters by fitting to the Fourier transform of the HCACF. The resulting $k_{p,\mathrm{O}}$ values for the three simulation runs are then averaged. The fit optical component of the HCACF is then subtracted from the raw HCACF. The resultant HCACFs for the three simulation runs are then averaged and integrated, and the acoustic components are obtained by fitting the integral. The results for the decomposition of MOF-5 are listed in Table 3.4 for all the temperatures considered, and are plotted in Figure 3.6. By comparing with Table 3.3, we see that the decomposition predicts a total thermal conductivity within 5% of the value obtained from the direct integration method. Note that $k_{p,\mathrm{O}}$ contributes significantly to the thermal conductivity. This contribution is often ignored in modelling efforts due to the flatness of the associated phonon dispersion branches.[33, 34, 75] Such an assumption is justified for materials with a large thermal conductivity. [29] For a crystal with a low thermal conductivity, such as MOF-5, the optical phonon

Table 3.4: Thermal conductivity decomposition for MOF-5 and the temperature dependence of the components.

T (K)	k_p (W/m-K)	$k_{p,A,lg}$ (W/m-K)	$k_{p,A,sh}$ (W/m-K)	$k_{p,O}$ (W/m-K)
200	0.298	0.051	0.141	0.106
250	0.306	0.042	0.151	0.113
300	0.305	0.029	0.160	0.116
350	0.314	0.025	0.161	0.128
400	0.318	0.021	0.142	0.155
ξ_i ($k_{p,i} \propto T^{\xi_i}$)	0.09	-1.30	0.06	0.54

contribution cannot be ignored. A similar result was found for silica structures.[29]

The components of the thermal conductivity have different temperature dependencies: $k_{p,A,sh}$ is almost temperature independent ($\xi = 0.06$), and is close to k_{CP} at all temperatures (as was found for a series of silica structures[29]); $k_{p,O}$ increases when the temperature increases ($\xi = 0.54$), and $k_{p,A,lg}$ decreases noticeably with increasing temperature ($\xi = -1.30$). Note that only $k_{p,A,lg}$ varies with temperature approximately as T^{-1}. For MOF-5, a crystal with a low thermal conductivity, the relative contribution of the long-range acoustic phonons is small and the temperature dependence of the total thermal conductivity is thus weak. Only for those crystals in which long-range correlations dominate the heat transfer (e.g., diamond, NaCl) will the total thermal conductivity vary as T^{-1}.

To develop a theoretical description of the acoustic portion of Eq. (4.12) ($k_{p,A} \equiv k_{p,A,sh} + k_{p,A,lg}$), we begin by writing the thermal conductivity as a summation of the
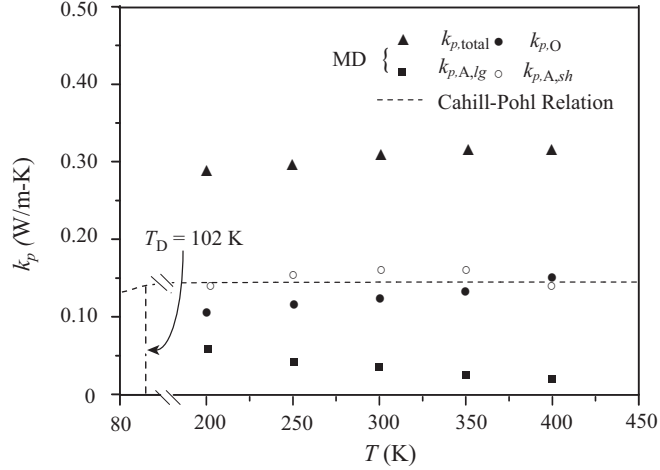
Figure 3.6: Variation of the thermal conductivity components of MOF-5 with respect to temperature and the Cahill-Pohl relation [Eq. (4.13)]. The Cahill-Pohl relation uses the temperature-independent sound speeds obtained in Section 3.3.2.

contributions of all the phonon modes as [76]

$$
\begin{aligned}
k_p &= \sum_{\kappa} \frac{1}{3} c_{v,\kappa} u_{p,g,\kappa} \lambda_{p,\kappa} \\
&= \sum_{\kappa,A} \frac{1}{3} c_{v,\kappa} u_{p,g,\kappa} \lambda_{p,\kappa} + \sum_{\kappa,O} \frac{1}{3} c_{v,\kappa} u_{p,g,\kappa} \lambda_{p,\kappa} \\
&= k_{p,A} + k_{p,O},
\end{aligned}
\tag{3.15}
$$

where $c_{v,\kappa}$, $u_{p,g,\kappa}$, and $\lambda_{p,\kappa}$, are the mode specific heat capacity, group velocity, and mean free path. Under the Debye approximation, the contribution of the acoustic phonons modes, $k_{p,A}$, can be written as [34]

$$
k_{p,A} = k_B n \sum_{i=1}^{3} u_{p,g,i} \left(\frac{T}{T_{D,i}} \right)^3 \int_0^{T_{D,i}/T} \frac{x^4 e^x}{(e^x - 1)^2} \lambda_{p,i}(x) dx,
\tag{3.16}
$$

where the summation is over the three polarization branches, x is $\hbar\omega/k_B T$ and $T_{D,i}$ is $\hbar\omega_{D,i}/k_B$ ($\omega_{D,i}$ is the Debye frequency for the ith branch). In general, the mean free path is limited by boundary scattering, impurity scattering, and interphonon

70

scattering.[34, 75] At high temperatures, interphonon scattering dominates. In the MD simulations performed here, only interphonon scattering is present. To be physically meaningful, the mean free path of a phonon mode should be longer than one half of its wavelength.[54] Starting from this idea, we construct a two-segment mean free path model. When the phonon frequency is below a critical frequency, ω_c, its mean free path will vary according to the relaxation time model of Roufosse for moderate and high temperatures (above T_D).[75, 81] When the phonon frequency is above the critical frequency, its mean free path is set to one half of its wavelength. Thus, we get

$$
\begin{aligned}
\lambda_{p,i}(\omega) &= \frac{u_{p,g,i}}{A_i(1 + B_i\omega^2)\omega^2 T}, \ \omega < \omega_{c,i}, \\
A_i &= \frac{3 \times 10^3 N_A \pi a \gamma_G^2 k_B}{2^{1/2}\langle M \rangle u_{p,g,i}^3}, \ B_i = \left(\frac{4\pi}{3}\right)^{2/3} \frac{5a^2}{12\pi^2 u_{p,g,i}^2} \\
&= \frac{\pi u_{p,g,i}}{\omega}, \ \omega_{c,i} \le \omega \le \omega_{D,i},
\end{aligned}
\tag{3.17}
$$

where a is the mean interatomic distance ($a = n^{-1/3}$) and N_A is the Avogadro number. To ensure a continuous $\lambda_{p,i}(\omega)$, ω_c must satisfy

$$
\omega_{c,i}A_i(1 + B_i\omega_{c,i}^2) = \frac{1}{\pi T}.
\tag{3.18}
$$

For $B_i \ll \pi^2 A_i^2 T^2$, we have

$$
\omega_{c,i} \simeq \frac{1}{A_i \pi T}.
\tag{3.19}
$$

For MOF-5 at a temperature of 300 K and using $u_{p,A} = 1,184$m/s, B is 9.2×10^{-27} s^2, and $\pi^2 A^2 T^2$ is 2.1×10^{-25} s^2, so that the use of Eq. (3.19) is justified. At this temperature, ω_c is 2.2 Trad/s, much less than the Debye frequency ($\omega_D = 13.4$ Trad/s), indicating that most acoustic phonons have the minimum mean free path.

71

The critical frequency ω_c decreases with temperature (for MOF-5, ω_c at temperatures of 200 K, 250 K, 300 K, 350 K, and 400 K is 3.3 Trad/s, 2.6 Trad/s, 2.2 Trad/s, 1.9 Trad/s, and 1.7 Trad/s). That is, as the temperature increases, an increasing number of phonon modes reach the limiting mean free path of one half of their wavelength. Using Eq. (3.17), Eq. (3.16) can be rewritten as

$$
\begin{aligned}
k_{p,\mathrm{A}} &= \sum_{i=1}^{3} \frac{k_\mathrm{B}}{2\pi^2 u_{p,g,i} A_i T} \int_0^{\omega_{c,i}} \left[\left(\frac{4\pi}{3} \right)^{2/3} \frac{5\omega^2 a^2}{12\pi^2 u_{p,g,i}^2} + 1 \right]^{-1} d\omega + \\
&\left(\frac{\pi}{6} \right)^{1/3} n^{2/3} \sum_{i=1}^{3} u_{p,g,i} \frac{\hbar^4}{T_{\mathrm{D},i}^2 k_\mathrm{B}^3 T^2} \int_{\omega_{c,i}}^{k_\mathrm{B} T_{\mathrm{D},i}/\hbar} \frac{\omega^3 e^{\frac{\hbar\omega}{k_\mathrm{B} T}}}{(e^{\frac{\hbar\omega}{k_\mathrm{B} T}} - 1)^2} d\omega.
\end{aligned}
\tag{3.20}
$$

Based on the construction of this model, and our knowledge of the G-K thermal conductivity decomposition, we associate the first term in Eq. (3.20) with $k_{p,\mathrm{A},lg}$ and the second term with $k_{p,\mathrm{A},sh}$. In considering Eq. (3.20), even if the temperature dependencies of the material properties and phonon dispersion are ignored, $k_{p,\mathrm{A},lg}$ still departs from T^{-1} behavior (T^ξ with $\xi < -1$). This is because ω_c decreases with temperature. At the same time, $k_{p,\mathrm{A},sh}$ increases slightly with temperature and eventually saturates. The lower ω_c, the larger the fraction of $k_{p,\mathrm{A},sh}$ in $k_{p,\mathrm{A}}$. Equation (3.20) also predicts that the temperature dependence of $k_{p,\mathrm{A}}$ will become progressively weaker as temperature increases.

In Fig. 3.7(a), the temperature dependencies of $k_{p,\mathrm{A},lg}$ and $k_{p,\mathrm{A},sh}$ predicted by the two-stage model are shown along with the MD decomposition data. The $k_{p,\mathrm{A},lg}$ component is fit to the decomposition data at 300 K by setting γ_G equal to 1.01. As with the fit to the Slack model in Fig. 3.5, the purpose of the fit is to compare the general trends, and not to specify γ_G. The agreement between the trends in the model and the MD data is good. Note that the thermal conductivity predicted by

72

Eq. (3.20) goes to infinity as the temperature goes to zero, typical of a crystal in an MD simulation, where there are no quantum effects. A simulation of MOF-5 at a temperature of 50 K (lower than T_D) gives a thermal conductivity of 2.8 W/m-K, consistent with this trend. While this numerical value cannot be compared with the experiments, it does indicate that MOF-5 behaves like a crystal in the simulations (the thermal conductivity of amorphous materials in MD decreases as the temperature decreases, consistent with experimental data[37, 82, 29]).
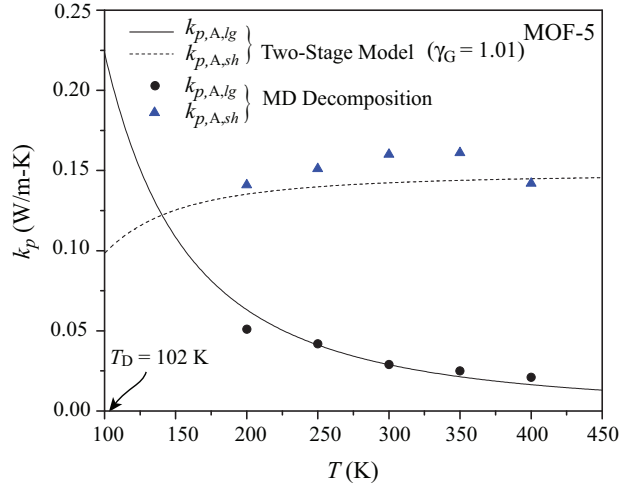
Figure 3.7: Variation of $k_{p,A,lg}$ and $k_{p,A,sh}$ with respect to temperature predicted by the two-stage model and from the MD decomposition. The longitudinal and transverse sound speeds are taken to be 1,672 m/s and 1,033 m/s (see Section 3.3.2), and γ_G is set as 1.01 to fit $k_{p,A,lg}$ at a temperature of 300 K.

By setting ω_c equal to ω_D, $u_{p,g,i}$ to the mean phonon speed $u_{p,g}$, and using $\omega_D = u_{p,g}(6\pi^2 n/N_c)^{1/3}$, we have, from Eq. (3.20),

$$k_p = k_{p,A,lg} = \frac{4.48 \times 10^3 \langle M \rangle T_D^3}{T n^{1/3} \gamma_G^2 N_c^{2/3}}, \tag{3.21}$$

which is similar to the Slack relation [Eq. (3.10)], except for the constant. The

difference in the constants is due to the single-mode relaxation time approximation and a different Hamiltonian used by Roufosse for three-phonon interactions.[75] If ω_c is equal to zero, only $k_{p,A,sh}$ contributes to $k_{p,A}$, and as expected, Eq. (3.20) reduces to Eq. (4.13). For $T/T_{D,i} \gg 1$, ω_c vanishes, and $k_{p,A}$ will reach the classical limit of k_{CP}, Eq. (3.12).

Since $k_{p,A,sh}$ and $k_{p,O}$ are small and their temperature dependencies are not strong (their sum has been interpreted as a thermal conductivity limit in crystals[29]), we may obtain a crystal with a low thermal conductivity and a weak temperature dependence by reducing ω_c. This can be accomplished by reducing the sound speed and increasing the mean interatomic distance.

3.4.3 Examination of Vibrations

The thermal conductivity of a dielectric material is related to the lattice vibrations (i.e., phonon transport). To further investigate the low thermal conductivity of MOF-5, we will calculate the partial density of states (PDOS) of the distinct atomic positions in the unit cell. The PDOS of the βth species, $D_{p,\beta}$, is determined by taking the Fourier transform of the velocity auto-correlation function, and weighting the result with the species concentration c_β:[83]

$$D_{p,\beta}(\omega) \;\; = \;\; c_\beta \int_0^\tau \Gamma_\beta(t) \cos(\omega t) dt, \tag{3.22}$$

where

$$\Gamma_\beta(t) \;\; = \;\; \sum_i^{N_\beta} \langle \mathbf{u}_{i\beta}(t) \cdot \mathbf{u}_{i\beta}(0) \rangle / \sum_i^{N_\beta} \langle \mathbf{u}_{i\beta}(0) \cdot \mathbf{u}_{i\beta}(0) \rangle. \tag{3.23}$$

The total phonon DOS is obtained by summing over the partial DOS:

$$D_p(\omega) = \sum_\beta D_{p,\beta}(\omega). \qquad (3.24)$$

The PDOS indicates the vibrational modes that specific atoms are involved with in the overall crystal lattice dynamics. In a classical system, such as an MD simulation, and in real systems well above the Debye temperature, all degrees of freedom have approximately the same expectation value for their energy. Thus, one can interpret the area under the PDOS curves as an indication of how the system energy is distributed among the atoms.

In Fig. 3.8 (a), two cages and one bridge of the MOF-5 structure are shown. In Figs. 3.8(b) and 3.8(c), the PDOS of the Oc, Zn, O, C1, C2, and C3 atoms are plotted. The C1 and C2 atoms have the same PDOS. Motivated by the decomposition of the thermal conductivity, we can examine the vibrations in both the low- and high-frequency regimes.

In the acoustic phonon modes, which end around 14 Trad/s (2.3 THz), the center oxygen atom (Oc) essentially doesn't participate. If one thinks of the heat transfer as energy moving from atom to atom, in the cage structure it will need to take a circuitous route around the Oc atom. There is also more activity in the C3 (which are a part of the phenylene ring) and O1 (which are a part of the cage) atoms than the C1/C2 atoms. The C1/C2 atoms act as a bottleneck. We interpret this result as a sign of energy localization. The phenylene ring can pivot about the axis defined by the C1-C2 bond, and yet these motions are difficult to pass onto the cage and vice versa. Energy moves back and forth across the bridge, or inside the cage, as it is
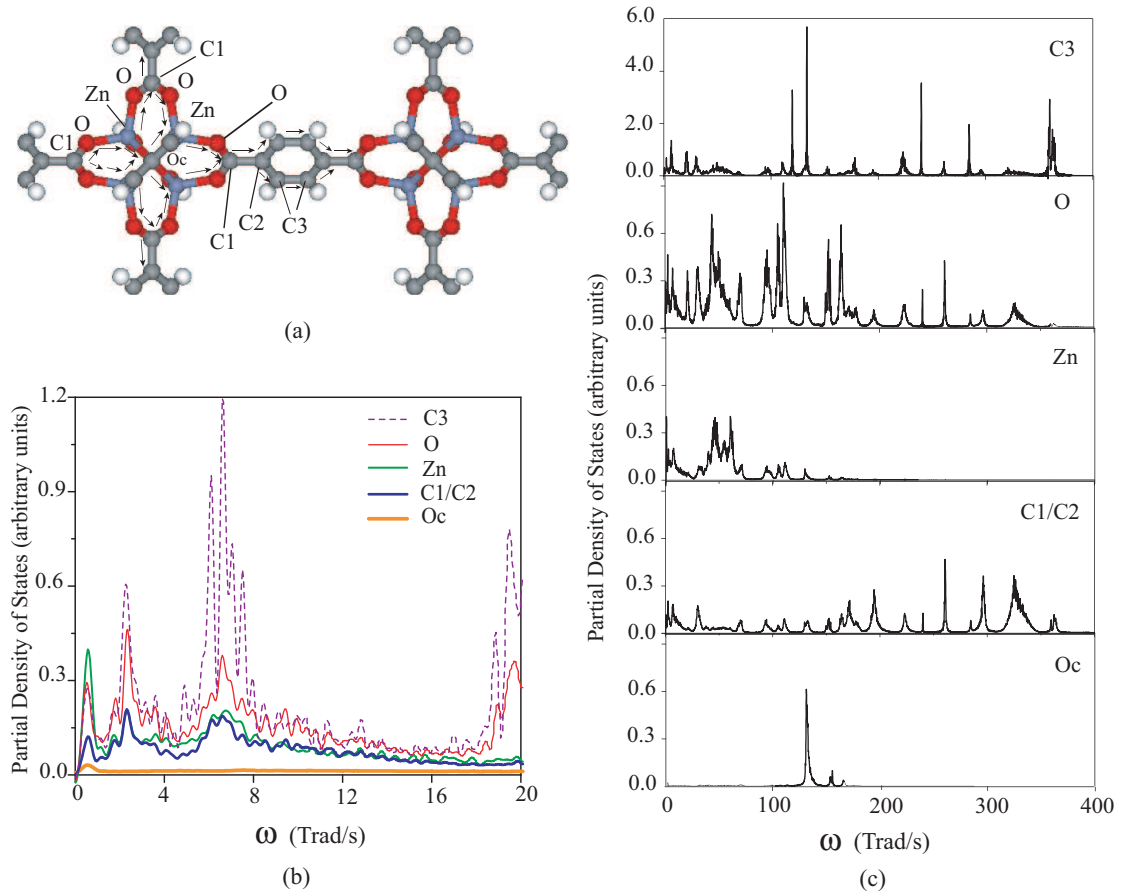
Figure 3.8: (a) Section of the MOF-5 structure. (b) and (c) PDOS of Oc, Zn, O, C1, C2, and C3 atoms in the simulation cell. Note that the scale for the C3 atoms is different than the others in (c).

reflected at the connection between them. In this way, the development of long-range correlations is suppressed. A similar trend is observed in the optical phonon spectrum of the C3 atoms. There is also scant overlap between the PDOS of the Zn and O atoms at the higher frequencies (most likely brought about by their mass difference), identifying another point in the structure where transmitting energy will be difficult. The overall picture is thus one of cages and bridges between which energy flow is restricted. This is a finding similar to that for zeolites,[29] where energy localization

on specific Si-O-Si structures was identified.

3.5   Experimental Results and Discussion

The experimental results are used to compare and verify the MD simulations. The details of the experiment, e.g., the sample preparation, measurement procedure, and the heat loss correction, is shown in Appendix B. Figure 3.9 shows the variation of the MOF-5 thermal conductivity with respect to temperature, from 6 K to 300 K. The experimental uncertainty of the absolute thermal conductivity is within $\pm 15\%$ (estimated by the standard error relation [84]). The uncertainty mainly results from the difficulty in the accurate determination of the effective cross-section area A (due to the small size and irregular shape of the sample) and the effective length of the heat flow path d (due to the junctions). The heat loss correction below 100 K is made as shown in Appendix B. Given the measured temperatures, the geometrical parameters, and the thermal conductivities of constantan, chromel, and copper[85], the heat loss at low temperature can be precisely predicted.

Since MOF-5 is a good dielectric, the thermal conductivity is from the contribution of phonons. The following processes are assumed to affect transport of phonons: grain-boundary scattering, lattice-defect scattering, and phonon-phonon scattering.[39]

To analyze the data, the average phonon mean free path $\overline{\lambda}$ is evaluated using the Debye model and the kinetic theory. The lattice thermal conductivity k_p can be
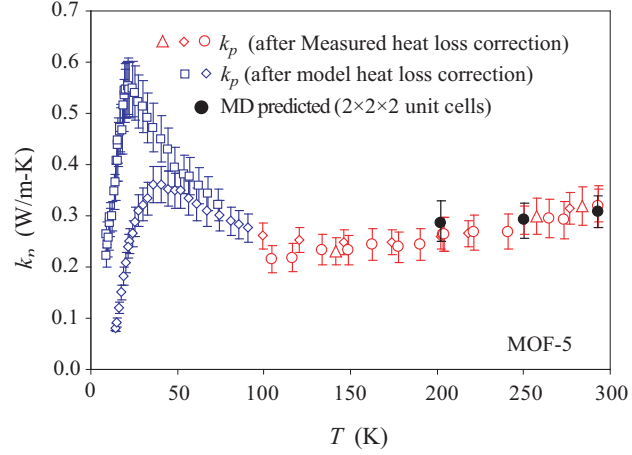
Figure 3.9: Variation of the MOF-5 thermal conductivity with respect to the temperature. Below 100 K, the heat loss correction is made by the heat loss model (Appendix B). The MD predicted result of $2 \times 2 \times 2$ unit-cell system, at 200, 250, and 300 K, are also shown [4].

written as [33]

$$k_p = \frac{k_{\mathrm{B}}}{2\pi^2 u_{p,g}} \left(\frac{k_{\mathrm{B}}T}{\hbar} \right)^3 \int_0^{T_{\mathrm{D}}/T} \frac{\tau_p x^4 e^x}{e^x - 1} \mathrm{d}x, \tag{3.25}$$

where k_{B} is the Boltzmann constant, $\hbar$ is the reduced Planck constant, T_{D} is the Debye temperature, $u_{p,g}$ is the phonon group velocity, and τ_p is the phonon scattering relaxation time. The relaxation time τ_p is normally frequency dependent, and it relates to the phonon mean free path λ through the relation $\tau_p = \lambda/u_{p,g}$.

Using Equation (3.25) and making the average, the average mean free path $\overline{\lambda}$ is given by

$$\overline{\lambda}(T) = k \left[\frac{k_{\mathrm{B}}}{2\pi^2 u_{p,g}^2} \left(\frac{k_{\mathrm{B}}T}{\hbar} \right)^3 \int_0^{T_{\mathrm{D}}/T} \frac{x^4 e^x}{e^x - 1} \mathrm{d}x \right]^{-1}. \tag{3.26}$$

We have made an estimation of the Debye temperature ($T_{\mathrm{D}} \simeq 102$ K) and the phonon group velocity ($u_{p,g} \simeq 1,184$ m/s), which is independent of the thermal conductivity prediction. Using these values in Equation (3.26), $\overline{\lambda}(T)$ is ploted in Fig. 3.10.

78
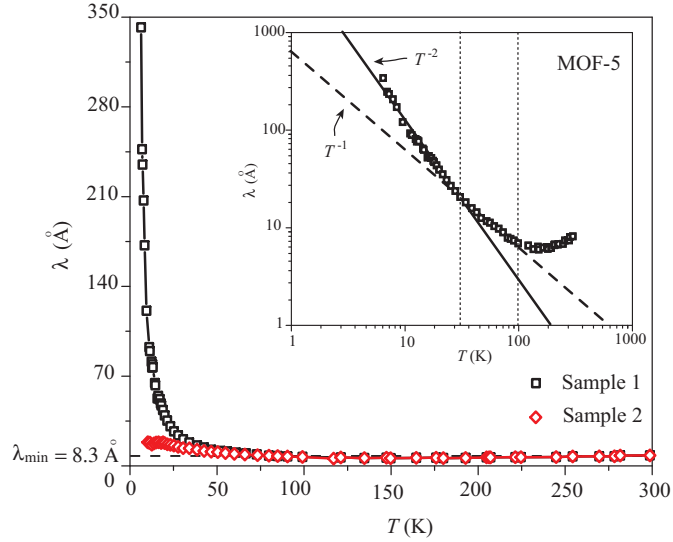
Figure 3.10: Temperature dependence of the average phonon mean free path of MOF-5. The solid and dashed lines represent the dependence T^{-2} and T^{-1}, respectively. The results are for two different samples having different impurities and sizes.

From Fig. 3.9, below 70 K, the measured thermal conductivities of the different samples are not the same (we denote the sample with higher k_p as sample 1, and the other as sample 2). The average mean free path of sample 2 is much smaller than that of sample 1 below 25 K, though they have similar dimensions. The mean free path of sample 2 reaches a limited value below 13 K, which is the typical effects of point defects (either inherent or due to thermal stresses resulting from cooling). However, $\overline{\lambda}$ of sample 1 continues to increase with decreasing temperature, suggesting this divergence is due to the different qualities of the samples. The peak in the thermal conductivity occurs at about 20 K (this is affected by the crystal quality). Below 20 K, the thermal conductivity increases sharply with increasing temperature, which is due to the excitation of more phonons at higher temperatures and is related to the increase

79

of the specific heat.[39] From Fig. 3.10, the temperature dependence of $\bar{\lambda}$ changes at about 35 K, we find that $\bar{\lambda} \propto T^{-2.16}$ (by fitting the mean free path between 6 K and 35 K). The typical interphonon scattering (U-process) will result in $\bar{\lambda} \propto T^{-1}$,[39] and the dependence of T^{-2} suggests the effects of the lattice distortion.[39, 86] The peak is just the result of the combination of the decreasing mean free path and the increasing specific heat, with the increase in temperature. From 35 K to 100 K, both k_p and $\bar{\lambda}$ decrease with increasing temperature, and $\bar{\lambda}$ shows a dependence $\bar{\lambda} \propto T^{-1.17}$, suggesting the interphonon scattering dominates.

From 100 K to 300 K, the thermal conductivity only varies about 30%, considering the experimental uncertainties, the thermal conductivity exhibits a weak temperature dependence (similar to the behavior of amorphous phase). The MD predictions at 200, 250 and 300 K, shown in Fig. 3.9, agree quite well with the measured value.

At 300 K, the thermal conductivity of MOF-5 is only 0.32 W/m-K, a rather low value for crystals. This value can be compared with the thermal conductivities of other nanoporous crystals, such as the MD predicted value for the zeolites sodalite (3.53 W/m-K), faujasite (2.07 W/m-K), and zeolite-A (1.68 W/m-K)[29]. The weak temperature dependence of the thermal conductivity is a common character for the nanoporous crystals.[29] Figure 3.10 shows that $\bar{\lambda}$ is almost a constant above 100 K, indicating the minimization of phonon mean free path. Similar phenomena are found for other crystals.[86] The minimum mean free path of MOF-5 is about 8.3 Å, much smaller than the lattice constant (25.85 Å), but close to the cage size (7.16 Å). In the accompanying manuscript, we show that it is the carboxylate-carbon atom that limits the transport of the acoustic phonons, that is, the acoustic phonons are reflected at

the connector between the cage and the bridge.[4] Considering most acoustic vibration modes lie in the cage, it is reasonable for the minimum $\overline{\lambda}$ to be close to the size of the cage. The low thermal conductivity and its temperature independence occur when most phonons reach their minimum mean free paths. In such a situation, the interphonon scattering cannot further reduce the phonon mean free paths and the energy is transmitted by activation or hopping of the localized modes, which is similar to the behavior of the amorphous phase [76].

3.6   Simple Model for Phonon Conductivity

Just like MOF-5, many linked-cage structure includes complex multiatomic cages connecting by relatively simple bridges [see Fig. 3.11)] (sometimes the cages may also be joined directly without bridges). In such a structure, the atoms in the cage are normally much more than the atoms acting as connectors. Zeolites and MOFs are good examples of such structures. Some siliceous zeolites, e.g., LTA, FAU and SOD, contain the complex sodalite cage built from SiO_4 tetrahedra [29].

Many molecular crystals consist of large, complex molecules held together by weak van der Waals interactions or hydrogen bonds. The intramolecular interactions are much stiffer than the intermolecular interactions. They can also be considered a special type of linked-cage structure, and each complex molecule can be considered a cage.

When $T \geq T_D$, all the vibration modes will have the same contribution to the total vibration energy. Since most atoms lie in the cage, most vibration energy is

located in the cage and a fraction of the vibration energy transports to the next cage through connectors. However, the large coordination number difference or bond stiffness difference make the connector a bottleneck for the energy transport, and most phonon energy is localized in the cage, or reflected at the connectors. McGaughey and Kaviany [29] showed that the Si-O-Si bonds contribute to the energy localization in FAU- and SOD-zeolites. Our work for MOF-5 [4] also showed the carbon connector limits the transport of phonon energy. An indicator of this phenomena is the large difference between the phonon partial density of states (PDOS, weighted by the concentration of atoms) of the cage and that of the connectors (as shown in [4]). Therefore, the connectors will act as scatterers in the structure. If the cage is relatively rigid (phonons experience little scattering within the cage), the phonon mean-free path will be limited by the distance between the connectors at the boundary of the cage, which is often the same as the cage size w. For molecular crystals, w is essentially the dimension of the molecule. Then we have

$$k_p = \frac{1}{3} n_a c_v u_{p,g} w. \tag{3.27}$$

When the temperature is higher than the Debye temperature, c_v can be simply set as $3k_\mathrm{B}$.

This simple mean-free path model for the linked-cage structures leads to good agreement with the experimental values or the MD results, as shown in Table 3.5 and Fig. 3.11. The values calculated by the Slack relation (k_CP) are also shown, and it is apparent that k_CP has a lower value.

When the temperature decreases, the high frequency phonon modes caused by

82
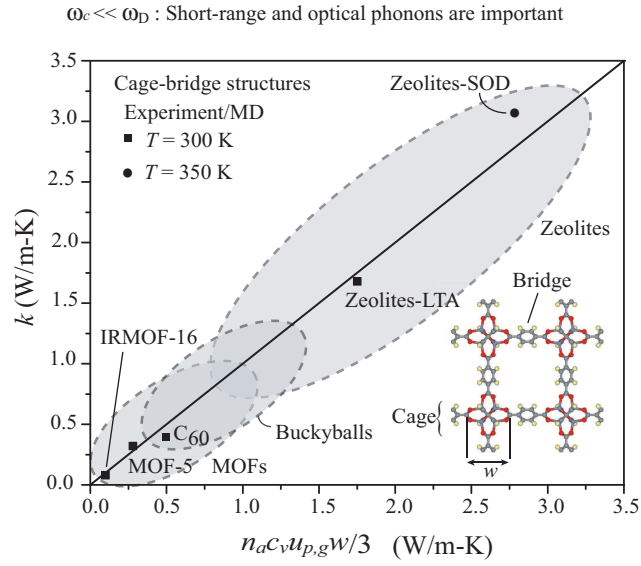
Figure 3.11: Comparison of the calculated thermal conductivities of some linked-cage crystals with the experimental or MD results.

the internal vibrations of the cage will decrease much faster than the low frequency modes, and the fraction of localized energy will decrease. When the temperature is much lower than the Debye temperature, the fraction of localized vibration energy will be small and the phonon mean-free path will no longer be limited by the cage size.

Table 3.5: Comparison of predicted thermal conductivities of some linked-cage structures calculated by Eq. (3.27) and the Slack relation, with the experimental and the MD results.

Crystals	T (K)	$u_{p,g}$ (m/s)	w (Å)	k_p (W/m-K)		
				Eq. (3.27)	$k_{p,S}$	Exp./MD
MOF-5[a]	300	1184	7.16	0.28	0.025	0.32
IRMOF-16[a]	300	600	7.16	0.10	0.01	0.08
SOD	350	4200[b]	8.88	2.79	1.58	3.09[c]
LTA	300	3200[b]	8.88	1.75	0.47	1.68[c]
C_{60}	260	2000[d]	7.00	0.52	0.007	0.4[e]

[a] values for MOF-5 are taken from reference [4]. The data for IRMOF-16 is calculated by MD using the same potentials;

[b] values are derived from the bulk modulus [48], by setting poisson ratio as 0.3;

[c] values are taken from MD results from reference [29];

[d] values are derived from the bulk modulus [87];

[e] values are from reference [88].

Chapter 4

Phonon and Electron Transport in Layered Bi$_2$Te$_3$ Structure

4.1 Introduction of Bismuth Telluride

Efficient solid state energy conversion devices based on the thermoelectric (TE) effects, i.e., the Peltier effect for cooling and the Seebeck effect for power generation, have great application potentials and economic benefits in many areas. However, present TE devices have a very low efficiency, which is directly limited by the performance of TE materials. Search into the fundamentals and improvements in TE transport phenomena continues. The performance of TE materials is presented by the dimensionless figure of merit (ZT)

$$ZT \;=\; \alpha_S^2 \sigma_e T / (k_e + k_p), \tag{4.1}$$

where α_S is the Seebeck coefficient, σ_e is the electrical conductivity, T is the temperature, and k_e and k_p are the electric and lattice thermal conductivity, respectively. Identifying and designing materials with high ZT has proven to be very challenging. Currently the best bulk commercial TE materials for applications near room temperature are still the compounds based on Bi_2Te_3, with ZT near 1. Bi_2Te_3 exhibits many typical features of a good room-temperature TE material, such as a narrow band gap, high density of states near the band edges, and low total thermal conductivity. Understanding phonon and electron transport in Bi_2Te_3 is important in design and optimization of TE materials.

Bulk Bi_2Te_3 has a rhombohedral lattice structure which belongs to the space group D_{3d}^5 ($R\bar{3}m$) and contains 5 atoms along the trigonal axis in the sequence of Te1-Bi-Te2-Bi-Te1 (Fig. 4.1). At 293 K, the rhombohedral unit-cell parameters[5] are $a_R = 10.473$ Å, $\theta_R = 24.159°$, and the corresponding hexognal unit-cell parameters are $a = 10.473$ Å, $c = 30.487$ Å. In the rhombohedral structure, the fractional coordinates for Te1 atoms are designated as $(\pm u, \pm u, \pm u)$ and those for Bi as $(\pm v, \pm v, \pm v)$, where u and v at 293 K have been found[89] to be 0.4001 and 0.2095. In the hexognal unit cell (Fig. 4.1), it is apparent that Bi_2Te_3 has a lamella structure made of Te1-Bi-Te2-Bi-Te1 blocks. The bond length of the Te1-Bi bond is 3.07 Å shorter than that of the Bi-Te2 bond (3.25 Å), indicating that they may be of different bond types; the Te1-Te1 bond is the longest (3.64 Å) and is believed to be van der Waals interaction, which responses to the ease of cleavage along the planes [5, 89]. We denote the direction along the c axis (cross-plane direction) as "$\perp$" and the in-plane direction as "$\parallel$".
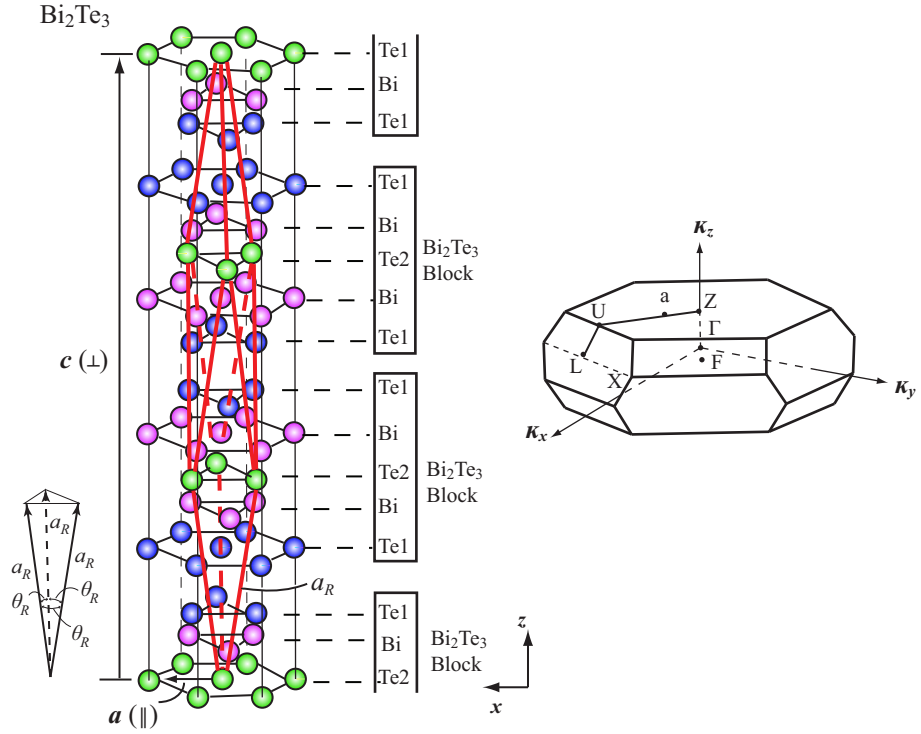
Figure 4.1: Crystal structure of Bi_2Te_3 showing both the rhombohedral and hexognal unit cells. The first Brillouin zone for the rhombohedral cell and some symmetry axes and κ points are also shown. The hexogonal structure is made of Te1-Bi-Te2-Bi-Te1 five-layer blocks.

Significant experimental characterization efforts [5, 89, 7, 90, 16, 91, 92, 93, 94] on Bi_2Te_3 and some *ab initio* calculations and theoretical treatments [7, 16, 20] have been reported. However, theoretical treatments for both the phonon and electron transport in Bi_2Te_3 are rare, especially for the lattice thermal conductivity. The difficulty has been due to the different physical features of phonon and electron transport, and a multi-scale approach is required for such investigations.

In order to systematically study the relationship between the TE properties and the structural features and understand the transport mechanisms in TE materials, we

develop a comprehensive strategy to calculate all the TE transport properties (α_S, σ_e, k_e, and k_p). In this strategy, first-principle calculations based on density functional theory (DFT), molecular dynamics (MD) simulations, and Boltzmann transport equation (BTE) are combined to calculate the TE transport properties of Bi_2Te_3. Below, we first report the classical interatomic potentials for Bi_2Te_3 developed on the basis of DFT energy calculations. With these potentials, the lattice vibrations are analyzed using MD simulations. Then the lattice thermal conductivity along the in-plane and cross-plane directions are calculated in a temperature range from 150 K to 450 K, using MD combined with the Green-Kubo (G-K) autocorrelation decay method. For electric transport, we start with the first-principle band structure calculations and the modeling for the chemical potential. Then the electric transport properties (α_S, σ_e, and k_e) are determined using BTE with the appropriate modeling of the relaxation time and chemical potential between 100 K and 500 K. The calculated results are in reasonable agreement with the experiments, noting that the experiments inherently contain various defects.

4.2 Prediction of Phonon Conductivity

There are two common theoretical approaches in the investigation of phonon transport in solids. One is the continuum transport theory (or kinetic theory), such as BTE [33, 34], which is suitable for fast calculations of large systems. However, this normally needs some parameter input from experiments or other predictions, therefore its application is limited. The other is the atomistic technique, such as MD

simulations. Unlike BTE, MD only requires material structures and suitable inter-atomic potentials. In a sense, MD is more fundamental and can provide insight into the lattice dynamics at the atomic level. Also, MD allows for decomposing different transport mechanisms, and therefore, is chosen here.

4.2.1   Interatomic Potentials

Suitable interatomic potentials are essential for modeling the lattice dynamics of Bi_2Te_3 in the MD simulations. Though there are already some simple harmonic potentials fitted using the experiments in the literature [7, 16], they are not suitable for the calculation of lattice conductivity due to the omitted anharmonic effects. Here, the interatomic potentials involving the anharmonic terms have been developed by fitting the energy surface from the *ab initio* calculations. The *ab initio* energy surface scan is normally carried out by considering only small isolated clusters. This approach is valid only when the interatomic interactions in a real crystal are mainly of short range. However, long-range interactions, e.g., van der Waals interactions, may be important in determining the structure and dynamics of Bi_2Te_3.[7] Therefore, a crystal structure with periodic boundary condition was adopted in the energy surface scan.

The *ab initio* calculations were performed with Quantum-ESPRESSO package [95] within DFT framework, using a plane-wave basis set and pseudopotentials adopting the Ceperley-Alder LDA with Perdew-Zunger data (PZ). A cut-off energy of 50 Ry was used and the spin–orbit coupling was included. The energy surface of Bi_2Te_3 was scanned by changing the bond lengths and angles. Both a rhombohedral primitive

cell and a hexagonal representation were used in the scan. The classical potentials with predetermined forms were first fitted to these data using the GULP code[64]. Then, the crystal structure and other properties such as the elastic constants were calculated by implementing those potentials in the GULP package and compared with experimental results. Such procedures iterated until convergent results were achieved. Note that the DFT with the generalized-gradient (GGA) or local (LDA) density approximations can not describe the true long-range van der Waals interactions[96]. Though recent developments[96] have seamlessly included van der Waals interactions in DFT, the solutions are not very simple and are unavailable in most present DFT codes. In this work, the van der Waals interactions were first parameterized by fitting the energy surface scanned by Quantum-ESPRESSO and subsequently refined by fitting to the structure and elastic constants. In the fitting with the energy surface, we adopted the atomic charges fitted by Kullmann et al. [16] The final forms of the interatomic potentials are listed in Table 5.3.

It is interesting to note that the Te1-Bi bond has a higher bond energy and higher force constant than the Te2-Bi bond, also its potential has a larger spatial variation than the Te2-Bi bond, showing a stronger bond anharmonicity. This indicates that the Te1-Bi bond is more ionic than the Te2-Bi bond. The Te1-Te1 bond, which is commonly considered as a van der Waals interaction, has a bond energy $\varphi_{\circ} = 0.0691$ eV, lower than that of a typical ionic or covalent bond but much higher than the bond energy of the Xe-Xe or Kr-Kr van der Waals interaction (for Xe-Xe, $\varphi_{\circ} = 0.014$ eV, and for Kr-Kr, $\varphi_{\circ} = 0.02$ eV)[14], which have a close filled-shell atomic radius. Also, the force constant Γ of Te1-Te1 at the equilibrium site is 10.45 N/m, which

Table 4.1: Interatomic potentials (excluding the electrostatic interactions) for Bi_2Te_3. Here r and θ are interatomic separation distance and bond angle. The cut-off radius of the electrostatic terms is 12 Å. The atomic charges of Te1, Bi, and Te2 are -0.26, 0.38, -0.24, respectively [16].

Interaction	Potential Model	Parameters
Pair		
Te1-Bi (adjacent layers)	$\varphi_\circ\{[1 - \exp(-a(r - r_\circ))]^2 - 1\}$	$\varphi_\circ = 0.974$ eV, $a = 1.2848$ Å^{-1}, $r_\circ = 3.10$ Å
Te2-Bi (adjacent layers)	$\varphi_\circ\{[1 - \exp(-a(r - r_\circ))]^2 - 1\}$	$\varphi_\circ = 0.5801$ eV, $a = 1.2537$ Å^{-1}, $r_\circ = 3.235$ Å
Te1-Te1 (adjacent layers)	$\varphi_\circ\{[1 - \exp(-a(r - r_\circ))]^2 - 1\}$	$\varphi_\circ = 0.0691$ eV, $a = 2.174$ Å^{-1}, $r_\circ = 3.64$ Å
Bi-Bi (same layer)	$\varphi_\circ\{[1 - \exp(-a(r - r_\circ))]^2 - 1\}$	$\varphi_\circ = 0.085$ eV, $a = 1.93$ Å^{-1}, $r_\circ = 4.18$ Å
Angular		
Te1-Bi-Te1 (adjacent layers)	$\frac{1}{2}\varphi_\theta(\cos\theta - \cos\theta_\circ)^2$	$\varphi_\theta = 0.56$ eV, $\theta_\circ = 90°$
Bi-Te1-Bi (adjacent layers)	$\frac{1}{2}\varphi_\theta(\cos\theta - \cos\theta_\circ)^2$	$\varphi_\theta = 1.31$ eV, $\theta_\circ = 90°$
Te2-Bi-Te2 (adjacent layers)	$\frac{1}{2}\varphi_\theta(\cos\theta - \cos\theta_\circ)^2$	$\varphi_\theta = 1.47$ eV, $\theta_\circ = 85°$
Bi-Te2-Bi (adjacent layers)	$\frac{1}{2}\varphi_\theta(\cos\theta - \cos\theta_\circ)^2$	$\varphi_\theta = 1.47$ eV, $\theta_\circ = 85°$
Te2-Bi-Te1 (adjacent 3 layers)	$\frac{1}{2}\varphi_\theta(\cos\theta - \cos\theta_\circ)^2$	$\varphi_\theta = 1.16$ eV, $\theta_\circ = 92°$
Bi-Te2-Bi (adjacent 3 layers)	$\frac{1}{2}\varphi_\theta(\cos\theta - \cos\theta_\circ)^2$	$\varphi_\theta = 1.18$ eV, $\theta_\circ = 95°$

is also much larger than those of Xe-Xe ($\Gamma = 0.96$ N/m) and Kr-Kr ($\Gamma = 1.15$ N/m)[14]. This value agrees well with the results of Jenkins et al[7] ($\Gamma = 9.83$ N/m) and Kullmann et al. [16] (7.98 N/m). The large bond energy, the force constants and large spatial variation of the Te1-Te1 interaction indicates that the Te1-Te1 (excluding electrostatic interaction) interaction may be special. As will be discussed in Section 4.3.1, the interatomic bonds in each quintuple layer are primarily the $pp\sigma$ interactions.

We applied these potentials in the GULP package to optimize the structure (energy minimization). The resulting c and a values at 0 K are listed in Fig. 4.2, compared with the values measured[6] at 4 K. Since structure parameters at low temperatures are unavailable, we also used MD to obtain the average bond lengthes and angles in a free-standing structure at 300 K, and the comparisons with the experimental results measured[5, 89] at 293 K are shown in Fig. 4.2. The overall agreement is good (the average deviation from the measured data is less than 1%). The calculated Te1-Te1 bond length at 0 K (not shown) in the crystal is 3.62 Å, shorter than the equilibrium bond length parameter 3.64 Å listed in Table 5.3. This indicates the repulsion between the adjacent two Te1 layers is overwhelmed by the electrostatic interaction between the distant Bi layers and Te1 layers in two neighboring blocks. However, at high temperature, as shown in Fig. 4.2, the attraction between the two adjacent Te1 layers originates from both the electrostatic interaction and the weak Te1-Te1 bonds. The combination of the electrostatic interaction and the strong van der Waals interaction make the net Te1-Te1 interaction behave as an ionic bond.

The elastic constants (the elastic modula $C_{\alpha\beta}$, bulk modulus E_p and Young modulus E_Y) of the optimized structure are also calculated using the dynamical matrix approach implemented in the GULP package. In performing the lattice dynamical calculation, the Cartesian reference axis is chosen as the same as in the reference [7]. The calculated results apply to 0 K. Table 4.2 compares the elastic constants of the optimized structure with the experimental data at different temperatures [7, 16]. Except for C13, our data for the optimized structure at 0 K agree quite well with the elastic constants at 0 K measured by Jenkins et al.[7], and the average deviation

T (K)	a (Å)	c (Å)	
0	4.36	30.38	Calculated
300	4.37	30.51	
4.2	4.37	30.34	Reference [17]
293	4.38	30.49	Reference [1]
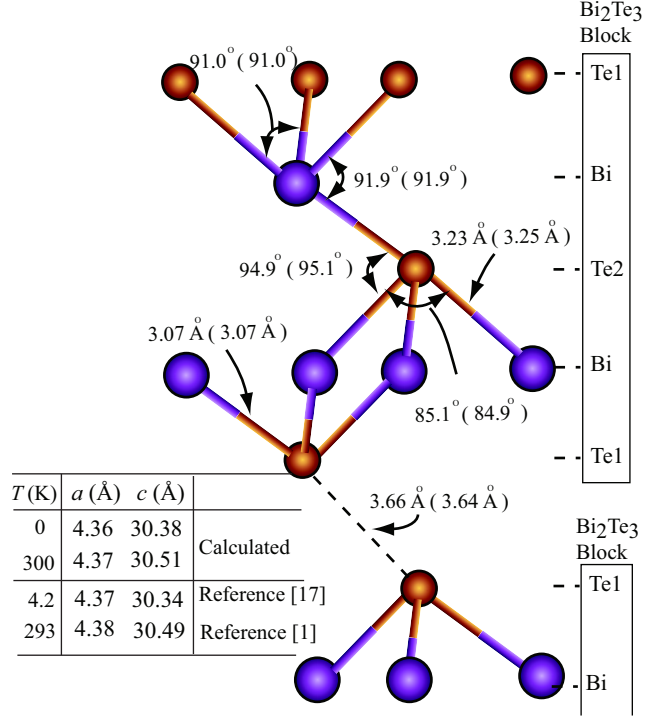
Figure 4.2: Comparison of the structure parameters calculated by the model at 300 K with those[5, 6] (shown in the parentheses) from experiments at 293 K. The calculated lattice parameters at 0 K and 300 K, together with the experimental results[5, 6], are also shown.

from the measured values is less than 10%. We also calculate the elastic constants of a free-standing structure at 300 K. As shown in Table 4.2, the changes of the elastic constants $\Delta C_{\alpha\beta}$ agree quite well with the experiments. This indicates that these potential can be used to describe the harmonic behaviors of Bi_2Te_3 over a wide temperature range. Also, note that C11 is only slightly larger than C33 because of the high force constant of Te1-Te1 bonds, which shows weak anisotropy in the elastic properties of the layered Bi_2Te_3 structure.

The Umklapp processes, in which the phonon momentum is changed by a recip-

Table 4.2: Comparison of the calculated elastic modula $C_{\alpha\beta}$, bulk modulus E_p and the in-plane Young modulus E_Y (in GPa) with experimental results[7, 16].

	C11	C13	C14	C33	C44	C66	E_p	E_Y
Ultrasonic Experiment (280 K)[7]	68.5	27.0	13.3	47.7	27.4	23.4	37.4	54.2
Ultrasonic Experiment (0 K)[7]	74.4	29.2	15.4	51.6	29.2	26.2	39.5^a	-
Neutron Scattering Experiment (77 K)[16]	76.3	-	13.2	51.2	30.9	9.9	-	-
This study (0 K)	69.0	21.6	12.3	54.8	28.8	26.7	34.4	52.5
This study (300 K)	65.4	19.0	10.9	50.7	26.5	25.7	31.6	51.4

[a] calculated through the bulk modulus relation in the reference [7].

rocal lattice vector, dominate the lattice thermal conductivity of crystalline materials at normal and high temperature (typically above 1/3-1/2 of the Debye temperature). This intrinsic resistive process results from the anharmonicity of the interatomic potentials in solids. Its strength depends on both the available phonon phase and the phonon-phonon scattering matrix, which are in turn determined by the harmonic force constants and anharmonicity of the interatomic potentials, respectively [97]. Therefore, we chose the Grüneisen parameter and the linear thermal expansion coefficients to check the anharmonicity of the interatomic potentials before applying them in the thermal conductivity calculations.

The mode Grüneisen parameter $\gamma_{G,\kappa,s}$ describes the relative shift of phonon frequency of the mode (κ, s) with the change of the volume and is defined as

$$\gamma_{G,\kappa,s} = -\frac{V}{\omega_s(\kappa)}\frac{\partial \omega_s(\kappa)}{\partial V},\tag{4.2}$$

where the mode is denoted by the wave vector κ and the branch identifier s, ω is the angular frequency and V is the volume. The overall Grüneisen parameter is defined

as

$$\gamma_{\mathrm{G}} = \frac{\sum_{\boldsymbol{\kappa},s} \gamma_{\boldsymbol{\kappa},\alpha} c_{v,s}(\boldsymbol{\kappa})}{\sum_{\boldsymbol{\kappa},s} c_{v,j}(\boldsymbol{\kappa})}, \quad c_{v,s}(\boldsymbol{\kappa}) = \frac{\hbar\omega_s(\boldsymbol{\kappa})}{V}\frac{\partial}{\partial T}\Big[\frac{1}{e^{\hbar\omega_s(\boldsymbol{\kappa})/k_{\mathrm{B}}T}-1}\Big] = \frac{\beta E_p}{c_v}, \qquad (4.3)$$

where $c_{v,s}(\boldsymbol{\kappa})$ is the contribution of the mode $(\boldsymbol{\kappa},\, s)$ to the volumetric specific heat c_v, and β is the volumetric thermal expansion coefficient. To calculate the volume dependence of the phonon frequencies in Eq. (4.2), we used GULP to calculate the volume of a hexagonal unit cell under different hydrostatic pressures p by minimizing the enthalpy of the system. With the resulting new structure, the phonon frequency at each $\boldsymbol{\kappa}$ point was recalculated by diagonalizing the corresponding dynamical matrix (a $6 \times 6 \times 6$ $\boldsymbol{\kappa}$ mesh was used). The Grüneisen parameter was then calculated from the changes in the phonon frequencies and listed in Table 4.3.

The linear thermal expansion coefficient β_α was obtained from the elastic compliance coefficient S_{ij}, and from the generalized Grüneisen parameters, which are defined as [98]

$$\gamma'_{\mathrm{G},\alpha} = \frac{\sum_{\boldsymbol{\kappa},s} \gamma'_{\alpha,\boldsymbol{\kappa},s} c_{v,s}(\boldsymbol{\kappa})}{\sum_{\boldsymbol{\kappa},s} c_{v,s}(\boldsymbol{\kappa})}, \quad \gamma'_{\mathrm{G},\alpha,\boldsymbol{\kappa},s} = -\frac{1}{\omega_s \boldsymbol{\kappa}}\frac{\partial \omega_s(\boldsymbol{\kappa})}{\partial \epsilon_\alpha}, \qquad (4.4)$$

where ϵ_α is a uniform areal strain along the α direction. The linear thermal expansion coefficients of a hexagonal crystal can be obtained from [98]

$$\beta_\parallel = [(S_{11} + S_{12})\gamma'_\parallel + S_{13}\gamma'_\perp]c_v \qquad (4.5)$$

$$\beta_\perp = [2S_{13}\gamma'_\parallel + S_{33}\gamma'_\perp]c_v. \qquad (4.6)$$

The corresponding volumetric thermal expansion coefficient β is

$$\beta = 2\beta_\parallel + \beta_\perp. \qquad (4.7)$$

Table 4.3: Comparison of the calculated Grüneisen parameters and thermal expansion coefficients, at $T = 293$ K, with the experimental results[7, 5, 17].

Parameter	γ_{G}	$\gamma_{\mathrm{G},\parallel}$	$\gamma_{\mathrm{G},\perp}$	β (10^{-6}/K)	$\beta_{\parallel}$ (10^{-6}/K)	$\beta_{\perp}$ (10^{-6}/K)
Experiment	1.49[7]	-	-	48.0[5], 44.0[17]	12.9[5], 13.0[17]	22.2[5], 18.0[17]
Calculation	1.40	1.17	1.86	46.8	12.9	21.0

The calculated results and those from experiments at $T = 300$ K are also listed in Table 4.3.

From Table 4.3, the calculated anharmonic properties agree well with the experimental results. Therefore, we would expect this set of interatomic potentials to provide a reasonable prediction for the lattice thermal conductivities.

Since Bi_2Te_3 is a highly anisotropic layered structure, to characterize the anharmonicities along different polarizations, similar to Eq. (4.3), we can also define a polarized Grüneisen parameter

$$\gamma_{\mathrm{G},\alpha} = \frac{3\beta_\alpha E_p}{c_v},$$
(4.8)

which measures the anharmonicity along α direction and equates to γ_{G} if the structure is isotropic ($\gamma_{\mathrm{G}} = \sum_\alpha \gamma_{\mathrm{G},\alpha}/3$). Table 4.3 shows the in-plane Grüneisen parameter $\gamma_{\mathrm{G},\parallel}$ is close to the γ_{G} value of an ideal covalent material [99] and much smaller than the cross-plane Grüneisen parameter $\gamma_{\mathrm{G},\perp}$, indicating the in-plane anharmonic scattering is much weaker than the cross-plane anharmonic scattering. The calculated $\gamma_{\mathrm{G},\perp}$, however, is a typical value of an ionic material, which confirms the conclusion about the Te1-Te1 ionic-like mixed bond.

4.2.2　Lattice Vibrations

To further investigate the lattice vibrations of Bi_2Te_3, we also used the MD simulations to calculate the normalized total phonon density of states (DOS) [Fig. 4.3(a)] together with the atomic partial phonon density of states (PDOS) (Fig. 4.4). The normalized PDOS of the βth species in the α direction, $D^*_{p,\beta,\alpha}$, is determined by taking the Fourier transform of the velocity auto-correlation function (1800 ps raw velocity data were used in the autocorrelation calculation) [49, 100]

$$D^*_{p,\beta,\alpha}(\omega) \;\; = \;\; \frac{\int \exp(-i\omega t)\langle u_{\beta,\alpha}(t)u_{\beta,\alpha}(0)\rangle \mathrm{d}t}{\int\int \exp(-i\omega t)\langle u_{i,\beta,\alpha}(t)u_{i,\beta,\alpha}(0)\rangle \mathrm{d}t\mathrm{d}\omega}, \tag{4.9}$$

where $u_{\beta,\alpha}$ denotes the velocity of an atom of the βth species in the α direction.

The normalized total phonon DOS is obtained by summing over the normalized partial DOS weighted with the speceies concentration c_β

$$D^*_p(\omega) = \sum_{\beta,\alpha} c_\beta D^*_{p,\beta,\alpha}(\omega). \tag{4.10}$$

To obtain the DOS and PDOS, the MD simulations were run at 300 K and 1800 ps raw velocity data were used in the calculation for the autocorrelation function. The obtained total phonon DOS is shown in Fig. 4.3. The generalized phonon density of states $G(\omega)$ measured at 77 K by Rauh et al. [8] using the inelastic neutron scattering, and that calculated by Jenkins et al. [7] with the assumed Born-von Karman model, are also shown in Fig. 4.3. Note that the $G(\omega)$ measured by Rauh et al.[8] is not the conventional DOS because the difference of the weight factors is significant for Bi and Te. The cut-off frequency calculated by the MD simulation is 4.7 THz, larger than the value 4.3 THz calculated by Jenkins et al.[7] but agreeing well with the value 4.7

97

THz measured by Rauh et al. [8] and 4.55 THz measured by Kullmann et al.[16] Overall, our DOS results agree fairly well with that of Jenkins et al.[7] In our DOS results, there is a gap between 2.5 THz and 2.9 THz, which is mainly determined by the weak Te1-Te1 bond and the Te2-Bi bond. Neither our model nor that of Jenkins et al.[7] can reproduce the transversal eigen mode around 1.0 THz. This may be due to the simple nature of the "rigid-ion" model, since the high polarizability of Te and Bi may significantly influence the dispersion behavior of the transverse optical mode. A suitable core-shell model may account for this problem, which will be investigated in the future.
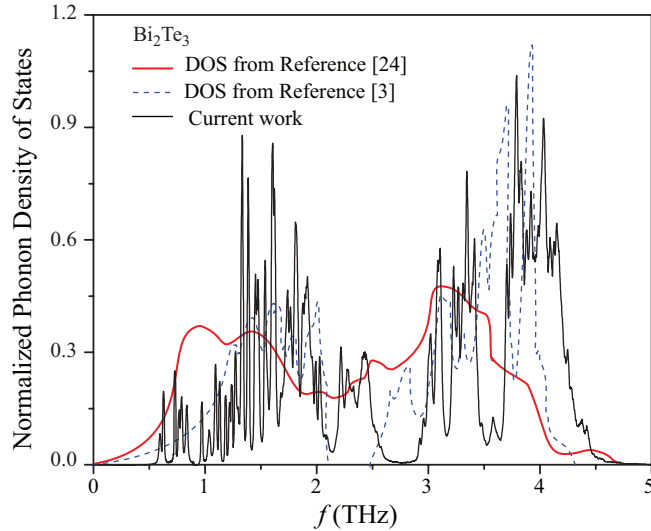
Figure 4.3: Predicted variation of the normalized phonon DOS for Bi_2Te_3 with respcet to frequency, and the comparison with the available DOS [7, 8].

Figure 4.4(a) shows the normalized in-plane and cross-plane phonon DOS of the entire Bi_2Te_3 structure and those of the different species. Overall, the in-plane and cross-plane phonon DOS almost overlaps, especially when $f < 3$ THz, and the differ-
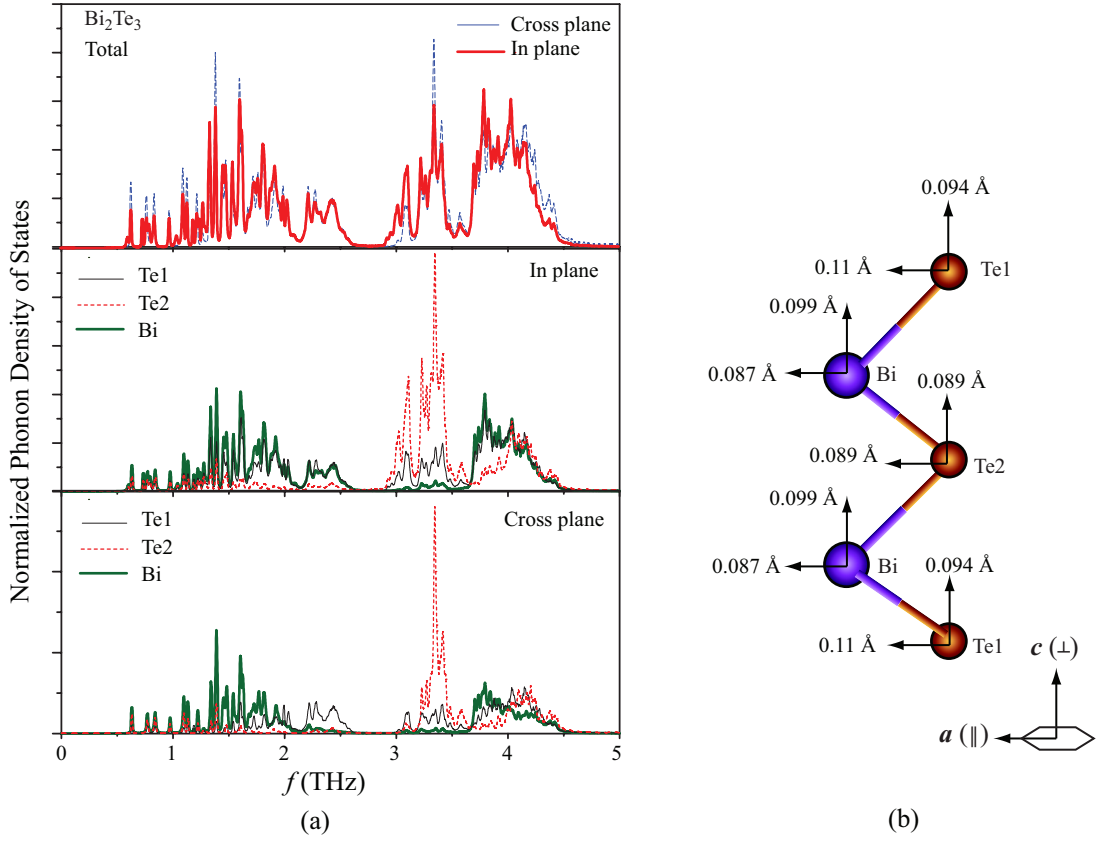
Figure 4.4: (a) Predicted variation of the directional phonon DOS for Bi_2Te_3 with respect to frequency. (b) Root mean square of the displacement for various atoms in Bi_2Te_3.

ence only lies in the high frequency regime ($f > 3$ THz), where the cross-plane spectrum seems to shift a little towards a relatively higher frequency regime. This rough identity indicates there is only minor difference between the in-plane and cross-plane vibration spectrum, which is consistent with the fact that C11 only differs slightly from C33. The in-plane and cross-plane PDOS of the different species provide more details about the lattice vibration. When $f < 1.5$ THz, where acoustic vibrations dominate, the three PDOS for both directions are almost the same. The Bi atoms have more modes in the low frequency regime ($f < 2.6$ THz) of the PDOS for both

the directions, but less modes in the high frequency regime ($f > 3$ THz) than those of the Te1 and Te2 atoms. This is due to their larger mass. Overall, the in-plane PDOS of Te1 and Bi match each other quite well and the difference only exists in a narrow frequency regime (2.8 THz $< f <$ 3.6 THz). This is believed to directly result from the strong Te1-Bi bonds. However, most in-plane vibration modes of Te2 atoms concentrate in the high frequency regime (2.8 THz $< f <$ 4.6 THz). The in-plane vibration spectrum of Te1 shows strong peaks between 2.8 THz and 3.6 THz, where Te1 and Bi have much less vibration modes. Te2 also has much less vibration modes than Bi and Te1 atoms in the regime between 1.5 THz and 2.6 THz. All these show that the correlation between the in-plane optical vibrations of Te2 and Bi/Te1 is weak, while the correlation between the in-plane vibrations of Bi and Te1 is strong. This may be due to the relatively weak Bi-Te2 bonds (compared with Bi-Te1 bonds) and the symmetric position of Te2 atoms in the five-layer sandwich structure. Similarly, the cross-plane PDOS of Te2 atoms mainly focuses in the high-frequency regime ($f > 2.8$ THz). There are strong peaks between 3 THz and 3.6 THz in the cross-plane PDOS of Te2, but those peaks are rather weak in the PDOS of Te1 and Bi, indicating the energy localization of those modes. Also, there are large differences among the cross-plane PDOS of neighboring Te1/Bi and Bi/Te2 layers, suggesting that phonon transporting across the planes will suffer from strong scattering. Those strong scatterings are mainly due to the mass difference and the large variation in $\Gamma\gamma'$ ($\Gamma\gamma'$ is the product of the force constant Γ and the bond-scaling parameter γ') in the neighboring bonds [99]. Figure 4.4(b) shows the root mean square displacement of atoms (RMS). The RMS of the Te2 atoms are isotropic, while the Bi atoms have

the largest cross-plane RMS and the Te1 atoms have the largest in-plane RMS.

4.2.3   MD Simulation Procedure and G-K Autocorrelation

The MD simulations were performed with a system consisting of $6 \times 6 \times 1$ hexognal unit cells and involving 540 atoms. The simulations with larger systems produced very similar results. The temperatures considered were from 100 K to 400 K, with an interval of 50 K. The time step was chosen as 10 fs. The Verlet leapfrog algorithm was adopted for the calculation, while the Nose-Hoover thermostat and the Berendsen barostat were used to control the system temperature and pressure. The system was first simulated in a NPT (constant number of atoms, pressure and temperature) ensemble for 100 ps-200 ps until it reached a free-standing state at the desired temperature, then it was switched into a NVE ensemble and ran for 200 ps to arrive in equilibrium. At each temperature point, 1700 ps raw heat current data were obtained for the calculation of HCACFs. After calculating HCACF, the direct integration method is used to obtain the thermal conductivity. The integral is averaged to smooth the behavior in a converged region. The final result is the average value over the converged region.

To speed up the calculations, the Wolf method[69] was adopted for the calculation of the long-range electrostatic interactions. The decay parameter β is chosen as 0.25 $\mathring{A}^{-1}$, and the cut-off radius R_c is chosen as 10 $\mathring{A}$.

4.2.4 Phonon Conductivities and Its Decomposition

Figure 4.5 shows the time variation of the normalized raw HCACF and the lattice thermal conductivity along the in-plane and cross-plane directions. The normalization factors $\langle \dot{\boldsymbol{w}}_\alpha(0) \cdot \dot{\boldsymbol{w}}_\alpha(0) \rangle$ for the two directions only differ slightly ($< 3\%$). The normalized raw HCACF curves in both directions involve high frequency components caused by the high frequency optical phonons. It is apparent that the fluctuations in the in-plane HCACF are much larger than the cross plane. Considering the identity of the normalized vibration spectrum along the two directions, the high frequency vibrations along the cross-plane direction are more likely to be localized. Both HCACF curves consist of two stages, i.e., an initial rapid decay stage followed by a relatively slow decay stage, which have also been found for other crystals [29]. It has been shown that the HCACF of a crystal with a multi-atom unit cell can be decomposed into three parts by fitting the HCACF to a function of the form [29]

$$
\begin{aligned}
\langle \dot{w}_\alpha(t) \cdot \dot{w}_\alpha(0) \rangle \quad = \quad & A_{\mathrm{A},sh,\alpha} \exp(-t/\tau_{p,\mathrm{A},sh,\alpha}) + A_{\mathrm{A},lg,\alpha} \exp(-t/\tau_{p,\mathrm{A},lg,\alpha}) + \\
& \sum_i B_{\mathrm{O},i,\alpha} \exp(-t/\tau_{p,\mathrm{O},i,\alpha}) \cos(\omega_{p,\mathrm{O},i,\alpha} t),
\end{aligned}
\tag{4.11}
$$

where $\tau_{p,i}$ is a time constant, the coefficients A and B represent the strength of a given mode, and the subscripts sh, lg, A, and O denote short-range, long-range, acoustic, and optical contributions, respectively. We used a Fourier low-pass filter (cut-off frequency was set as 1.5 THz) to remove the high frequency components of HCACF, and fitted the low frequency acoustic part using the two-term exponential functions. The fitting results are also shown in Figure 4.5. At the beginning, the decay relaxation times for HCACF curves are almost the same and rather short (0.27

102
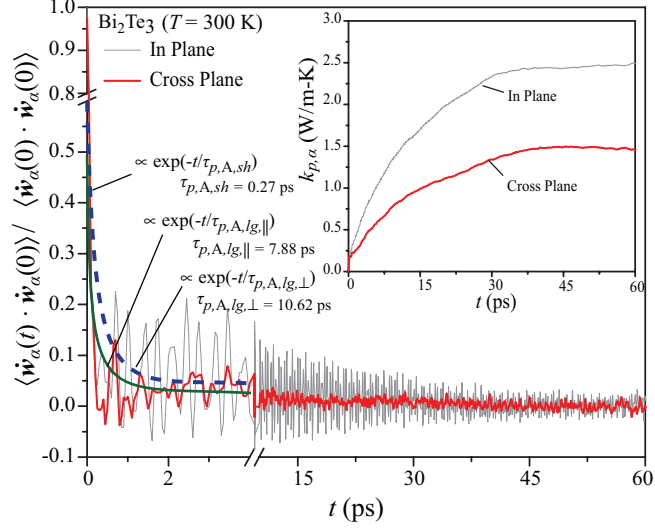
Figure 4.5: Time variation of the raw HCACF and the lattice thermal conductivity at $T = 300$ K, for the in-plane and cross-plane directions. The curve fits of the two-term exponential functions, for the HCACF low-frequency portion, are also shown.

ps). However, for the long-range decay, the relaxation time for the in-plane HCACF is 10.62 ps, which is longer than that for cross-plane HCACF (7.88 ps), indicating that the lattice scattering along the cross-plane direction is stronger. The time variation of the lattice thermal conductivities shown in Fig. 4.5, also confirms this.

Figure 4.6 shows the temperature-dependent, in-plane and cross-plane lattice conductivities of Bi_2Te_3 calculated by the MD simulations using the potentials listed in Table 5.3. The available experimental results [9] are also shown. Note that the calculated in-plane and cross-plane $k_{p,\parallel}$, $k_{p,\perp}$ are higher than the experimental results. This is expected, considering the various defects (e.g., isotopes, displacements, lamellae, etc.) in a real Bi_2Te_3 crystal[101], which will reduce the thermal conductivity.

The lattice conductivities in both directions roughly follow the $1/T$ law, similar to insulators. The calculated cross-plane thermal conductivity $k_{p,\perp}$ is lower than the
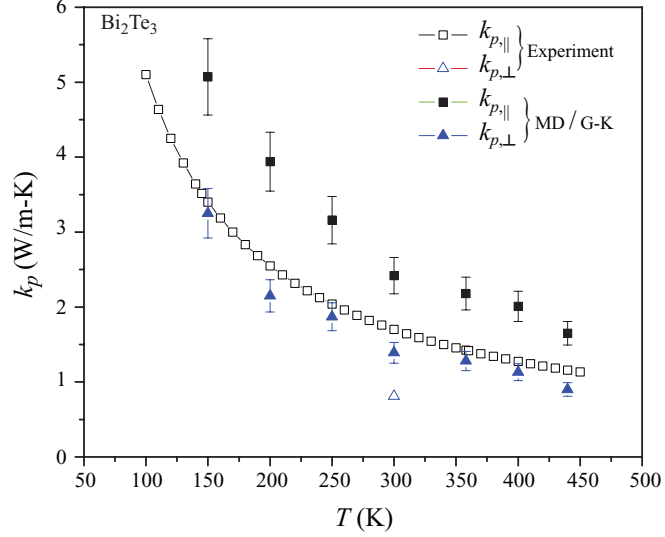
Figure 4.6: Predicted temperature-dependent, in-plane and cross-plane lattice thermal conductivity, compared with the experimental results [9].

in-plane $k_{p,\parallel}$. Since the average cross-plane sound velocity (1,631 m/s) is very close to the in-plane sound velocity (1,775 m/s), the difference between the two thermal conductivities is mainly due to the different anharmonicities along the two directions. This can be verified by the directional Grüneisen parameter $\gamma_{G,\alpha}$ along the direction α. For Bi_2Te_3, at 300 K, the in-plane Grüneisen parameter $\gamma_{G,\parallel}$ is 1.17, while the cross-plane Grüneisen parameter $\gamma_{G,\perp}$ is 1.86. The large difference in the anharmonicity originates from the unique bond characteristics in the layered structure (Fig. 4.1), in which the intra-layer bonds are mainly covalent but the inter-layer bonds are the hybrids of the electrostatic interaction and the van der Waals interaction.

Figure 4.5 illustrates the different decay stages and components of HCACF. According to Eqs. (3.8) and (4.11), the lattice thermal conductivity $\boldsymbol{K}_p$ can then be
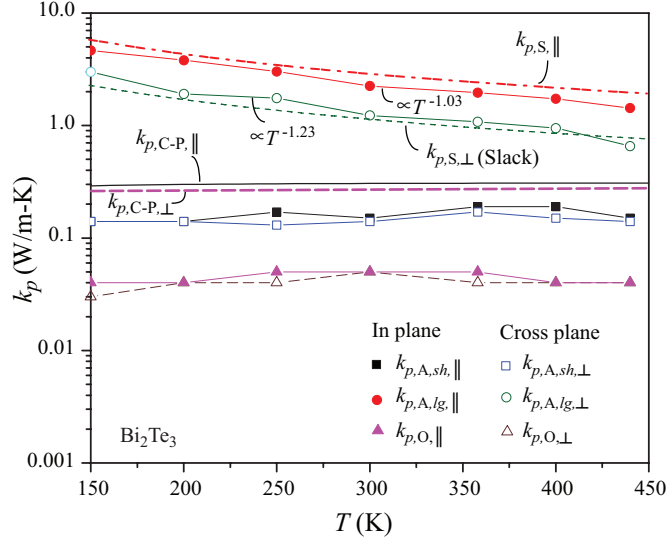
Figure 4.7: Decomposition of calculated in-plane and cross-plane thermal conductivity. The lowest in-plane and cross-plane thermal conductivities calculated by the Cahill-Pohl model are also shown.

decomposed into three parts as

$$\boldsymbol{K}_p \;\; = \;\; \boldsymbol{K}_{p,\mathrm{A},sh} + \boldsymbol{K}_{p,\mathrm{A},lg} + \boldsymbol{K}_{p,\mathrm{O}}. \tag{4.12}$$

Here $\boldsymbol{K}_{p,lg,\mathrm{A}}$ is believed to be the contribution from the long-range acoustic phonons, with a mean-free path larger than one half of their wavelengthes; $\boldsymbol{K}_{p,sh,\mathrm{A}}$ is the contribution from the short-range phonons, with their mean-free pathes minimized[29, 4] (Kaburaki et al.[102] attributed it to single-particle motions in a local environment); and $\boldsymbol{K}_{p,\mathrm{O}}$ is the contribution from the high frequency optical phonons. We obtained $\boldsymbol{K}_{p,sh,\mathrm{A}}$ and $\boldsymbol{K}_{p,lg,\mathrm{A}}$ by fitting the low frequency part of HCACF with the two-term exponential functions shown in Eq. (4.11), and obtained $\boldsymbol{K}_{p,\mathrm{O}}$ by directly integrating the high frequency part of HCACF. The Fourier low-pass and high-pass filters were used to separate the different components. Further details about the decomposition

105

can be found elsewhere [29, 4].

Figure 4.7 shows the variation of the different components of the in-plane and cross-plane lattice thermal conductivity with respect to temperature. The results shown are the average for several data sets. The difference between the summation of the fitted three components and that specified directly from the integral is less than 10%. As shown in Fig. 4.7, for both the in-plane and cross-plane directions, the long-range contribution $k_{p,A,lg}$ dominates, and $k_{p,A,sh}$ is relatively small, but still 3 to 4 times larger than $k_{p,O}$. The in-plane long-range contribution $k_{p,A,lg,\parallel}$ is larger than the cross-plane long-range component $k_{p,A,lg,\perp}$ and the ratio $k_{p,A,lg,\parallel}/k_{p,A,lg,\perp}$ varies from 1.55 to 2.17 in the temperature range 150 K $\sim$ 450 K. Considering the almost isotropic sound velocity and phonon DOS (Section 4.2.2), this difference is mainly attributed to the different scattering strength along the two directions. However, the short-range and optical components are almost the same in both the directions (the in-plane values seem slightly larger but the difference is in the error range of the data). This seems to indicate that the mean-free paths of both the short-range and optical phonons are independent of the scattering mechanisms and their transport is mainly determined by the local environment. This conclusion is consistent with the fact that $k_{p,A,sh}$ and $k_{p,O}$ are almost temperature independent. On the other hand, $k_{p,A,lg}$ decreases with increasing temperature. A power-law fit yields $k_{p,A,lg,\parallel} \propto T^{-1.03}$ and $k_{p,A,lg,\perp} \propto T^{-1.23}$, and the stronger temperature dependence of $k_{p,A,lg,\perp}$ may be due to larger thermal expansion along the cross-plane direction. In other words, in both the in-plane and cross-plane directions, $k_{p,A,lg}$ roughly follows the normal T^{-1} law for high-temperature lattice thermal conductivities.

In Fig. 4.7, the lattice conductivity calculated by the Cahill-Pohl model[54] $k_{p,\text{C-P}}$ is also shown, which is given by

$$k_{p,\text{C-P}} = \left(\frac{\pi}{6}\right)^{1/3} k_\text{B} n^{2/3} \sum_{i=1}^{3} u_{p,g,i} \left(\frac{T}{T_{\text{D},i}}\right)^2 \int_0^{T_{\text{D},i}/T} \frac{x^3 e^x}{(e^x - 1)^2} dx, \qquad (4.13)$$

where n is the number density of atoms. The lattice conductivity predicted by Eq. (4.13) has been interpreted as the minimum solid phase thermal conductivity. In Fig.4.7, $k_{p,\text{C-P},\parallel}$ is only slightly higher than $k_{p,\text{C-P},\perp}$ and both are almost temperature independent in the temperature range between 150 K and 450 K. The sum of $k_{p,\text{A},sh}$ and $k_{p,\text{O}}$ is about 60% of $k_{p,\text{C-P},\parallel}$ or $k_{p,\text{C-P},\perp}$. The behavior of $k_{p,\text{A},sh}$ and $k_{p,\text{O}}$ are actually quite similar. If they are both mainly affected by a local environment, the sum of them seems likely to be independent of different scattering mechanisms unless the local environment (with a dimension of the order of the interatomic spacing) is changed. In other words, this provides a lower limit of the phonon conductivity for structure engineering, which is 0.2 W/m-K at 300 K.

By assuming heat was mainly carried by the acoustic phonons scattered via the three-phonon processes, Slack [2] proposed a simple relation for the thermal conductivity of crystals with constant volume at high temperatures

$$k_{p,\text{S}} = \frac{3.1 \times 10^4 \langle M \rangle N_c^{1/3} \delta T_{\text{D},\infty}^3}{T \langle \gamma_\text{G}^2 \rangle}. \qquad (4.14)$$

Here $\langle M \rangle$ is the mean atomic weight of the atoms in the primitive cell, δ^3 is the average volume per atom, N_c is the number of atoms in a primitive cell, and $T_{\text{D},\infty}$ is defined from the phonon density of states (DOS) D_p,[2] i.e.,

$$T_{\text{D},\infty}^2 = \frac{5h_\text{P}^2}{3k_\text{B}^2} \frac{\int_0^\infty f^2 D_p(f) \mathrm{d}f}{\int_0^\infty D_p(f) \mathrm{d}f}, \qquad (4.15)$$

107

where h_P is the Planck constant, and f is the phonon frequency. Note that the integral is only over the acoustic portion of the phonon spectrum. $T_{\mathrm{D},\infty}$ is generally close or slightly lower than the Debye temperature for the acoustic branches $T_\mathrm{D}/N_c^{1/3}$ (T_D is the Debye temperature).

Slack mainly applied this relation for isotropic crystals with a cubic structure. However, as discussed in the reference [99], if the long-range phonons dominate the heat transfer, their contribution may still have a form very similar to Eq. (4.14), therefore, it is possible to modify this relation and apply it for anisotropic crystals. Assuming that the scattering of phonons along the α direction is only related to the elastic and anharmonic properties along this direction, that is, the transport of phonons along this direction is similar to the transport in an isotropic structure with the same elastic and anharmonic properties, then we extended Eq. (4.14) as

$$k_{p,\mathrm{S},\alpha} = \frac{3.1 \times 10^4 \langle M \rangle N_c^{1/3} \delta T_{\mathrm{D},\infty,\alpha}^3}{T \gamma_{\mathrm{G},\alpha}^2}, \ \ \alpha = \perp \ \text{or} \ \parallel . \qquad (4.16)$$

Here $T_{\mathrm{D},\infty,\alpha}$ is given by Eq. (4.15) while replacing $D_p(\nu)$ with $D_{p,\alpha}(\nu)$. As discussed in Section 4.2.2, the total in-plane and cross-plane PDOS are almost the same, and the calculation according to Eq. (4.15) provides $T_{\mathrm{D},\infty,\parallel} = 76$ K and $T_{\mathrm{D},\infty,\perp} = 75$ K. Using $\gamma_{\mathrm{G},\parallel} = 1.17$ and $\gamma_{\mathrm{G},\perp} = 1.86$ calculated in Section 5.4, the in-plane and cross-plane long-range components [denoted as $k_{p,\mathrm{A},lg,\parallel}$(Slack) and $k_{p,\mathrm{A},lg,\perp}$(Slack)] were calculated by Eq. (4.16) and are also shown in Fig. 4.7. Overall, these results are in reasonable agreement with those decomposed from the MD simulations in both directions (the average deviations from the MD results are within 30% for $k_{p,\mathrm{A},lg,\parallel}$, and 20% for $k_{p,\mathrm{A},lg,\perp}$).

4.2.5 Role of Phonon-Electron Scattering in Phonon Conductivity

In semiconductors, phonons are scattered by grain boundary, defects, other phonons, and carriers. According to the Matthiessen rule, the total thermal resisitivity can be represented as

$$\frac{1}{k_p} = \frac{1}{k_{p,b}} + \frac{1}{k_{p,d}} + \frac{1}{k_{p,\mathrm{U}}} + \frac{1}{k_{p,c}}, \tag{4.17}$$

where $k_{p,b}$, $k_{p,d}$, $k_{p,\mathrm{U}}$ and $k_{p,c}$ are the thermal conductivity limited by the scattering of grain boundary, defects, phonon-phonon U process and carriers, respectively.

The thermal conductivity limited by phonon-carrier scattering $k_{p,c}$ can be estimated using the electrical resistivity ρ_e. Their relations have been derived by ignoring the difference between the N-processes and U-processes between carriers and phonons [39, 103], as is

$$\frac{1}{k_{p,c}} = \frac{A}{N_{\mathrm{L}}T}\left(\frac{T_{\mathrm{D}}}{T}\right)I_5\frac{\pi^2 z_e^2}{27 I_4^2} \tag{4.18}$$

$$\rho_e = A\left(\frac{T}{T_{\mathrm{D}}}\right)^5 I_5, \tag{4.19}$$

where

$$I_n = \int_0^{T_{\mathrm{D}}/T} \frac{x^n e^x}{(e^x - 1)^2}\mathrm{d}x. \tag{4.20}$$

In the above relations, z_e is the number of free electrons per atom, N_{L} the Lorenz constant, and A is a constant (for metals, $A = 3.7$). Then we have

$$\frac{1}{k_{p,c}} = \frac{\rho_e}{N_{\mathrm{L}}T}\frac{(T_{\mathrm{D}}/T)^6}{27 I_4^2}\pi^2 z_e^2. \tag{4.21}$$

When T/T_{D} increases from 0.1 to 10, $(T_{\mathrm{D}}/T)^6/I_4(T_{\mathrm{D}}/T)^2$ decreases from 97 to 9. Also, for normal dopant concentration ($< 10^{19}$ cm^{-3}), z_e is of the order of 10^{-3}. Then

for a wide temperature range ($0.1 \leq T/T_{\mathrm{D}} \leq 10$), $1/k_{p,c}$ is only about 10^{-4} of the electrical thermal resistivity $1/k_e$ found from the Wiedemann-Franz law; therefore, it is negligible for most semiconductors (including Bi_2Te_3).

4.3   Prediction of Electronic Properties

The thermoelectric transport properties can be derived from BTE with the relaxation time approximation. The general form of the relations for TE properties is [104]

$$
\begin{aligned}
\sigma_{e,\alpha\beta}(E_e) &= \frac{1}{N}\sum_{i,\boldsymbol{\kappa}} e_c^2 \tau_{e,i,\boldsymbol{\kappa}} u_\alpha(i,\boldsymbol{\kappa}) u_\beta(i,\boldsymbol{\kappa}) \frac{\delta(E_e - E_{e,i,\boldsymbol{\kappa}})}{\mathrm{d}E_e} \\
\sigma_{e,\alpha\beta} &= \frac{1}{V}\int \sigma_{e,\alpha\beta}(E_e)[-\frac{\partial f_\mu(T;E_e)}{\partial E_e}]\mathrm{d}E_e \\
v_{\alpha\beta} &= \frac{1}{e_c TV}\int \sigma_{e,\alpha\beta}(E_e)(E_e - \mu)[-\frac{\partial f_\mu(T;E_e)}{\partial E_e}]\mathrm{d}E_e \\
\alpha_{\mathrm{S},\alpha\beta} &= (\sigma_e^{-1})_{j\alpha} v_{e,j\beta} \\
k_{\alpha\beta}^\circ &= \frac{1}{e_c^2 TV}\int \sigma_{e,\alpha\beta}(E_e)(E_e - \mu)^2[-\frac{\partial f_\mu(T;E_e)}{\partial E_e}]\mathrm{d}E_e \\
k_{e,\alpha\beta} &= k_{\alpha\beta}^\circ - T v_{\alpha j}(\sigma_e^{-1})_{lj} v_{l\beta},
\end{aligned}
\tag{4.22}
$$

where α_{S} is the Seebeck coefficient, σ_e is the electrical conductivity, k_e is the electrical thermal conductivity, i is the band index, τ_e is the relaxation time, e_c is the charge of electron, $\boldsymbol{\kappa}$ is the wave vector, u is the group velocity, $f = [e^{(E_e - \mu)/(k_{\mathrm{B}}T)} + 1]^{-1}$ is the equilibrium Fermi-Dirac distribution function, μ is the chemical potential, and E_e is the total energy of electron. Accordingly, the band structure $E_e(i,\boldsymbol{\kappa})$, chemical potential μ, and relaxation times τ_e, are required inputs for the electronic property calculations.

4.3.1 Electronic Band Structure of Bi$_2$Te$_3$

The band structure calculation for Bi$_2$Te$_3$ was carried out in the framework of density functional theory (DFT). The WIEN2k program [105], which employs the full potential, linearized augmented plane-wave (LAPW) and local orbits (LO) methods, was chosen for this investigation. The generalized gradient approximation (GGA) as proposed by Perdew et al. [106] was used for the exchange and correlation potential. The experimental rhombohedral cell parameters of $a = 10.48$ Å and 24.16° and the atomic parameters[5, 89] $u = 0.4001$ and $v = 0.2095$ at $T = 300$ K were used in the calculations. The radii of both Bi and Te atoms were set as 2.8 a.u. An $\boldsymbol{R} \cdot \boldsymbol{\kappa}_{max}$ value of 9 and a G_{max} value of 14 were adopted, and a non-shifted mesh with 10,000 $\boldsymbol{\kappa}$ points were used. The energy cut-off between the core and valence states was set at -6 Ry. Because of the significant spin–orbit (SO) effects on the band structure of Bi$_2$Te$_3$, the eigen states below 10 Ry were considered in the SO calculations. As suggested by Larson [19], the $p_{1/2}$ corrections may significantly affect the band structure; therefore, the $p_{1/2}$ corrections have also been considered for the Bi $6p$ and Te $5p$ states.

The calculated band structures along some high-symmetry lines is plotted in Fig. 4.8. The solid and dash lines show the results with and without the $p_{1/2}$ corrections, respectively. When the $p_{1/2}$ corrections are not included, our results are consistent with the results of Scheidemantel et al. [20] The band gap is evaluated as $\Delta E_{e,g} = 0.13$ eV (Scheidemantel et al.[20] reported $\Delta E_{e,g} = 0.11$ eV), which is slightly smaller than the zero-temperature experimental results[90] (0.16 eV). The band edges were found in the mirror plane and off the high symmetry lines, yielding six highest valence bands
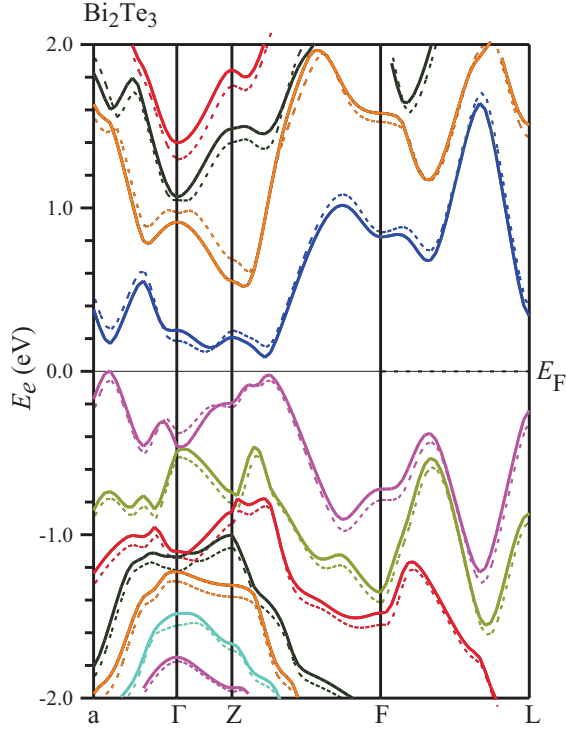
Figure 4.8: Electronic band structure of Bi_2Te_3 along the high-symmetry lines with spin–orbit coupling. The solid and dash lines are for the results with and without the $p_{1/2}$ corrections included.

(HVB) and six lowest conduction bands (LCB). The conduction band edge (CBE) is found at (0.667,0.571,0.571), close to those of previous investigations [20, 18, 21]. The secondary LCB edge is found at (0.238,0.238,0.238) with an 10 meV higher energy. The valence band edge (VBE) is also found at (0.667,0.571,0.571), the same κ position of the LCB edge. This result is close to (0.652,0.579,0.579) reported by Scheidemantel et al.[20], but different from (0.546,0.383,0.383) found by Youn et al.[18], and (0.555,0.397,0.397) by Kim et al.[21]. These comparisons are listed in Table 4.4.

As shown in Fig. 4.8, the addition of $p_{1/2}$ lowers the CBE, but elevates the VBE,

resulting a decrease in $\Delta E_{e,g}$ from 0.13 eV to 0.07 eV. The positions of the band edges are still off the high symmetry lines. The CBE keeps at the same position (0.667,0.571,0.571), but VBE shifts to (0.571,0.571, 0.429). Fig. 4.8 also illustrates this shift.

The effective masses of electrons and holes for a single valley near the band edge $m_{i,e,\circ}^* = (m_{i,e,\circ,xx}^* m_{i,e,\circ,yy}^* m_{i,e,\circ,zz}^*)^{1/3}$ $(i = e, h)$, where $m_{i,e,\circ,kl}^{*}{}^{-1} = \hbar^{-2}[\partial^2 E_e/\partial\kappa_k\partial\kappa_l]$, were calculated by choosing a small region around the band extrema. As shown in Table 4.4, the addition of the $p_{1/2}$ corrections significantly reduces $m_{e,e,\circ}^*$ and $m_{h,e,\circ}^*$. Figure 4.9 (a) also shows the addition of the $p_{1/2}$ corrections lower the slope of the electron density of states near the band edge. The band structure without the $p_{1/2}$ corrections seems to agree better with the experiments [93, 94, 90].

Table 4.4: Comparison of the calculated CBE, VBE, and the corresponding effective masses $m_{i,e,\circ}^* = (m_{i,e,\circ,xx}^* m_{i,e,\circ,yy}^* m_{i,e,\circ,zz}^*)^{1/3}$ at the band edges, with the available results[18, 19, 20, 21].

Reference	$\Delta E_{e,g}$ (eV)	CBE	VBE	$m_{e,e,\circ}^*$	$m_{h,e,\circ}^*$
Youn et al. [18]	0.06	(0.663,0.568, 0.568)	(0.546,0.383, 0.383)	-	-
Larson [19]	0.05	(0.381,0.5, 0.5)	(0.546,0.383, 0.383)	-	-
Scheidemantel et al. [20]	0.11	(0.663,0.568, 0.568)	(0.652,0.579, 0.579)	-	-
Kim et al. [21]	0.154	(0.646,0.549, 0.549)	(0.555,0.397, 0.397)	0.07	0.11
Experiment [93, 94, 90]	0.16	-	-	0.07	0.09
This study (no $p_{1/2}$ correction)	0.13	(0.667,0.571, 0.571)	(0.667,0.571, 0.571)	0.06	0.08
This study ($p_{1/2}$ correction)	0.07	(0.667,0.571, 0.571)	(0.571,0.571, 0.429)	0.02	0.03

The total electron density of states D_e with and without the $p_{1/2}$ corrections, are shown in Figs. 4.9(a). It is apparent that D_e of both the valence bands and conduction bands are non-parabolic. However, we find the Kane band structure model[107], with $\Delta E_{e,g}$ and $m^*_{i,e,\circ}$ calculated from the Wien2K (listed in Table 4.4), gives a good approximation for D_e near both the conduction and valence band edges.

Many semiconductors with narrow band gap exhibit significant non-parabolicity of their energy bands. The two-band Kane model[107], which has been used successfully to describe many real narrow gap materials[92], was adopted to account the non-parabolicity for theoretical calculations of transport coefficients. The Kane model assumes the band extrema for the conduction and valence bands are located at the same κ point. The energy separation from other bands is greater than the main energy gap and the momentum operator has non-zero matrix elements between the states corresponding to the extremal points [108]. The dispersion relation of the bands of a valley is of the form

$$E_e(1 + \frac{E_e}{\Delta E_{e,g}}) = \frac{\hbar^2 \kappa^2}{2m_{i,e,\circ}}, \tag{4.23}$$

where $m_{i,e,\circ}$ is the density of states effective mass at the band edge, $\Delta E_{e,g}$ is the energy gap, and κ is the wave vector. Note here E_e is measured from the band edge. Then the density of states D_e can be explicitly written as

$$D_e(E) = \frac{2^{1/2} N m_{e,e,\circ}^{3/2}}{\pi^2 \hbar^3} E_e^{1/2} (1 + \frac{E_e}{\Delta E_{e,g}})^{1/2} (1 + 2\frac{E_e}{\Delta E_{e,g}}). \tag{4.24}$$

Here N is the multiplicity of the valleys. However, for Bi_2Te_3, it is the D_e calculated by the Kane model using $N = 12$ instead of $N = 6$ that can match the results near the band edge from Wien2K [shown in Fig. 4.9 (a)]. This is believed to result from the

secondary band edges, of which the energy only slightly differs from that of the band edges. This also leads to the total effective mass $m_{e,e} = N^{2/3}m_{e,e,\circ} = 0.31m_e$ and $m_{h,e} = 0.42m_e$ (m_e is the mass of a free electron), which agree well with $m_{e,e} = 0.32m_e$ and $m_{h,e} = 0.46m_e$ measured by Harman et al. [109] Also note that the energy regime in which the Kane model can provide a good approximation for D_e is within 0.1 eV around the band edges. Since only the states with an energy within $3k_BT$ about the chemical potential are important for the transport properties, the Kane model is believed to be a good approximation for D_e over a wide temperature range.

The total density of states without the $p_{1/2}$ corrections for each species (a product of the partial D_e of each species and its multiplicity), are shown in Figs. 4.9(b). For comparison of the contribution of different orbitals, the orbital-decomposed D_e (without the $p_{1/2}$ corrections) are also shown in Fig. 4.9(c).

As shown in Fig. 4.9(b), for the valence bands, Te1 atoms contribute the most to the electronic density of states D_e near the band edge, while the contributions from Bi and Te2 atoms are less and nearly the same. This indicates that the Te1 atoms are more probable to lose electrons and be donors in the structure. In contrast, for the conduction bands, the Bi atoms contribute the most to the density of states near the band edge, indicating they are more probable to receive an electron and be acceptors. Note that the contributions from Te1 atoms are only slightly less than those from the Bi atoms. This is consistent with the slightly ionic-like bond between the Bi atoms and Te1 atoms. Te2 atoms contribute the least to the density of states at both the valence and conduction band edges, indicating they are relatively inert in determining the electronic transport properties of Bi_2Te_3. Figure 4.9(c) shows that, for Te1 and Te2
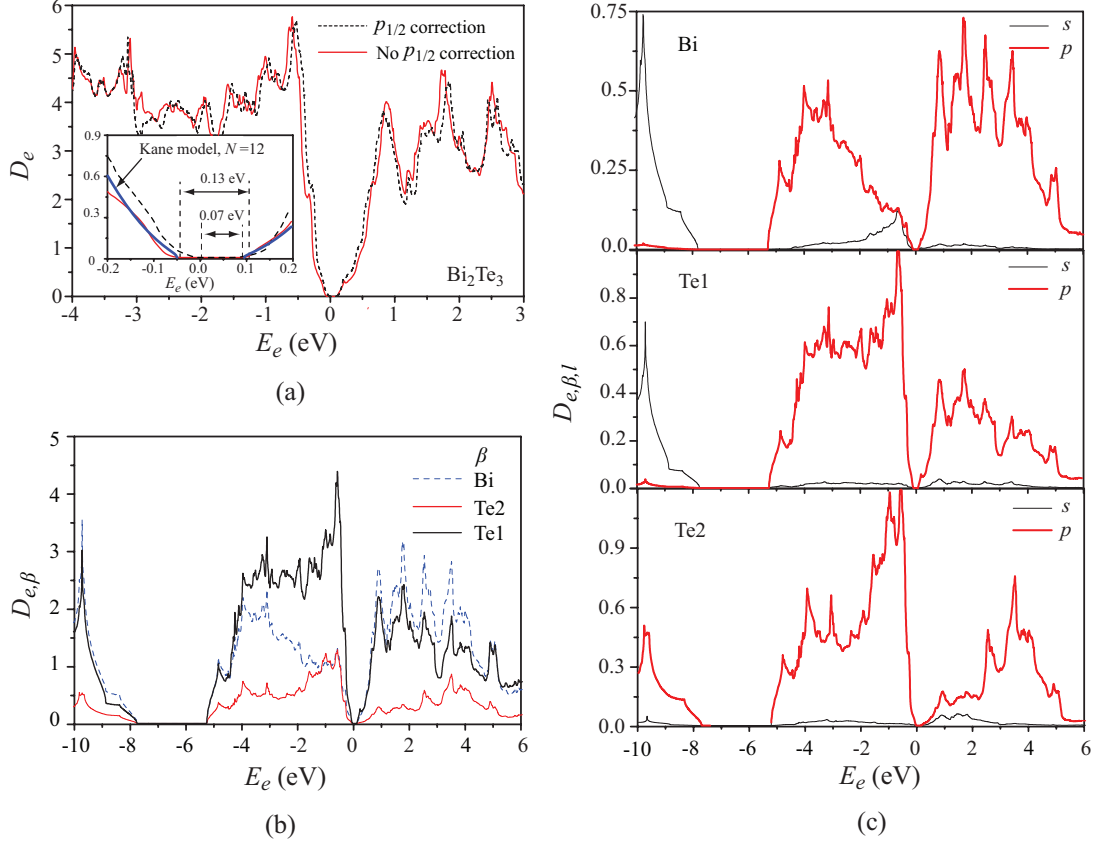
Figure 4.9: (a) Dimensionless electronic density of states D_e of Bi_2Te_3 with and without the $p_{1/2}$ corrections. The inset is for the band edge, also shown is the D_e calculated by the Kane model. (b) Total $D_{e,\beta}$ for individual species β (partial D_e of each species times its multiplicity). (c) Decomposed, partial $D_{e,\beta,l}$ for each species.

atoms, p-type orbitals predominate in both the valence band and conduction band. Bi atoms, however, have strong $s+p$ orbital contribution at the valence band edge, but the wave function at the conduction band edge is mainly p-type. Considering the layer sequence Te1-Bi-Te2-Bi-Te1, it seems the bonds between the nearest-neighboring atoms in each quintuple layer are primarily the $pp\sigma$ interactions, as suggested by Mishra et al. [110]

4.3.2 Chemical Potential

In a thermal equilibrium system, chemical potential μ is an essential parameter to describe the equilibrium distribution of carriers and their concentrations. All the electronic transport coefficients, in fact, are functions of the band structure $E_e(\boldsymbol{\kappa})$, μ, and temperature.

Generally, μ can be determined from

$$n_{d,h} - n_{d,e} \;=\; n_h + n_{h,b} - n_e - n_{e,b}, \tag{4.25}$$

where $n_{d,h}$ and $n_{d,e}$ are the concentrations of acceptors and donors, n_h is the hole concentration, $n_{h,b}$ is the concentration of holes bound on the acceptors, n_e is the electron concentration, $n_{e,b}$ is the concentration of electrons bound on the donors. For modest doped semiconductors, $n_{h,b}$ and $n_{e,b}$ are normally negligible at normal and high temperatures (> 100 K). Therefore, we can rewrite Eq. (4.25) as

$$n_{d,h} - n_{d,e} = \int_{-\infty}^{0} D_e(E_e)\frac{1}{e^{(\mu - E_e)/k_B T} + 1}\mathrm{d}E_e - \int_{\Delta E_{e,g}}^{\infty} D_e(E_e)\frac{1}{e^{(E_e - \mu)/k_B T} + 1}\mathrm{d}E_e,$$
$$\tag{4.26}$$

Given $n_{d,h} - n_{d,e}$, and using the D_e calculated by the Kane model, we obtain the carrier concentrations and the chemical potentials at each temperature point. Figure 4.10 shows the temperature dependence of the calculated carrier concentrations and chemical potentials, compared with the experimental results[10] for p-type Bi_2Te_3 single crystals, where $n_{d,h} - n_{d,e} = 1.1 \times 10^{19}$ cm^{-3}. Both a constant $\Delta E_{e,g}$ and a temperature dependent $\Delta E_{e,g}(T)$ were adopted in the calculation. As shown in Fig. 4.10, a constant $\Delta E_{e,g}$ gives a much lower carrier concentration compared to the experiments [10] at high temperatures ($T > 300$ K), when the thermal excitation of
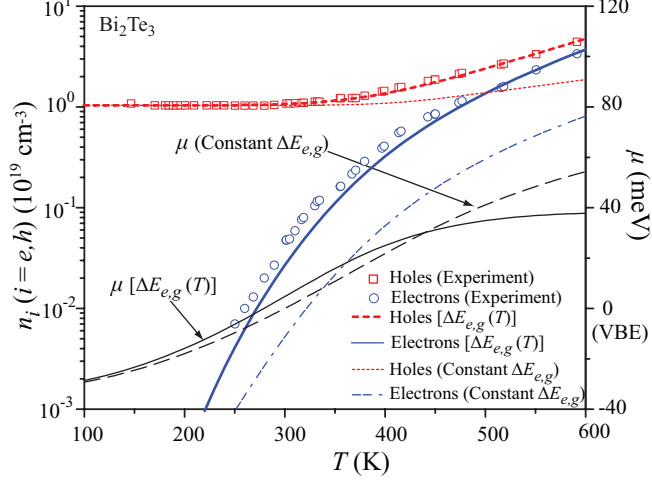
Figure 4.10: Temperature dependence of the calculated carrier concentrations and chemical potentials, compared with the experimental results [10]. Both a constant band gap $\Delta E_{e,g} = 0.13$ eV and a temperature-dependent band gap $\Delta E_{e,g} = 0.13 - 1.08 \times 10^{-4}T$ were used.

carriers becomes important. A good overall agreement can only be achieved by using a temperature-dependent band gap $\Delta E_{e,g} = 0.13 - 1.08 \times 10^{-4}T$. The different $\Delta E_{e,g}$ produce two chemical potential μ curves. The deviation between them is small below 200 K, but becomes more prominent when $T \geq 250$ K, especially when $T \geq 500$ K. Below 300 K, μ resides within the valence band and the sample is in the extrinsic regime. For $T > 300$ K, increasingly more carriers are thermally excited, leading μ into the band gap, and the crystal becomes intrinsic. At even higher temperatures, μ tends to move toward the middle of the band gap. In the following electrical transport calculations, we use μ calculated from Eq. (4.26) with the temperature-dependent $\Delta E_{e,g}$ by shifting the conduction band.

4.3.3 Relaxation Time Models

The relaxation time models simplify the calculation of BTE, but condense all the complexities into the relaxation time τ_e. In principle, the scattering relaxation time can be obtained using the Fermi golden rule and the perturbation theory. The scattering of electrons is related to the perturbation of the Hamiltonian for an electron, which is [105, 111]

$$
\begin{aligned}
\mathrm{H} &= -\frac{\hbar^2}{2m_e}\nabla^2 + \frac{e_c^2}{4\pi\epsilon_\circ}\int\frac{n_e g_e(\boldsymbol{r}')}{|\boldsymbol{r}-\boldsymbol{r}'|}\mathrm{d}\boldsymbol{r}' + \varphi_{ec} + \varphi_{ext} + \mathrm{H}' \qquad (4.27)\\[2mm]
\mathrm{H}' &= \mathrm{H}'_{e-p,\mathrm{A}} + \mathrm{H}'_{e-p,\mathrm{O}} + \mathrm{H}'_{e-p,\mathrm{PO}} + \mathrm{H}'_{e-v,d} + \mathrm{H}'_{e-v,\mathrm{C}} + ...\\[2mm]
&= \varphi_{d,a}\frac{\partial\boldsymbol{d}}{\partial\boldsymbol{r}} + \varphi_{d,o}\boldsymbol{d} - \frac{e_c q_e}{V_\circ}\sum_{\boldsymbol{\kappa}_p}\frac{\kappa_p}{\kappa_p^2+\lambda^{-2}}(iQ_{\boldsymbol{\kappa}_p}e^{i\boldsymbol{\kappa}_p\cdot\boldsymbol{r}}) +\\[2mm]
&\quad\, \varphi_{v,c} + \frac{Ze_c^2}{4\pi\epsilon r}e^{-r/\lambda} + ... \qquad (4.28)
\end{aligned}
$$

where $g_e(\boldsymbol{r})$ is the electron radial distribution function, φ_{ec} is the exchange-autocorrelation energy, φ_{ext} is the external potential excluding the perturbation, H' is the perturbation Hamiltonian due to scatterings, $\mathrm{H}'_{e-p,\mathrm{A}}$, $\mathrm{H}'_{e-p,\mathrm{O}}$, $\mathrm{H}'_{e-p,\mathrm{PO}}$, $\mathrm{H}'_{e-v,d}$, and $\mathrm{H}'_{e-v,\mathrm{C}}$ are the perturbation Hamiltonian for the acoustic phonon scattering, non-polar optical phonon scattering, polar optical phonon scattering, short-range scattering by impurity, and scattering by Coulomb potential, respectively. Here $\varphi_{d,a}$ and $\varphi_{d,o}$ are the deformation potentials for the acoustic and optical phonons, q_e is the effective charge, $\varphi_{v,c}$ is the scattering potential of impurity. $\boldsymbol{d} = N^{-1/2}\sum_{\boldsymbol{\kappa}_p}Q_{\boldsymbol{\kappa}_p}\boldsymbol{s}_{\boldsymbol{\kappa}_p}\exp(i\boldsymbol{\kappa}_p\cdot\boldsymbol{R})$ (N is the number of unit cells and $\boldsymbol{s}_{\boldsymbol{\kappa}_p}$ is the polarization vector) is the normal coordinate form of lattice displacement, $\boldsymbol{\kappa}_p$ is the phonon wave vector, $Q_{\boldsymbol{\kappa}_p}$ is the normal coordinate, λ is the screening length, and Ze_c is the effective charge of impurity.

The electron relaxation time τ_e for a mode $\boldsymbol{\kappa}$ can be represented as [111]

$$\frac{1}{\tau_e(\boldsymbol{\kappa})} = \sum_i \frac{1}{\tau_{e,i}(\boldsymbol{\kappa})} = \int \frac{\mathrm{d}\boldsymbol{\kappa'}}{(2\pi)^3} \dot{\gamma}_{\boldsymbol{\kappa},\boldsymbol{\kappa'},i}(1 - \frac{g_{\boldsymbol{\kappa'}}}{g_{\boldsymbol{\kappa}}}\frac{f_{\boldsymbol{\kappa}}^{\circ}}{f_{\boldsymbol{\kappa'}}^{\circ}}), \qquad (4.29)$$

where $f_{\boldsymbol{\kappa}}^{\circ}$ is the carrier equilibrium distribution , $g_{\boldsymbol{\kappa}} = f_{\boldsymbol{\kappa}} - f_{\boldsymbol{\kappa}}^{\circ}$ is the perturbation of the distribution, $\dot{\gamma}_{\boldsymbol{\kappa},\boldsymbol{\kappa'},i}$ is the transition rate from state $\boldsymbol{\kappa}$ to $\boldsymbol{\kappa'}$ by the ith scattering, which can in turn be given by the Fermi golden rule as [111]

$$\dot{\gamma}_{\boldsymbol{\kappa},\boldsymbol{\kappa'},i} = \frac{2\pi}{\hbar}\delta[E_e - E_e(\boldsymbol{\kappa'})]|M_{\boldsymbol{\kappa},\boldsymbol{\kappa'},i}|^2$$

$$M_{\boldsymbol{\kappa},\boldsymbol{\kappa'},i} = \langle\boldsymbol{\kappa'}|\mathrm{H}_i'|\boldsymbol{\kappa}\rangle = \int \psi^{\dagger}(\boldsymbol{\kappa'},\boldsymbol{r})\mathrm{H}_i'\psi(\boldsymbol{\kappa},\boldsymbol{r})\mathrm{d}\boldsymbol{r}, \qquad (4.30)$$

where H_i' is the perturbation Hamiltonian for the scattering mechanism i, and $\psi(\boldsymbol{\kappa},\boldsymbol{r})$ is the wave function for mode $\boldsymbol{\kappa}$. The Bloch wave function corresponding to the electron wave vector $\boldsymbol{\kappa}$ can be written as

$$\psi(\boldsymbol{\kappa'},\boldsymbol{r}) = \frac{1}{V^{1/2}}\sum_o C_J' \sum_{\boldsymbol{G}} C_{\boldsymbol{G}}^{\boldsymbol{\kappa}} e^{i(\boldsymbol{\kappa}+\boldsymbol{G})\cdot\boldsymbol{r}}, \qquad (4.31)$$

where V is the volume, C and C' are coefficients, and the subscripts J and $\boldsymbol{G}$ denote the different orbitals and reciprocal lattice vectors. Therefore,

$$M_{\boldsymbol{\kappa},\boldsymbol{\kappa'}} = \frac{1}{V^{1/2}}\sum_{J'}\sum_{J} C_{J'}^{'\dagger}C_J' \sum_{G'}\sum_{G} e^{i(-\boldsymbol{\kappa'}-\boldsymbol{G'})\cdot\boldsymbol{r}}\mathrm{H}' e^{i(\boldsymbol{\kappa}+\boldsymbol{G})\cdot\boldsymbol{r}}. \qquad (4.32)$$

If the wave function and the perturbation potential can be obtained from the first-principle calculation, $\tau_{e,i}$ can be directly determined. This calculation is very challenging and here we just introduce an analytical relaxation time model, which is also based on the Fermi golden rule and incorporates the non-parabolic Kane model for the energy dispersion.

Five common electron scattering mechanisms are considered in this work, namely due to deformation potential of the acoustic phonons $\tau_{e-p,A}$, deformation potential of the optical phonons $\tau_{e-p,O}$, polar scattering by the optical phonons $\tau_{e-p,PO}$, short range deformation potential of vacancies $\tau_{e-v,d}$, Coulomb potential of vacancies $\tau_{e-v,C}$. According to the Matthiessen rule, the total scattering relaxation time τ_e is expressed as

$$\frac{1}{\tau_e} = \frac{1}{\tau_{e-p,A}} + \frac{1}{\tau_{e-p,O}} + \frac{1}{\tau_{e-p,PO}} + \frac{1}{\tau_{e-v,d}} + \frac{1}{\tau_{e-v,C}}. \tag{4.33}$$

Using the Kane model, the expressions for different scattering mechanisms are given as follows.[91]

(i) *Scattering by Deformation Potential of Acoustic Phonons $\tau_{e-p,A}$*

The relaxation time for electrons dispersed on the deformational potential of acoustic phonons, when using the Kane model of dispersion and assuming a elastic procedure, can be given as

$$
\begin{aligned}
\tau_{e-p,A} &= \frac{(\tau_{e-p,A})_\circ \left(E_e + \frac{E_e^2}{\Delta E_{e,g}}\right)^{-1/2}}{\left(1 + 2\frac{E_e}{\Delta E_{e,g}}\right)\left[(1-A)^2 - B\right]} \\
A &\equiv \frac{\frac{E_e}{\Delta E_{e,g}}(1 - a_A)}{\left(1 + 2\frac{E_e}{\Delta E_{e,g}}\right)}, \quad a_A = \frac{\varphi_{d,A,v}}{\varphi_{d,A,c}} \\
B &\equiv \frac{8\frac{E_e}{\Delta E_{e,g}}\left(1 + \frac{E_e}{\Delta E_{e,g}}\right)a_A}{3\left(1 + 2\frac{E_e}{\Delta E_{e,g}}\right)^2} \\
(\tau_{e-p,A})_\circ &\equiv \frac{2\pi\hbar^4 C_l}{\varphi_{d,a,c}^2 k_B T (2m_{e,e,o})^{3/2}},
\end{aligned} \tag{4.34}
$$

where $\varphi_{d,A,c}$ is the acoustic deformation potential coupling constant for the conduction band, C_l is a combination of elastic constants, a_A is the ratio of the acoustic deformation potential coupling constants for the valence and conduction bands, and

$m_{e,e,\mathrm{o}}$ is the density of states effective mass for a single ellipsoid.

(ii) *Scattering by Deformation Potential of Optical Phonons* $\tau_{e-p,\mathrm{O}}$

$$
\begin{aligned}
\tau_{e-p,\mathrm{O}} &= \frac{(\tau_{e-p,\mathrm{O}})_{\circ}(E_e + \frac{E_e^2}{\Delta E_{e,g}})^{-1/2}}{(1 + 2\frac{E_e}{\Delta E_{e,g}})[(1-A)^2 - B]} \\[2mm]
A &\equiv \frac{\frac{E_e}{\Delta E_{e,g}}(1 - a_\mathrm{O})}{(1 + 2\frac{E_e}{\Delta E_{e,g}})}, \quad a_\mathrm{O} = \frac{\varphi'_{d,\mathrm{O},v}}{\varphi'_{d,\mathrm{O},c}} \\[2mm]
B &\equiv \frac{8\frac{E_e}{\Delta E_{e,g}}(1 + E_e/\Delta E_{e,g})a_\mathrm{O}}{3(1 + 2\frac{E_e}{\Delta E_{e,g}})^2} \\[2mm]
(\tau_{e-p,\mathrm{O}})_{\circ} &\equiv \frac{2\hbar^2 a^2 \rho (\hbar\omega_{p,\mathrm{O}})^2}{\pi \varphi'^2_{d,o,c} k_\mathrm{B} T (2m_{e,e,\mathrm{o})^{3/2}}},
\end{aligned}
\tag{4.35}
$$

where a is lattice constant, ρ is the density, $\omega_{p,\mathrm{O}}$ is the frequency of the optical phonons, a_o is the ratio of the optical deformation potential coupling constants for valence and conduction bands.

(iii) *Scattering by Polar-Optical Phonons* $\tau_{e-p,\mathrm{PO}}$

In a simple isotropic parabolic model, the relaxation time for polar longitudinal optical phonons has the form

$$
\tau_{e-p,\mathrm{PO}}^{-1} \sim \frac{1}{u_e \kappa^2} \int_0^{2\kappa} q \mathrm{d}q,
\tag{4.36}
$$

where u_e is the velocity of electrons. When the integral takes into account all phonons, we have

$$
\tau_{e-p,\mathrm{PO}} = \frac{\hbar^2 u_e}{2k_\mathrm{B} T e_c^2 [(\epsilon_\mathrm{o}\epsilon_{e,s})^{-1} - (\epsilon_\mathrm{o}\epsilon_{e,\infty})^{-1}]}.
\tag{4.37}
$$

Inclusion of non-parabolicity and screening effects will lead to

$$
\tau_{e-p,\mathrm{PO}} \;=\; \frac{\hbar^2 (E_e + \frac{E_e^2}{\Delta E_{e,g}})^{1/2} F^{-1}}{e_c^2 (2 m_{e,e,\mathrm{o}})^{1/2} k_\mathrm{B} T [(\epsilon_\mathrm{o}\epsilon_{e,s})^{-1} - (\epsilon_\mathrm{o}\epsilon_{e,\infty})^{-1}](1 + 2\frac{E_e}{\Delta E_{e,g}})}
$$

$$
F \;\equiv\; 1 - \delta \ln(1 + \delta^{-1}) - \frac{2\frac{E_e}{\Delta E_{e,g}}(1 + \frac{E_e}{\Delta E_{e,g}})}{(1 + 2\frac{E_e}{\Delta E_{e,g}})^2}[1 - 2\delta + 2\delta^2 \ln(1 + \delta^{-1})]
$$

$$
\delta \;\equiv\; (2\kappa\lambda_\mathrm{o})^{-2}, \tag{4.38}
$$

where $\epsilon_{e,s}$ and $\epsilon_{e,\infty}$ are the static and high frequency relative permitivities, κ is the carrier wave vector and λ_o is the screening length of the optical phonons.

(iv) *Scattering by Short Range Deformation Potential of Vacancies $\tau_{e-v,d}$*

$\tau_{e-v,d}$ also has a form similar to the relaxation time of electron-acoustic phonon scattering, due to a similar deformation potential, which is

$$
\tau_{e-v,d} \;=\; \frac{(\tau_{e-v,d})_\mathrm{o}(E_e + \frac{E_e^2}{\Delta E_{e,g}})^{-1/2}}{(1 + 2\frac{E_e}{\Delta E_{e,g}})[(1 - A)^2 - B]}
$$

$$
A \;\equiv\; \frac{\frac{E_e}{\Delta E_{e,g}}(1 - a_v)}{(1 + 2\frac{E_e}{\Delta E_{e,g}})}, \qquad a_v = \frac{\varphi'_{v,v}}{\varphi'_{v,c}}
$$

$$
B \;\equiv\; \frac{8\frac{E_e}{\Delta E_{e,g}}(1 + E_e/\Delta E_{e,g})a_v}{3(1 + 2\frac{E_e}{\Delta E_{e,g}})^2}
$$

$$
(\tau_{e-v,\mathrm{d}})_\mathrm{o} \;\equiv\; \frac{\pi\hbar^4}{\varphi'^2_{v,c} m_{e,e,\mathrm{o}}(2 m_{e,e,\mathrm{o}})^{1/2} n_v}, \tag{4.39}
$$

where n_v is the vacancy density, a_v is the ratio of the short range deformation potential coupling constants of vacancies for valence and conduction bands.

(v) *Scattering by Coulomb Potential of Vacancies $\tau_{e-v,\mathrm{C}}$*

$$
\tau_{e-v,\mathrm{C}} \;=\; \frac{\epsilon_s^2 (2 m_{e,e,\mathrm{o}})^{1/2}(E_e + \frac{E_e^2}{\Delta E_{e,g}})^{3/2}}{\pi (Z e_c^2)^2 n_v [\ln(1 + \xi) - \xi/(1 + \xi)](1 + 2\frac{E_e}{\Delta E_{e,g}})}
$$

$$
\xi \;\equiv\; (2\kappa\lambda_v)^2, \tag{4.40}
$$

Table 4.5: Parameters used in the relaxation time models for Bi_2Te_3, from fit to experimental results[10].

Parameter	Magnitude	Parameter	Magnitude
$m_{h,e,o}/m_e$	0.08	$m_{e,e,o}/m_e$	0.06
n_v, 1/m^3	1.04×10^{25}	ρ, kg/m^3	7.86×10^3
$\epsilon_{e,o}$	400	$\epsilon_{e,\infty}$	69.8
C_l, N/m^2	0.71×10^{11}	$\hbar\omega_o$, eV	0.0061
Z	0.1	$\varphi_{d,A,c}$, eV	35
$\varphi_{d,O,c}$, eV	40	$\varphi'_{v,c}$, J-m^3	1.2×10^{-46}
a_A, a_O, a_v	1.0	a, Å	10.45
$\Delta E_{e,g}$, eV	$0.13 - 1.08 \times 10^{-4}T$		

where Ze_c is the vacancy charge, and λ_v is the screening radius of the vacancy potential, and λ_v is given as

$$
\begin{aligned}
\lambda_v^{-2} &= \frac{4\pi e_c^2}{\epsilon_s} D_e(\mu), \quad \mu = E_F \\
D_e(\mu) &\equiv \frac{2^{1/2}(m_{e,e,o})^{3/2}}{\pi^2 \hbar^3}(\mu + \frac{\mu^2}{\Delta E_{e,g}})^{1/2}(1 + 2\frac{\mu}{\Delta E_{e,g}}),
\end{aligned}
\tag{4.41}
$$

where $D_e(\mu)$ is actually the density of states at the Fermi level.

Figure 4.11 shows the temperature dependence of the calculated average relaxation times described above. The parameters used in the calculation are listed in Table 4.5. Some parameters, e.g., the deformation potentials, are obtained by fitting the electrical conductivity with experimental results at 100 K. Overall, the scatterings by acoustic and optical phonons dominate the electrical transport of Bi_2Te_3. On the other hand $\langle\langle\tau_{e-v,d}\rangle\rangle$ and $\langle\langle\tau_{e-v,C}\rangle\rangle$ are orders of magnitudes larger than $\langle\langle\tau_{e-p,A}\rangle\rangle$ and $\langle\langle\tau_{e-p,O}\rangle\rangle$. Therefore, the scattering by the short-range deformation potential of vacancies and Coulomb potentials are unimportant for the electrical transport of
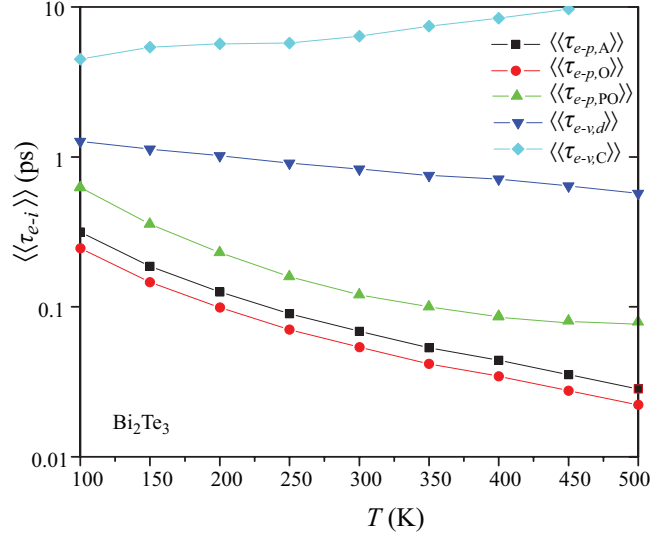
Figure 4.11: Variation of calculated average electron relaxation times for Bi_2Te_3 with respect to temperature, using the Kane band model for energy dispersion.

Bi_2Te_3. Note that $\langle\langle\tau_{e-p,\mathrm{PO}}\rangle\rangle$ is comparable with $\langle\langle\tau_{e-p,\mathrm{A}}\rangle\rangle$ and $\langle\langle\tau_{e-p,\mathrm{O}}\rangle\rangle$. Therefore, the polar scattering by optical phonons is also important.

4.3.4 Seebeck Coefficient

Figure 4.12 shows the variation of calculated $\alpha_{\mathrm{S},\parallel}$ of Bi_2Te_3 with temperature, using Eq. (4.22). The calculation was carried out using BoltzTraP, a software package adopting Boltzmann transport equations (BTE). Both the energy-dependent relaxation time models (Section 4.3.5) and the constant relaxation time model were used. We modified the BoltzTraP code and incorporated the relaxation time model into the integration, since BoltzTrap assumes a constant relaxation time. The corresponding Fermi energy at each temperature is determined by Eq. (4.26) along with the Kane band model for D_e. To incorporate the temperature dependence of the

125

band structure, we assume the band structure does not change with temperature, and shift the conduction band in the calculation to include the temperature dependence of the band gap $\Delta E_{e,g}$. Figure 4.12 shows that, the constant $\Delta E_{e,g}$ leads to much higher values for $T > 300$ K (intrinsic regime), while results calculated with the temperature-dependent $\Delta E_{e,g} = 0.13 - 1.08 \times 10^{-4} T$ agrees quite well with the experimental results. However, in the extrinsic regime ($T \leq 300$ K), there is only minor difference between the results with the two different settings for $\Delta E_{e,g}$. As shown in Fig. 4.12, with the same temperature-dependent $\Delta E_{e,g} = 0.13 - 1.08 \times 10^{-4} T$ eV, the two relaxation-time models give very similar results in the extrinsic regime, since one kind of carriers dominate the electrical transport. However, some deviation appears in the intrinsic regime, where the concentrations of the holes and electrons become comparable, and it increases with the increasing temperature. This phenomena indicate the temperature dependences of the mobilities of holes and electrons are different.

The band structure calculated with the experimental lattice parameters at 300 K was used in the above calculations for α_{S}. Temperature changes not only the carrier concentrations but also the lattice parameters. However, the band structure calculations adopting the lattice parameters under different temperatures, shows that the thermal expansion has negligible effects on the band structure. The change of lattice parameters from 0 K to 300 K only results in less than 2% change in the band gap. Compared with the actual temperature dependence of band gap[112], it seems that the temperature variation of the band gap is mainly due to lattice vibration.

Figure 4.13 shows the variation of α_{S} along the $\parallel$ and $\perp$ directions, with respect
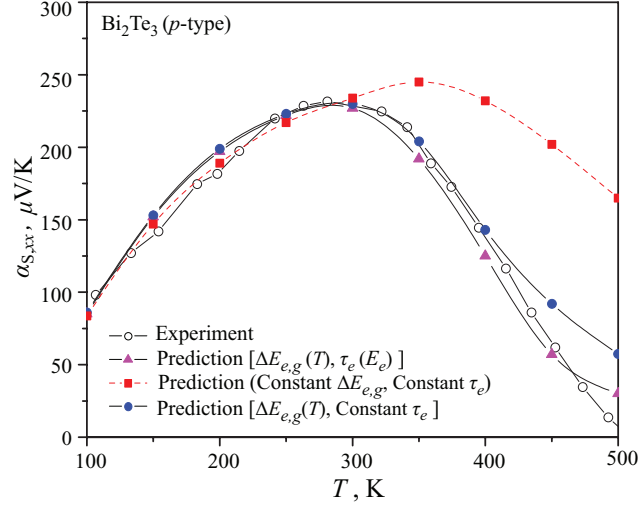
Figure 4.12: Variation of the calculated Seebeck coefficient for p-type Bi_2Te_3 with respect to temperature, compared with the available experimental results[10]. Both a temperature-dependent band gap $\Delta E_{e,g} = 0.13 - 1.08 \times 10^{-4}T$ eV and a constant $\Delta E_{e,g} = 0.13$ eV are used. Also shown are the predictions using the energy-dependent relaxation times and the constant relaxation time model.

to the chemical potential μ, at 300 K. Apparently, the two curves are very similar, indicating the isotropy of α_S. Figure 4.13 shows that for p-type Bi_2Te_3, the α_S peaks along the $\parallel$ and $\perp$ directions almost overlap. However, for n-type Bi_2Te_3, the absolute peak value α_S along the $\parallel$ direction is larger than that along the $\perp$ direction, though the peak positions are identical. In Fig. 4.13, μ_0 is the chemical potential value at which $\alpha_S = 0$. It is useful to rewrite the relation for α_S in Eq. (4.22) as

$$\alpha_S = \frac{k_B}{e_c} \frac{\langle E_e - \mu \rangle_{\sigma_e(E_e,\mu)}}{k_B T}, \quad \langle E_e - \mu \rangle_{\sigma_e(E_e,\mu)} = \frac{\int \sigma_e(E_e,\mu)(E_e - \mu) dE_e}{\int \sigma_e(E_e,\mu) dE_e}. \quad (4.42)$$

Here $\langle E_e - \mu \rangle_{\sigma_e(E_e,\mu)}$ is the $\sigma_e(E_e,\mu)$-averaged energy deviation from the chemical potential. Then we have

$$\mu_0 = \langle E_e \rangle_{\sigma_e(E_e,\mu_0)}, \quad (4.43)$$

127

which is the $\sigma_e(E_e)$-averaged energy and close to the middle of band gap. Therefore,

$$\alpha_{\mathrm{S}} = \frac{k_{\mathrm{B}}}{e_c} \frac{[\langle E_e \rangle_{\sigma_e(E_e,\mu)} - \langle E_e \rangle_{\sigma_e(E_e,\mu_0)}] - (\mu - \mu_0)}{k_{\mathrm{B}}T}. \tag{4.44}$$

$\langle E_e \rangle_{\sigma_e(E_e,\mu)}$ has a simple form if the nondegenerate approximation may be used, that is,

$$\begin{aligned} \langle E_e \rangle_{\sigma_e(E_e,\mu)} &\simeq \frac{\sigma_{e,e}\Delta E_{e,g}}{\sigma_{e,e} + \sigma_{e,h}} \\ &= \frac{1}{1 + be^{-2\epsilon/(k_{\mathrm{B}}T)}}\Delta E_{e,g}, \end{aligned} \tag{4.45}$$

where $\sigma_{e,e}$ and $\sigma_{e,h}$ are the electrical conductivity contributed by electrons and holes, $b = (\mu_h/\mu_e)(m_{e,h}/m_{e,e})^{3/2}$ (μ_h and μ_e are the mobilities of electrons and holes), and $\Delta E_e = \mu - \Delta E_{e,g}/2$ is the seperation of the chemical potential above the middle of the band gap. Apparently, for semiconductors with large band gap (e.g., $\Delta E_{e,g} > 10k_{\mathrm{B}}T$), the absolute value of the maximum α_{S} can be estimated as

$$|\alpha_{\mathrm{S},max}| = \frac{k_{\mathrm{B}}}{|e_c|}\frac{\Delta E_{e,g}}{2k_{\mathrm{B}}T}. \tag{4.46}$$

For small $2\Delta E_e/k_{\mathrm{B}}T$, we have

$$\langle E_e \rangle_{\sigma_e(E_e,\mu)} \simeq \frac{\Delta E_{e,g}}{1+b}[1 + \frac{2b\Delta E_e/(k_{\mathrm{B}}T)}{1+b}]. \tag{4.47}$$

Therefore,

$$\alpha_{\mathrm{S}} \simeq \frac{k_{\mathrm{B}}}{e_c}\frac{[\frac{2b\Delta E_{e,g}}{(1+b)^2 k_{\mathrm{B}}T} - 1](\mu - \mu_0)}{k_{\mathrm{B}}T}. \tag{4.48}$$

For narrow band-gap semiconductors, as shown in Fig. 4.13, Eq. (4.48) is a good approximation for α_{S} when $|\mu - \mu_0| < \Delta E_{e,g}/2$. When μ move towards the band edge, the effects of opposite charges becomes smaller; when μ move further into the band
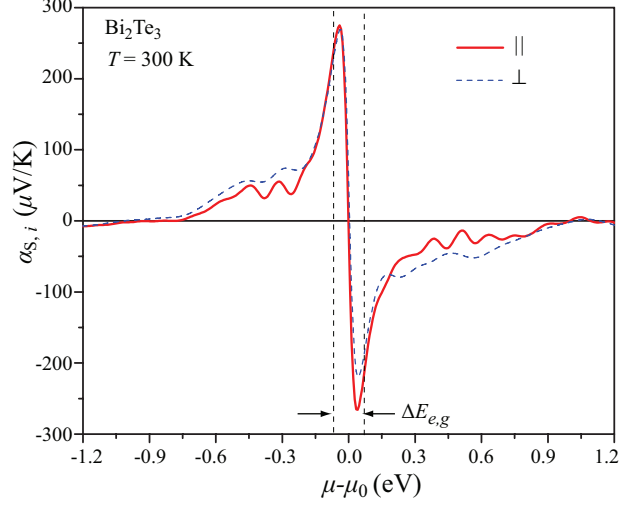
Figure 4.13: Variation of the calculated Seebeck coefficient of Bi_2Te_3 with different lattice parameters at $T = 300$ K, with respect to the chemical potential μ.

edge, $\langle E_e \rangle_{\sigma_e(E_e,\mu)}$ will become closer to μ. Therefore α_S will achieve the maximum near the band edge, and the maximum value can be estimated from Eq. (4.48). Assuming $b = 1$ and the maximum is achieved at the band edge, for Bi_2Te_3 at 300 K, $|\alpha_S|_{max} \simeq 320$ μV/K, close to the maximum in Fig. 4.13.

4.3.5 Electrical Conductivity and Electric Thermal Conductivity

Figure 4.14 shows the calculated electrical conductivity of Bi_2Te_3 along the $\parallel$ and $\perp$ directions, wherein the Kane band model based relaxation times are used. The temperature-dependent band gap $\Delta E_{e,g} = 0.13 - 1.08 \times 10^{-4}T$ eV and the corresponding chemical potential calculated in Section 4.3.2 are adopted in the calculation. The parameters for the relaxation time models are listed in Table 4.5. Below 300 K,

the ratio $\sigma_{e,\parallel}/\sigma_{e,\perp}$, is around 2.2 and almost temperature independent. But above 300 K, $\sigma_{e,\parallel}/\sigma_{e,\perp}$ increases with increasing temperature. From the results shown in Fig. 4.14, this is because $\sigma_{e,\parallel}$ changes much faster than $\sigma_{e,\perp}$ at high temperatures. Note the calculated $\sigma_{e,\parallel}/\sigma_{e,\perp}$ is lower than the experimental values (around 2.95 [113]). A reason can be neglecting of the direction dependence of the effective masses.
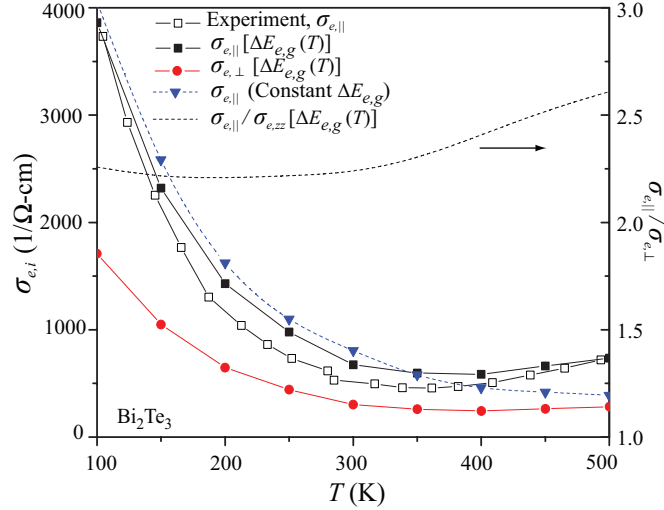
Figure 4.14: Variation of calculated directional electrical conductivity for Bi_2Te_3 with respect to temperature, using the Kane band model and energy-dependent relaxation times, and comparison with the available experimental results. [10]

We also used a constant band gap $\Delta E_{e,g} = 0.13$ eV for the calculation of σ_e using the above energy dependent relaxation time models. The same parameters in Table 4.5 are used, and the results are also plotted in Fig. 4.14. Below 300 K, the $\sigma_{e,\parallel}$ calculated with a constant $\Delta E_{e,g}$, is fairly close to those results with a temperature-dependent $\Delta E_{e,g}(T)$. But in the intrinsic regime, the larger band gap suppresses the thermal excitation of carriers and thus leads to lower σ_e values. Note, with a constant $\Delta E_{e,g}$, $\sigma_{e,\parallel}$ continues to decay without any rebound shown in the experimental results.
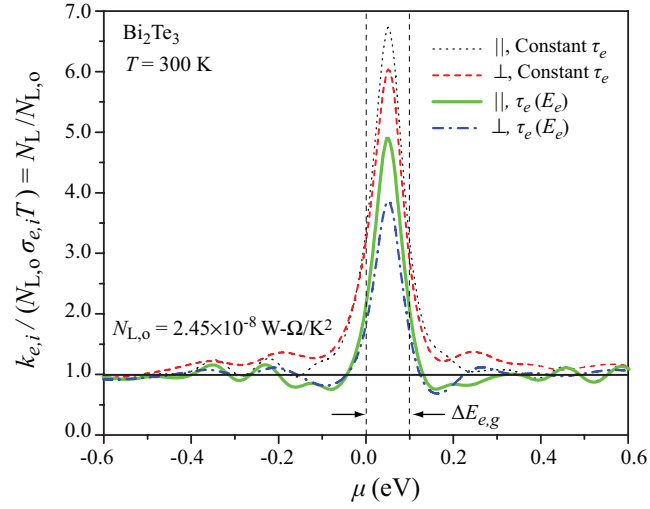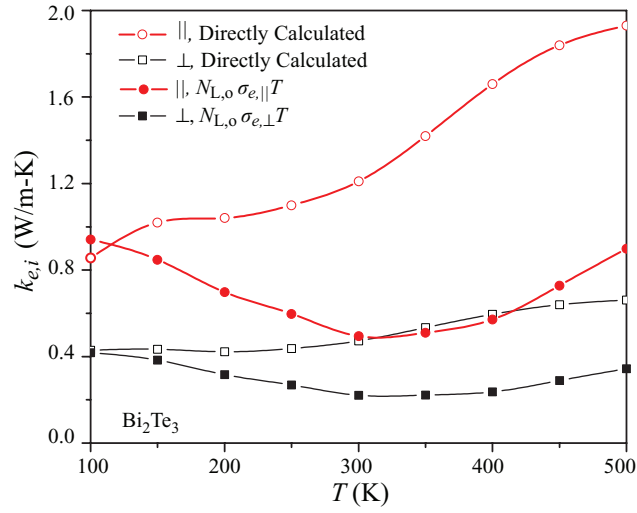
Figure 4.15: (a) Variation of the calculated, scaled Lorenz number for Bi_2Te_3 (along $\parallel$ and $\perp$), with respect to the chemical potential. Both the constant relaxation time model and the energy-dependent relaxation time model (with the Kane band dispersion) results are shown. (b) Variation of the calculated k_e along the $\parallel$ and $\perp$ directions, with respect to temperature. The results calculated using the constant $N_{L,\circ}$, i.e., $N_{L,\circ}\sigma_e T$, are also shown.

However, a temperature-dependent $\Delta E_{e,g}(T)$ yields a much better agreement with the experiments at high temperatures, indicating the temperature dependence of the band gap is important in predicting the temperature dependence of the electrical conductivity.

Traditionally, the Wiedemann-Franz law, $k_e = N_{\mathrm{L}}\sigma_e T$, where N_{L} is the Lorenz number, is used to calculate the electric thermal conductivity k_e on the basis of σ_e. However, for semiconductors, N_{L} may not be the values used for metals $[N_{\mathrm{L},\circ} = (\pi^2/3)k_{\mathrm{B}}^2/e_c^2]$, especially when the chemical potential is near the center of the band gap[?]. Figure 4.15(a) shows the variation of the directly calculated Lorenz number N_{L} (scaled with $N_{\mathrm{L},\circ}$) for Bi_2Te_3 (along $\parallel$ and $\perp$) at 300 K, with respect to the chemical potential. The results are similar to those found by Chaput et al.[?] for doped skutterudites. When the sample is heavily doped (the chemical potential is deep inside the valence or conduction band), $N_{\mathrm{L}}/N_{\mathrm{L},\circ}$ is close to 1.0. However, for intermediate doping, $N_{\mathrm{L}}/N_{\mathrm{L},\circ}$ can be smaller than 1.0, and the minimum is around 0.7. For small doping concentrations or intrinsic regime, $N_{\mathrm{L}}/N_{\mathrm{L},\circ}$ may be much larger than 1.0. Figure 4.15(a) also shows the constant relaxation time model will lead to a larger N_{L}, compared to that for the energy-dependent relaxation time model discussed above. For both relaxation time models, N_{L} along the $\parallel$ direction is slightly larger than that along the $\perp$ direction. Figure 4.15(b) shows the temperature dependence of the electric thermal conductivity calculated according to Eq. (4.22) and that calculated from $N_{\mathrm{L},\circ}\sigma_e T$. The results from Eq. (4.22) shows that k_e for both directions increase with increasing temperature, while $N_{\mathrm{L},\circ}\sigma_e T$ results show valleys near the room temperature. Due to the significant changes of N_{L} in the intrinsic regime,
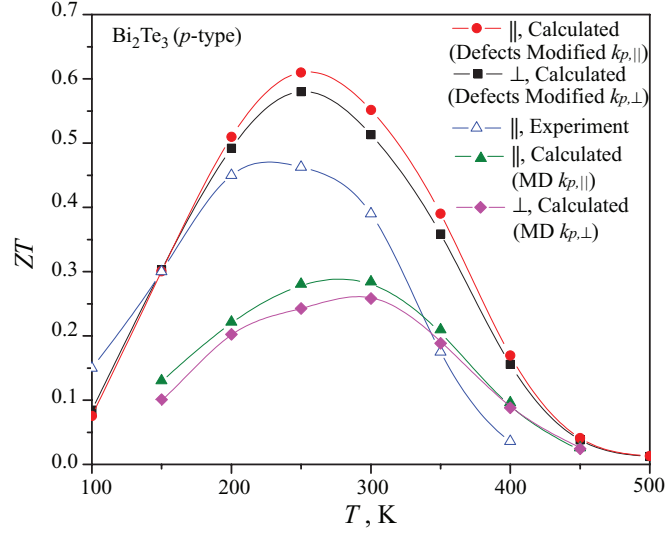
Figure 4.16: Variation of calculated directional figure of merit for Bi_2Te_3 (along $\parallel$ and $\perp$), with respect to temperature. Both the results with the directly calculated k_p and that modified by defects are presented. The experimental results[10] are also shown.

$N_{L,\circ}\sigma_e T$ underestimates k_e at high temperatures.

4.3.6 Figure of Merit

Figure 4.16 shows the variation of the figure of merit ZT for the p-type Bi_2Te_3 specimen of experiment[10] along the $\parallel$ and $\perp$ directions, with respect to temperature. The lower two curves are based on the directly (MD) calculated k_p. Since k_p as well as σ_e is very sensitive to defects, which are always present in fabricated specimens, for comparison between the calculated and measured ZT, we used a modified k_p and the results are shown with the top two curves. Due to the difficulty in modeling various defects, the modified k_p was obtained by fitting the total thermal conductivity to the experimental results[10] at 300 K and then using the $1/T$ law at other temperatures.

133

The experimental results are also shown in Fig. 4.16. The ZT with a modified k_p is higher than experimental results above 200 K, mainly due to the overestimation of σ_e. The calculated ZT reaches its maximum around 250 K. ZT along the $\parallel$ direction is higher than that along the $\perp$ direction between 200 K and 400 K, due to the larger ratio $\sigma_{e,\parallel}/\sigma_{e,\perp}$ compared to $k_{p,\parallel}/k_{p,\perp}$. Note that the experimental $\sigma_{e,\parallel}/\sigma_{e,\perp}$ is larger than the calculated results (discussed above), so the difference in the figure of merits along the $\parallel$ and $\perp$ direction is expected to be even larger.

4.4   Summary and Conclusion

The interatomic potentials for Bi_2Te_3 have been developed and the calculated elastic constants and thermal expansion coefficients agree well with the experimental data, indicating the proposed force field is suitable to describe both the harmonic and anharmonic behaviors of Bi_2Te_3. The interaction between two Te1 atoms in the neighboring layers is a mixture of the electrostatic interaction and the van der Waals interaction and behaves like an ionic bond. The force constant difference between the Te1-Te1 and Te2-Bi bonds leads to a phonon band gap near 2.5 THz. There is only small difference between the in-plane and cross-plane vibrations and no significant two-dimensional elastic behavior has been found in this layered structure. However, the anisotropy in the polarized Grüneisen parameter shows much stronger anharmonicity along the cross-plane direction, which is mainly due to the high anharmonic Te1-Te1 interaction.

The temperature dependence of the in-plane and cross-plane lattice thermal con-

134

ductivity $k_{p,\mathrm{A},\parallel}$ and $k_{p,\mathrm{A},\perp}$ has been calculated in a temperature range from 150 K to 450 K. The ratio $k_{p,\mathrm{A},\parallel}/k_{p,\mathrm{A},\perp}$ varies from 1.55 to 2.17 in this temperature regime. Since the elastic properties along the two directions are nearly the same, the difference between $k_{p,\mathrm{A},\parallel}$ and $k_{p,\mathrm{A},\perp}$ is believed to be mainly due to the different inharmonicity along the two directions. The calculated in-plane thermal conductivity roughly follows the $1/T$ law while the calculated cross-plane lattice thermal conductivity seems to have a slightly stronger temperature dependence(i.e., $1/T^{1.23}$), which may be due to the larger thermal expansion effects along that direction. The decomposition of the lattice thermal conductivity shows that the long-range acoustic phonons dominate the heat transfer in both the in-plane and cross-plane directions. The contribution from the long-range acoustic phonons $k_{p,\mathrm{A},lg}$ has a strong temperature dependence; in contrast, the contribution from the short-range acoustic phonons $k_{p,\mathrm{A},sh}$ and that from the optical phonons $k_{p,\mathrm{O}}$ are also temperature-independent. Also, at each temperature point, $k_{p,\mathrm{A},sh}$ and $k_{p,\mathrm{O}}$ along the in-plane and cross-plane directions are almost identical. Therefore, $k_{p,\mathrm{A},sh}$ and $k_{p,\mathrm{O}}$ are not sensitive to the inharmonicity. The sum of $k_{p,\mathrm{A},sh}$ and $k_{p,\mathrm{O}}$ provides a lower limit for the doped, bulk Bi_2Te_3, which is about 0.2 W/m-K at 300 K. By using direction-dependent $T_{D,\infty}$ and γ_{G}, the Slack model was also extended for anisotropic materials. The extended Slack model gives a good estimation for both the in-plane and cross-plane lattice thermal conductivity, indicating the phonon transport along a given direction is only affected by the elastic and inharmonic properties along that direction.

We have also calculated the temperature dependence of α_{S}, σ_e, and k_e, over the temperature range from 100 K to 500 K. These calculation are based on the band

135

structure, μ, and τ_e. The Kane band model is found to be appropriate to describe the non-parabolicity of the Bi_2Te_3 band structure. The fitting with the carrier concentration and μ shows that the temperature dependence of the band gap is important to give a good prediction. The thermal expansion has negligible effects on the relationship between α_S and μ, therefore, the effects of temperature on α_S are mainly through changing the distribution function and μ. Both the constant relaxation time model and the analytic relaxation-time model with the non-parabolic Kane model for energy dispersion, have been used in the calculations for α_S. The results show α_S is sensitive to the temperature dependence of the band gap and the relaxation time models in the intrinsic regime.

The fitting for σ_e using the relaxation time model also shows that the polar scattering by optical phonons and the scattering by the deformation potential of acoustic and optical phonons predominate the electron transport in Bi_2Te_3. The scattering by the short-range deformation potential of vacancies and the coulomb potentials are negligible. The comparison of the temperature dependence of different scattering mechanisms also shows that the temperature dependence of the band gap is important to describe the temperature dependence of σ_e. It is also found that the Lorenz number can be smaller than the value for metals for intermediate doping and will become much larger in the intrinsic regime. In the relaxation time models used, some parameters are found by fitting to the experimental data on σ_e. Further work would use the first-principle methods [e.g., Eq. (4.30)] to calculate the scattering rates by acoustic and optical phonons.

Chapter 5

Phonon Conductivity of Filled Skutterudites

5.1 Filled Skutterudites

Binary skutterudites are structures with the general formula MX_3, where M is one of the group 9 transition metals (Co, Rh, or Ir), and X is a pnictogen. Skutterudites are characterized by a complex crystalline structure containing large cages and four-membered planary rings of X (shown in Fig. 5.1). It has been observed that filling the cages leads to a dramatic decrease in the phonon conductivity [114, 115]. Due to their good electronic properties (high Seebeck coefficient and high electrical conductivity), this reduction in phonon conductivity makes the filled skutterudites promising for thermoelectric applications.

One mechanism that has been evoked to explain the significant decrease of the phonon conductivity in filled skutterudites is a strong unharmonic rattling motion of
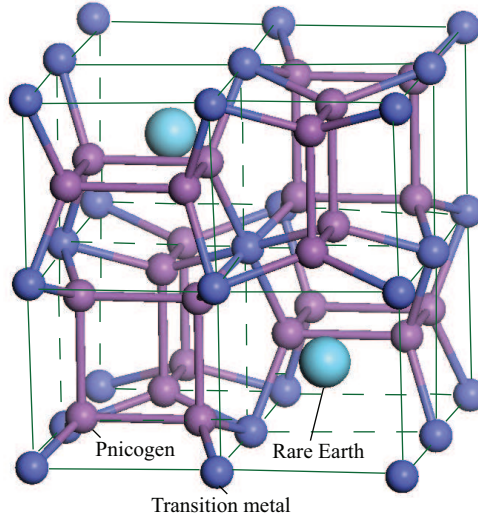
Figure 5.1: Cubic structure of skutterudites. Two fillers in the cages are also shown.

the filling atom. Large ADPs of the filler ions in filled-skutterudites with a drastically reduced phonon conductivity has been observed [116], which is believed to result from the rattling motion of fillers in the skutterudite cages. Perhaps the most important evidence of rattling comes from the investigations of low temperature specific heat measurements [117], which suggests the presence of Einstein oscillators.

To clarify the mechanisms in the reduction of phonon conductivity in filled skutterudites, investigation of the phonon transport at the atomic level are needed. Present work reports the lattice dynamics calculations and direct molecular dynamic (MD) simulations for the thermal conductivity of $CoSb_3$ and $Ba_x(CoSb_3)_4$ on the basis of quantum mechanics, which provides important information for the filler-host interaction and interphonon scattering. First, the vibration spectrum and dispersion of the empty and fully-Ba-filled $CoSb_3$ structure are calculated and compared. Then the force fields for this two structures are developed using the *ab initio* calculations. Together with the Green-Kubo method, the MD simulations are used to directly pre-

dict the thermal conductivity of the two structures. Thereafter, the role of filler in determining the phonon transport is discussed and modelled.

5.2 Empty and Filled Structure

The *ab initio* calculations were performed for the empty $CoSb_3$ and fully-filled $Ba(CoSb_3)_4$ structure using ABINIT package [118] within the density-functional theory (DFT) framework, with a planewave basis and the general gradient approximation (GGA) parameterized by Perdew et al. [106] to the exchange-correlation potential. Both the lattice constants and atomic positions of $CoSb_3$ and the fully-filled $Ba(CoSb_3)_4$ were relaxed until the forces on the atoms were smaller than 2.6×10^{-3} eV/Å. So far in experiments no fully Ba-filled $CoSb_3$ cage has been achieved, due to the long-range coulomb interactions [119]. Then fully-filled $Ba(CoSb_3)_4$ may not exist, but it can simplify the calculations and still provide useful information about the filler-host interactions. A $2 \times 2 \times 2$ grid of special κ-points was sufficient to obtain well-converged results and the kinetic energy cutoff is 35 hartree. The calculated structure parameters and their comparison with some other calculations are shown in Table 5.1. The lattice constant of the relaxed $CoSb_3$ is $a = 9.14$ Å, which is slightly larger than the experimental value[23] $a = 9.04$ Å. However, it is the same as the DFT (GGA) result from Mahan et al.[22]. The internal parameters u and v for the relaxed $CoSb_3$ structure are in good agreement with both the experimental and DFT results in literature [22, 11, 23]. For $Ba(CoSb_3)_4$, the comparison with the LDA calculations for $Ba(CoSb_3)_8$ performed by Kajitani et al [24] shows a reasonable agreement.

Table 5.1: Comparison among the structure parameters of $CoSb_3$ and $Ba(CoSb_3)_4$ obtained from the *ab initio* calculations and some theoretical and experimental results in the literatures [22, 11, 23, 24].

Parameters	$CoSb_3$	$Ba(CoSb_3)_4$
a (Å)	9.14 (GGA) [22]	9.12^a (LDA) [24]
	8.94 (LDA) [22]	9.27 (GGA, this work)
	8.94 (LDA) [11]	
	9.04 (Exp.) [23]	
	9.14 (GGA, this work)	
u	0.3332 (GGA) [22]	$0.3334/0.3360^a$ (LDA) [24]
	0.3328 (LDA) [22]	0.3386 (GGA, this work)
	0.3354 (Exp.) [23]	
	0.3346 (GGA, this work)	
v	0.1594 (GGA) [22]	$0.1587/0.1605^a$ (LDA) [24]
	0.1599 (LDA) [22]	0.1619 (GGA, this work)
	0.1579 (Exp.) [23]	
	0.1585 (GGA, this work)	
Co-Sb (Å)	2.53 ^{c}(Exp.) [23]	2.52/2.53 (LDA) [24]
	2.55 (GGA, this work)	2.59 (GGA, this work)
Sb-Sb (Å)	2.90/2.98 ^{c}(Exp.) [23]	2.93/3.03 ^{b} (LDA) [24]
	2.89/3.03 (GGA, this work)	2.99/3.00 (GGA, this work)
Co-Sb-Co (degree)	126.9 ^{c} (Exp.) [23]	126.9 (LDA) [24]
	126.9 (GGA, this work)	126.9 (GGA, this work)
Sb-Co-Sb (degree)	85.6 ^{c}(Exp.) [23]	84.6/93.9 (LDA) [24]
	85.7 (GGA, this work)	84.2 (GGA, this work)

^{a} The data are for $Ba(CoSb_3)_8$ [24].

^{b,c} The values are calculated from the published lattice parameters [24, 23].

Table 5.1 shows that the addition of Ba filler will slightly increase the lattice constant as well as the internal parameters u and v. This is also apparent in the calculations[24] for the half-filled $Ba(CoSb_3)_8$, which show a larger lattice constant and two groups of Sb sites. The most significant change is the bond length for the short Sb-Sb bond, which increases from 2.888 Å to 2.993 Å. Thus the intra rectangular pnicogen ring becomes closer to a square in the fully-filled structure. On the other hand, there are only minor changes in other bond lengths and bond angles.

The GGA calculations using the ABINIT package[118] were adopted to investigate the interactions between the filler and the host. Figure 5.2(a) shows the variation of calculated total energy of $BaCo_8Sb_{24}$ with respect to the absolute displacements from the center of the cage along the [100], [110], and [111] directions. Apparently, the three curves overlap quite well, indicating the energy surface for the filler-host interactions is isotropic. At the same time, Fig. 5.2(b) shows the dependence of the calculated lattice energy of $ReCo_8Sb_{24}$ on the displacement of the fillers (Re = Ba, Ce, La and Yb, GGA for Ba and La, LDA for Ce and Yb) from the center along the [100] direction. It is apparent that all the potentials are nearly harmonic with respect to the filler site. Some anharmonic deviation are marginally evident at large displacements. Similar behavior is also found by Feldman et al.[120] for $La(Ce)Fe_4Sb_{12}$ and Ghosez and Veithen[121] for $TlFeCo_3Sb_{12}$. Figure 5.2(b) also shows that the order of the bare force constant for the fillers is Ba > La > Ce > Yb, that is, the heavier the filler, the smaller bare force constant and in turn the lower bare vibration frequency. From Fig. 5.2(b), we can obtain the bare vibration frequencies for Ba, La, Ce, and Yb, which are 3.31, 2.71, 2.23, 1.80 THz, respectively. The bare frequencies for La

and Ce obtained here are slightly higher than those [120] reported for La (2.24 THz) and Ce (2.04 THz) in La(Ce)Fe$_4$Sb$_{12}$. Since interaction between the filler and the host is of strong covalent characters [121], we assumed the filler only interacts with the nearest Sb and Co neighbors and then fitted the interatomic force constants with the scanned filler-host energy surface. The results are shown in Table 5.2. The fitted force constants show that all the fillers have a strong coupling with the nearest Sb atoms, but the coupling with Co atoms is very weak due to the longer seperation.

Table 5.2: Fitted force constants for the interaction between the filler Re (Re = Ba, Ce, La and Yb) and the CoSb$_3$ host.

Interactions	Ba	La	Ce	Yb
$\Gamma_{\text{Re}-\text{Sb}}$ (eV/Å^2)	1.70	1.11	0.96	0.63
$\Gamma_{\text{Re}-\text{Co}}$ (eV/Å^2)	0.008	0.013	0.033	0.0027

Using the response-function theory (RFT) and applying perturbations based on the structure symmetry, the interatomic force constants Γ_{i-j} are directly determined using ABINIT. Those force constants were projected on the local coordinates to be decomposed into the longitudinal and transversal force constants. The resulting longitudinal force constants Γ_{L} are expected to correspond to the two-body stretching force constant, and the transversal force constants Γ_{T} are believed to result from the many-body interactions.

Figure 5.3 shows the comparison of the calculated longitudinal force constants of CoSb$_3$ and Ba(CoSb$_3$)$_4$ structure. The force constant values that change significantly after the Ba insertion into the cage vacancy are shown in a box. Figure 5.3 shows
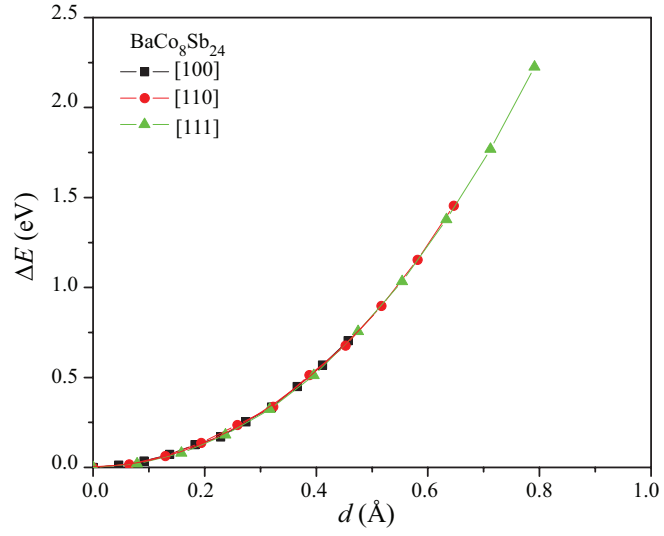
(a)
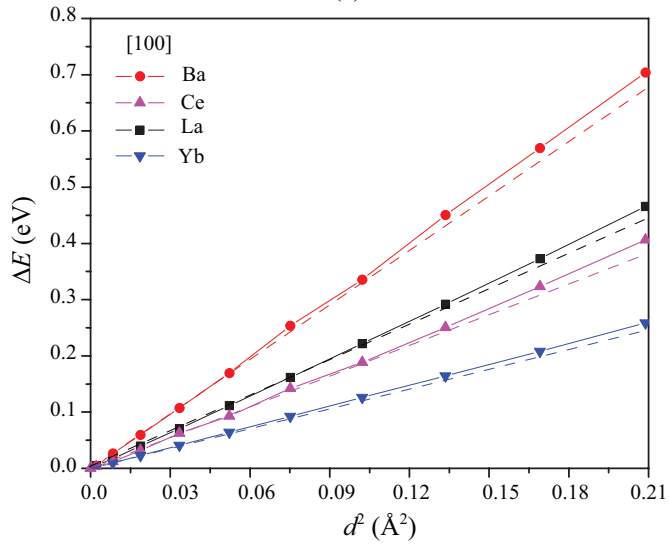
(b)

Figure 5.2: (a) Variations of calculated LDA/GGA total energy of $BaCo_8Sb_{24}$, with respect to displacements from center of the cage along the [100], [110], and [111] directions. (b) Variations of calculated LDA/GGA total energy of $ReCo_8Sb_{24}$ (Re = Ba, Ce, La), with respect to displacement from center of the cage along [100] directions. The dashed lines show the slopes of those LDA/GGA energy curves at $d^2 = 0$.
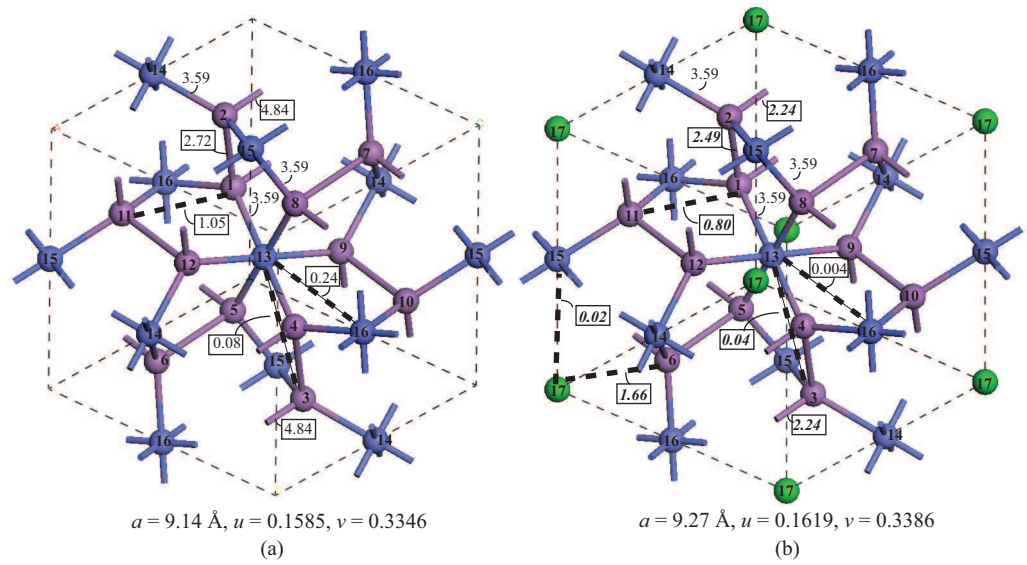
Figure 5.3: Comparisons between the longitudinal force constants Γ_{i-j} of CoSb$_3$ and BaCo$_8$Sb$_{24}$, obtained from the *ab initio* calculations and from RFT. Atoms 1-12 are Sb atoms, 13-16 are Co atoms, and 17 is Ba atom. The values that changes significantly due to the addition of filler are shown in box.

that, except for Co-Sb bonds, the force constants of other bonds are more or less changed by the Ba filler. The most important change is Γ_L of the short Sb-Sb bond, which decreases around 50% and becomes close to that of the long Sb-Sb bond. Γ_L of the long Sb-Sb bond and the Sb-Sb inter-rectangle bond also decrease 10 % and 20 %, respectively. The calculated Γ_L of Sb-Ba interaction is 1.66 eV/Å^2, in good agreement with 1.7 eV/Å^2 (shown in Table 5.2) obtained by fitting the energy surface.

5.3 Lattice Dynamics

To investigate the effects of the fillers on the lattice vibrations of skutterudite structure, the normalized phonon total density of states (DOS), projected density of states (PDOS), and dispersion curves of the unfilled $CoSb_3$ and the filled $Ba(CoSb_3)_4$ were calculated using RFT and lattice dynamics. Figures 5.4(a) and (b) show the calculated phonon DOS of $CoSb_3$ and $Ba(CoSb_3)_4$, respectively. The calculated DOS for $CoSb_3$ is in good agreement with the other calculations in the literature [11, 121]. Apparently, the existence of the filler, Ba atoms, affects the overall total vibration spectrum: first the cut-off frequency is significantly reduced from 8.3 THz to 7 THz; second the peak around 5 THz is separated from the lower frequency spectrum; third the small gap around 3 THz disappears and the large gap above 6 THz becomes much smaller; and fourth there are more peaks appearing between 1.5 THz and 3.0 THz. The fourth change is believed to be due to the vibration of Ba atoms and its hybridization with the vibrations of Co and Sb. However, the first three changes are unlikely due to the disturbance from Ba atoms. As will be shown below, they result from the weakened bonds caused by the presence of the Ba atom. The vibration spectrum of Ba atoms actually occupies a wide frequency regime and is distinct from that of an Einstein oscillator, which only occupies a narrow band regime.
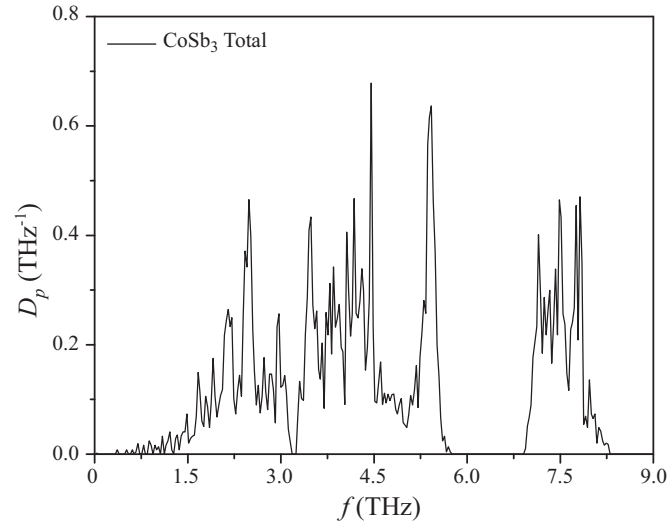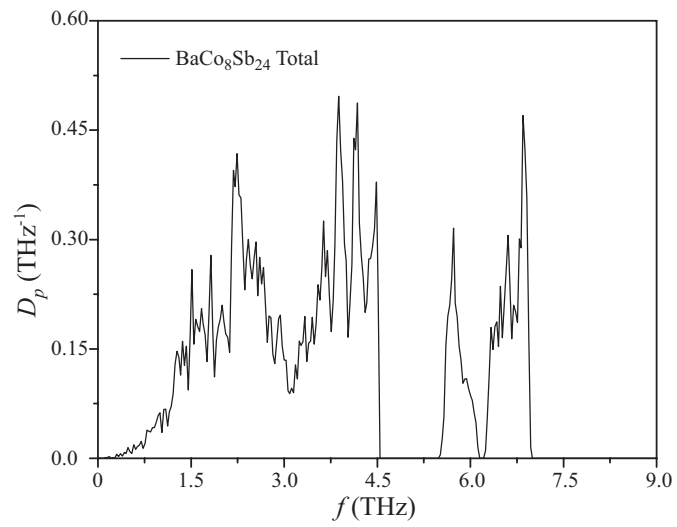
Figure 5.4: (a) Normalized phonon DOS of CoSb$_3$. (b) Normalized phonon DOS of Ba(CoSb$_3$)$_4$.

Phonon dispersion may provide more information on the effects of the filler in CoSb$_3$ structure. Figure 5.5 shows the phonon dispersion of (a) CoSb$_3$ and (b) Ba(CoSb$_3$)$_4$. The dispersion curves for CoSb$_3$ seem to be significantly changed by Ba atoms. First, the acoustic branches become flatter and their cutoff frequency is reduced from around 1.5 THz to 1.0 THz, which means the group velocity of acoustic branches is reduced by around 30%. Second, the optical branches are squeezed, i.e., both the vibration frequency and group velocity are reduced. Furthermore, there are strong disturbance near 2 THz. The first two changes in the dispersion, however, are not due to the disturbance of the Ba vibration, but due to the weakened bond force constant by the presence of the Ba atom. This is more clear by comparing the dispersion curves plotted in Fig. 5.6 and those in Fig. 5.5. In Fig. 5.6, the potential model C proposed by Feldman and Singh [11] was adopted for the CoSb$_3$ host, and the filler-host interaction is fitted with the scanned energy surface, as mentioned in Section 5.2. Figure 5.6(a) shows the dispersion for the empty CoSb$_3$ structure calculated from Feldman-Singh's model, which is in good agreement with the result from RFT [shown in Fig. 5.5(a)]. When the Ba atom is inserted into the cage, as shown in Fig. 5.6(b), the overall change in the dispersion is minor if the force field for the host keeps the same. The acoustic branch below 1.5 THz is almost untouched and the optical phonon spectrum between 1.5 THz and 6 THz actually expands, which is in direct contrast with the result shown in Fig. 5.5(b). Comparing the dispersions for the empty and filled structure, phonon transport is more likely to be suppressed in the filled structure with a dispersion shown in Fig. 5.5(b), as compared to the dispersion shown in Fig. 5.6(b).

147
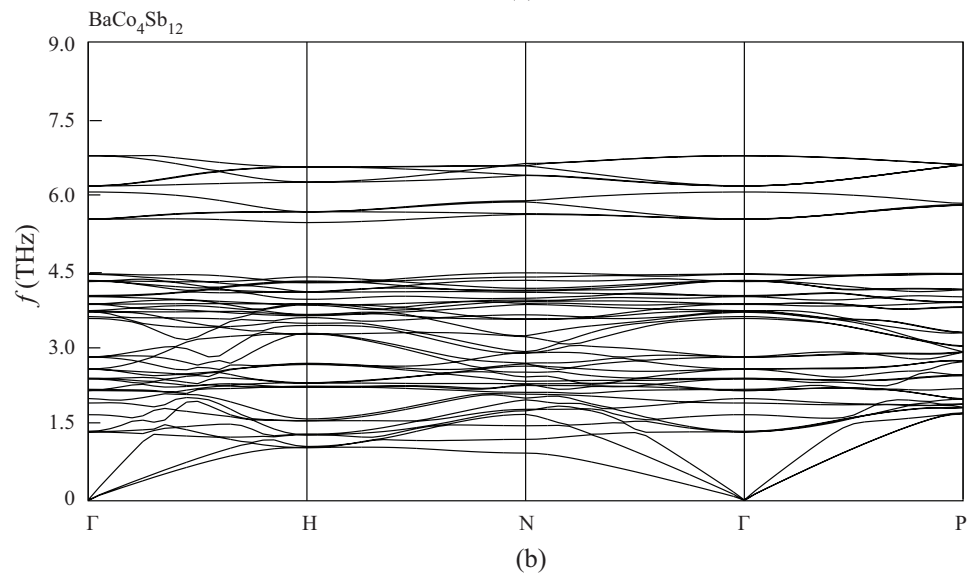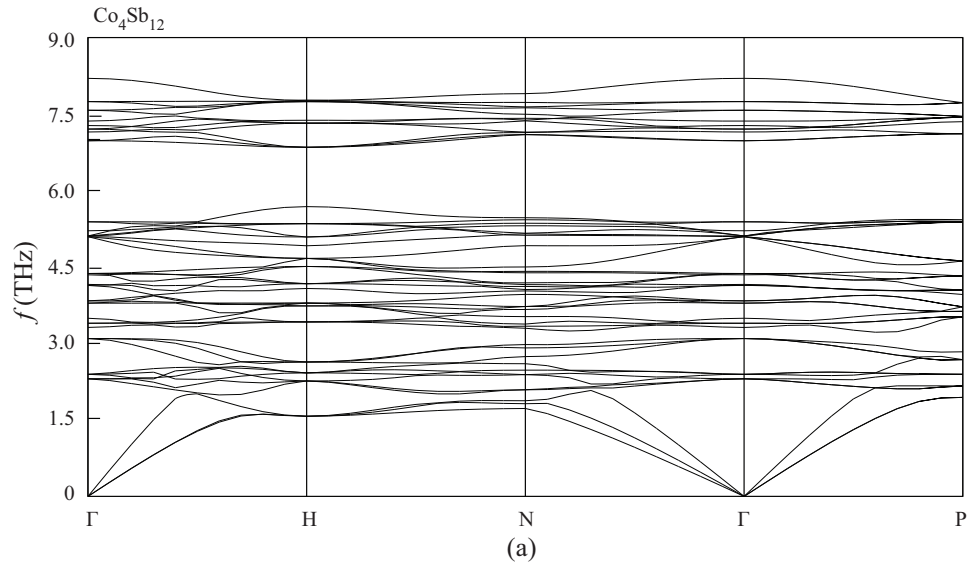
Figure 5.5: Phonon dispersion calculated by RFT for (a) Co_4Sb_{12}, and (b) $Ba(CoSb_3)_4$.
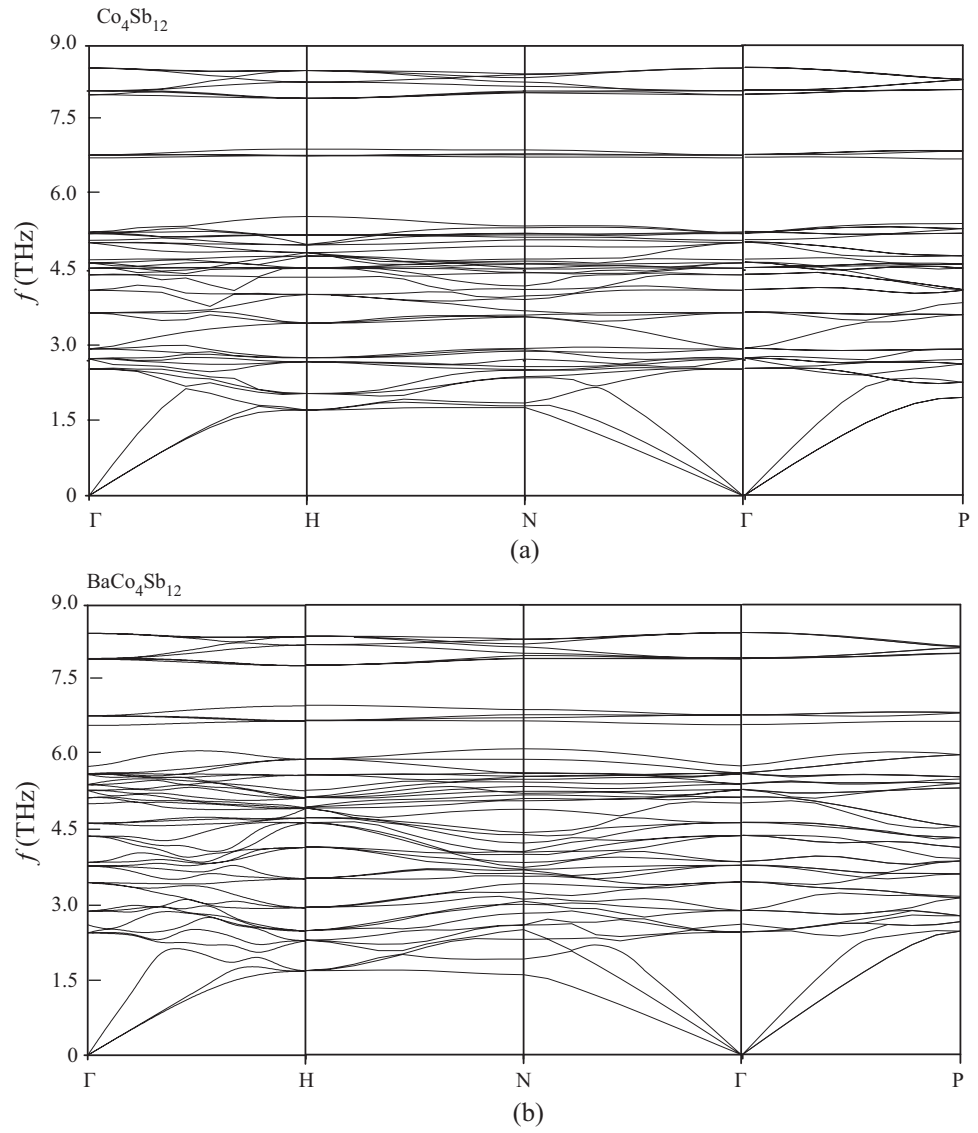
Figure 5.6: Phonon dispersion calculated by the classical force field for (a) Co_4Sb_{12} and (b) $Ba(CoSb_3)_4$. Feldman-Singh's model C [11] is adopted for the $CoSb_3$ host, and the filler-host interaction is fitted with the energy surface.

5.4   Interatomic Potentials

Lutz and Kliche[122] (LK) fitted six-parameter central force constant model to the infrared data of $CoSb_3$. Their model accurately predicts the LDA volume dependence of the total energy and most eigen mode frequency. However, the LK model does not contain bond angle force constants, which may be important due to the significance of covalent bonding in $CoSb_3$ structure. Feldman et al. [123] proposed a harmonic force field which includes the bond-angle distortions by fitting the parameters to the available infrared data and LDA results. They also fitted the cubic anharmonic terms of the interatomic potentials with the LDA results. Their model predicts the zone-center mode frequencies and the anharmonicity in the volume-dependent LDA results quite well. The effects of atomic charges are assumed to be negligible in Feldman's model as well as LK model, due to the strong covalent charaters of the interatomic bond. Nevertheless, a cubic bond-stretching potential passes through a maximum and might cause some instability in the molecular dynamics for some cases. Therefore, the quadratic anharmonic terms should be involved for a robust MD simulation, which, however, is very challenging to fit accurately. Of the many functional forms used to model interatomic interactions, the Morse potential is found to be very useful, especially for covalent bonds. The Morse potential has the following form [124]

$$\varphi = \varphi_\circ \{[1 - \exp(-a(r - r_\circ))]^2 - 1\}, \tag{5.1}$$

where $\varphi_\circ$ is the depth of the potential energy minimum and $r_\circ$ is the equilibrium bond length. We first determined the parameters in the Morse potentials for $CoSb_3$ by fitting their harmonic and cubic anharmonic terms with the force field proposed

by Feldman et al. [123]. As in the force field proposed by Feldman et al. [123], this force field model includes the nearest-neighbor Co-Sb interaction, the nearest-neighbor Co-Co interaction, the two nearest-neighbor Sb-Sb interactions (both long and short bonds) in the rectangles, the two nearest-neighbor Sb-Sb interactions between rectangles, and the two bond-angle distortions associated with the two distinct Co-Sb-Sb angles. As expected, this force field produces the same predictions for the zone-center normal modes and elastic constants as those calculated by Feldman et al. [11] The potential for the filler-host interaction can be obtained by fitting the energy surface calculated in Section 5.3. However, for a filled skutterudite structure, the filler may significantly affect the interatomic interactions [123]. Therefore, for the direct comparison between the empty structure and the fully-filled one, we also need to obtain the potentials for filled $CoSb_3$ structure as well as the empty one on the same platform and using the same approach. Ba was chosen as the filler to investigate as high filling fraction has been achieved experimentally [12]. Normally, interatomic potentials are developed by fitting the energy surface scanned by the *ab initio* calculations or the experimental data, which is extremely challenging, especially for structures with strong interatomic coupling, due to the difficulty in decomposing the different interactions. With the motivation from the dynamical matrix calculations in Section 5.3, a new approach based on the response function theory [118, 125, 126] was adopted here. First, the interatomic force constants for the optimized structure were calculated. Then, by varying the lattice constant,

151

Table 5.3: Interatomic potentials for CoSb$_3$ and the rattlers. Here r and θ are interatomic separation distance and bond angle. The parameters of the potentials are derived from *ab initio* calculations and RFT. The subscripts 1 and 2 denote the potentials for CoSb$_3$ and Ba(CoSb$_3$)$_4$, respectively.

Interaction	Potential Model	Parameters
Pair		
Co-Sb	$\varphi_\circ\{[1-\exp(-a(r-r_\circ))]^2-1\}$	$\varphi_{\circ,1} = 1.289$ eV, $a_1 = 1.175$ Å^{-1}, $r_{\circ,1} = 2.554$ Å $\varphi_{\circ,2} = 1.075$ eV, $a_2 = 1.286$ Å^{-1}, $r_{\circ,2} = 2.592$ Å
Co-Co	$\varphi_\circ\{[1-\exp(-a(r-r_\circ))]^2-1\}$	$\varphi_{\circ,2} = 0.273$ eV, $a_2 = 0.657$ Å^{-1}, $r_{\circ,2} = 4.569$ Å $\varphi_{\circ,2} = 0.025$ eV, $a_2 = 0.719$ Å^{-1}, $r_{\circ,2} = 4.636$ Å
Sb-Sb (short bond)	$\varphi_\circ\{[1-\exp(-a(r-r_\circ))]^2-1\}$	$\varphi_{\circ,1} = 2.24$ eV, $a_1 = 1.039$ Å^{-1}, $r_{\circ,1} = 2.888$ Å $\varphi_{\circ,2} = 1.002$ eV, $a_2 = 0.992$ Å^{-1}, $r_{\circ,2} = 2.993$ Å
Sb-Sb (long bond)	$\varphi_\circ\{[1-\exp(-a(r-r_\circ))]^2-1\}$	$\varphi_{\circ,1} = 1.380$ eV, $a_1 = 1.102$ Å^{-1}, $r_{\circ,1} = 3.025$ Å $\varphi_{\circ,2} = 0.91$ eV, $a_2 = 1.11$ Å^{-1}, $r_{\circ,2} = 3.004$ Å
Sb-Sb (between rectangles)	$\varphi_\circ\{[1-\exp(-a(r-r_\circ))]^2-1\}$	$\varphi_{\circ,1} = 0.702$ eV, $a_1 = 0.864$ Å^{-1}, $r_{\circ,1} = 3.473$ Å $\varphi_{\circ,2} = 0.431$ eV, $a_2 = 0.96$ Å^{-1}, $r_{\circ,2} = 3.474$ Å
Sb-Sb (between rectangles)	$\varphi_\circ\{[1-\exp(-a(r-r_\circ))]^2-1\}$	$\varphi_{\circ,1} = 0.527$ eV, $a_1 = 0.8$ Å^{-1}, $r_{\circ,1} = 3.746$ Å $\varphi_{\circ,2} = 0.228$ eV, $a_2 = 0.866$ Å^{-1}, $r_{\circ,2} = 3.847$ Å
Co-Sb (second neighbor)	$\varphi_\circ\{[1-\exp(-a(r-r_\circ))]^2-1\}$	$\varphi_{\circ,1} = 0.158$ eV, $a_1 = 0.676$ Å^{-1}, $r_{\circ,1} = 4.44$ Å $\varphi_{\circ,2} = 0.022$ eV, $a_2 = 0.751$ Å^{-1}, $r_{\circ,2} = 4.538$ Å
Co-Sb (third neighbor)	$\varphi_\circ\{[1-\exp(-a(r-r_\circ))]^2-1\}$	$\varphi_{\circ,1} = 0.196$ eV, $a_1 = 0.665$ Å^{-1}, $r_{\circ,1} = 4.51$ Å $\varphi_{\circ,2} = 0.102$ eV, $a_2 = 0.719$ Å^{-1}, $r_{\circ,2} = 4.636$ Å
Angular		
Co-Sb-Sb (1)	$\frac{1}{2}\varphi_\theta(\cos\theta-\cos\theta_\circ)^2$	$\varphi_\theta = 0.91$ eV, $\theta_\circ = 109.2°$
Co-Sb-Sb (2)	$\frac{1}{2}\varphi_\theta(\cos\theta-\cos\theta_\circ)^2$	$\varphi_\theta = 0.91$ eV, $\theta_\circ = 107.6°$
Filler-Host		
Ba-Sb (third neighbor)	$\varphi_\circ\{[1-\exp(-a(r-r_\circ))]^2-1\}$	$\varphi_\circ = 0.549$ eV, $a = 1.147$ Å^{-1}, $r_\circ = 3.48$ Å

a series of force constants were obtained. Providing the interatomic bond model, these force constants together with the corresponding bond length are then analyzed to obtain the anharmonic terms. Thereafter, the Morse potentials were fitted with these harmonic and anharmonic terms, and the results are listed in Table 5.3.

5.5 MD Simulation Procedure and G-K Autocorrelation

The phonon thermal conductivity $\boldsymbol{K}_p$ of unfilled and filled $CoSb_3$, is determined using molecular dynamics simulations together with G-K approach (described in chapter 1)[124].

Because of their cubic structures, the phonon thermal conductivities of $CoSb_3$ and filled structure ($ReCo_8Sb_{24}$) are isotropic. Due to the limit computation resource, to minimize the computation time, the MD simulations were mainly performed with a system consisting of $12 \times 3 \times 3$ cubic unit cells ($117 \times 27 \times 27$ Å^3). We assume the phonon transport in the x direction will not be affected by the small dimensions in the other two directions. This assumption was confirmed by running a simulation with $9 \times 9 \times 9$ cubic unit cells. The obtained results for the $9 \times 9 \times 9$ unit-cell system were found very close to the x-direction results for the $12 \times 3 \times 3$ unit-cell system. The simulations with even larger systems, e.g., $15 \times 4 \times 4$ system, produced very similar results, indicating the size effects were minor for a $12 \times 3 \times 3$ system. All the simulations were performed at 300 K and the time step was chosen as 4 fs.

153

The Verlet leapfrog algorithm was adopted for the calculation, while the Nose-Hoover thermostat and the Berendsen barostat were used to control the system temperature and pressure. The system was first simulated in a NPT (constant number of atoms, pressure and temperature) ensemble for 100-200 ps until it reached a free-standing state at the desired temperature, then it was switched into a NVE ensemble and ran another 100 ps to reach the the equilibrium state. Thereafter, 3000 ps raw heat current data were obtained for the calculation of HCACFs. The resulted HCACFs were then directly integrated and the phonon conductivities were set as the average values in the stable regime of the integral.

5.6   Effects of Fillers

Figure 5.7 shows the time evolvement of the predicted phonon conductivity of $CoSb_3$ at $T = 300$ K, using the modified force field (model C) developed by Feldman and Singh [123]. This force field leads to a k_p of 6.3 W/m-K. This value is lower than the experimental results (k_p of between 8 and 11 W/m-K)[114, 127, 12]. This lower value might be due to the overestimation of Grüneisen parameter, which is calculated as $\gamma_G = 1.1$ and is higher than the experimental value [127] $\gamma_G = 0.95$. By adding the Ba-Sb potential fitted with the scanned energy surface, the phonon conductivity of fully-filled $Ba(CoSb_3)_4$ is also calculated and is shown in Fig. 5.7. It is surprising that the predicted k_p of $Ba(CoSb_3)_4$ reaches 10 W/m-K, which is even higher than that of pure $CoSb_3$. This directly contradicts the traditional "rattler" idea that the filler's random "rattling" movement strongly scatters phonons and results in a much lower
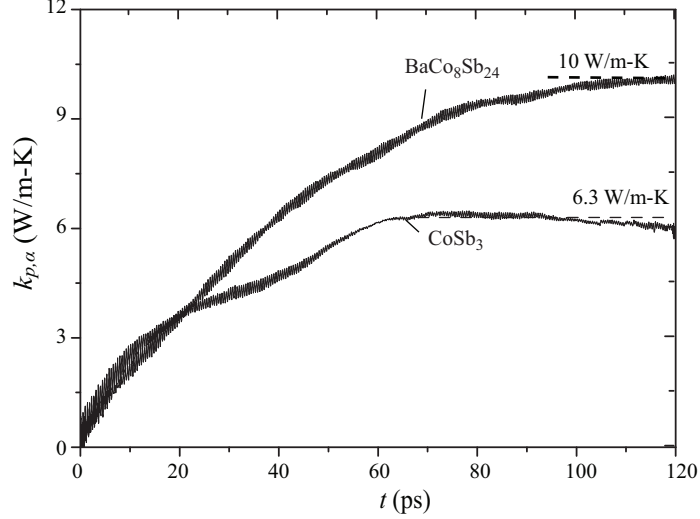
Figure 5.7: Evolvement of predicted variation of the phonon conductivity of $CoSb_3$ and $Ba(CoSb_3)_4$. In the MD simulation, the modified force field of Feldman and Singh[11] is used for the host, and the Sb-Ba potential is fitted with the energy surface .

phonon conductivity. To find out the reason for this increase in phonon conductivity, we calculated the elastic properties of $Ba(CoSb_3)_4$ using the above force field. After the Ba insertion, the bulk modulus E_p increases from 99.2 GPa to 116.8 GPa and c_{11} increases from 203 GPa to 235 GPa. These changes suggest that the creation of a strong Ba-Sb bond makes the lattice more rigid. According to the Slack relation (Eq. 3.10), $k_p \propto T_D^3 \propto E_p^{3/2}$, the change in elastic properties may result in 25% increase in the phonon conductivity. At the same time, the insertion of Ba atoms adds some parallel pathes for phonon transport, i.e., some phonons may pass through Ba-Sb bonds rather than propagate around the cage.

According to Fig. 5.5, we believe that the phonon conductivity of the fully-filled $Ba(CoSb_3)_4$ skutterudite should be lower than that for the empty structure, but this
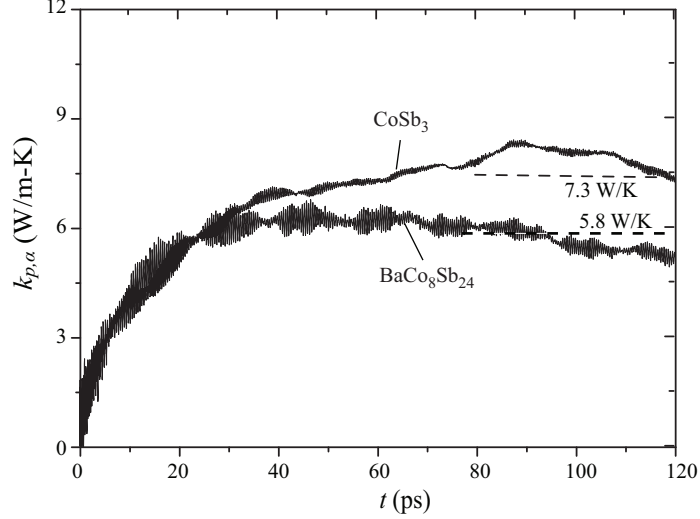
Figure 5.8: Predicted variation of the phonon conductivity of $CoSb_3$ and $Ba(CoSb_3)_4$ with respect to the correlation time. In the MD simulation, the force fields developed on the basis of DFT and RFT are used.

decrease is due to the bond change resulting from the presence of Ba atoms. To confirm this, we replaced the force fields for the host with those developed in the preceding sections on the basis of DFT and RFT (shown in Table 5.3) in the MD simulation. Figure 5.8 shows the predicted evolvement with these new potentials, at $T = 300$ K. The results support the suggestion that the filler "softens" the host bonds and suppresses the phonon transport.

We find that the filling effects can be estimated by the Slack relation 3.10. Since T_D is proportional to the cutoff frequency $f_{A,max}$ of the acoustic branches, by ignoring the changes in the Grüneisen parameter, we have

$$\frac{k_{p,\mathrm{Ba(CoSb_3)_4}}}{k_{p,\mathrm{CoSb_3}}} \simeq \left[\frac{f_{A,max,\mathrm{Ba(CoSb_3)_4}}}{f_{A,max,\mathrm{CoSb_3}}}\right]^3. \tag{5.2}$$

As approximation, we use the average cutoff frequency for the three acoustic branches.

156

According to Fig. 5.5, $f_{A,max,Ba(CoSb_3)_4} \simeq 1.0$ THz and $f_{A,max,Ba(CoSb_3)_4} \simeq 1.5$ THz, therefore, $k_{p,Ba(CoSb_3)_4}/k_{p,CoSb_3} \simeq 0.3$. This simple method also works fine for Sr-filled Ge clathrate and predicts the ratio of $k_{p,Sr_6Ge_{46}}/k_{p,Ge_{46}} \simeq [\frac{(80+45\times 2)}{3}/30] = 0.15$ (here we have used frequency in cm^{-1}). This value is in a good agreement with the MD predicted ratio[128] of 0.12.

5.7   Partial Filling

It has been observed that a relatively small concentration of a filler can cause relatively large decrease in phonon conductivity of skutterudites [114, 115, 129]. In addition, the largest decrease in the phonon conductivity is achieved for the partially-filled skutterudites rather than the fully-filled structures [114, 115]. If this reduction in phonon conductivity is due to the scattering by "rattlers", then we expect the phonon conductivity to decrease monotonically with increasing filler concentration. However, observations show there exists an optimal filling fraction in reducing the phonon conductivity [114, 115, 129]. Moreover, the room-temperature phonon conductivity of some partially filled skutterudites[129], e.g., $Ce_yFe_xCo_{4-x}Sb_{12}$, is almost independent of the filling fraction when the filling fraction is larger than 0.2. Nolas et al. [114] argued that a point-defect-type phonon scattering effect, due to the partial, random distribution of fillers in the voids, as well as the "rattling" effect of the filler ions, results in the scattering of a larger spectrum of phonons than in the case of full filling.

As discussed in previous sections, the filler is strongly coupled with the host

and the role of filler in reducing the phonon conductivity is more likely to change the surrounding bonds, instead of being a "rattler". It is reasonable to treat the fully-filled skutterudite as a new compound which has a lower phonon conductivity. Therefore, the partially-filled skutterudites can be thought of as solid solutions of completely filled and unfilled components, e.g., the partially-filled $Ba_x(CoSb_3)_4$ can be considered as solid solutions of $Ba(CoSb_3)_4$ and $\square(CoSb_3)_4$. Thus, the preminant mass fluctuation scattering is between Ba and $\square$. Similar ideas for $Ce_yFe_xCo_{4-x}Sb_{12}$ have been proposed by Meisner et al. [115].

We compared the experimental phonon conductivity[12] of $Ba_x(CoSb_3)_4$ with that predicted using the point defect scattering theory[130, 131, 115]. For high defect concentration, the phonon conductivity limited by the point defects scattering $k_{p,d}$ can be given by

$$k_{p,d} = k_B/[4\pi u_{p,g,A}(a_1\tau_{p-p})^{1/2}], \tag{5.3}$$

where τ_{p-p} is the relaxation time for interphonon scattering, and $u_{p,g,A}$ is average phonon group velocity. The relaxation time for interphonon scattering can be estimated from the room-temperature thermal conductivity of empty $CoSb_3$ crystal $k_{p,CoSb_3} = 10$ W/m-K, i.e.,

$$\begin{aligned}\tau_{p-p} &= k_B^2 T_D/(2\pi^2 u_{p,g,A}\hbar k_{p,CoSb_3}) \\ &= \frac{(6n)^{1/3}k_B}{2\pi^{4/3}k_{p,CoSb_3}}, \end{aligned} \tag{5.4}$$

where n is the atomic number density. This yields $\tau_{p-p} = 6.54 \times 10^{-16}$ s. The parameter a_1 is the coefficient for the Rayleigh-type point defect scattering rate,

which is given by $a_1 = V_c a_s / (4\pi u_{p,g,\mathrm{A}}^3)$. Here, V_c is the unit cell volume and a_s is the scattering parameter. For impurity atoms on a single atom site, $a_s = \sum f_i (1 - M_i / \langle M \rangle)^2$, where $\langle M \rangle = \sum f_i M_i$, f_i is the fractional concentration of impurity i, and M_i is its mass. The scattering parameter for a compound $\mathrm{Re}_u \mathrm{M}_v \mathrm{X}_w$, denoted as $a_s(\mathrm{Re}_u \mathrm{M}_v \mathrm{X}_w)$, is given by [132, 115]

$$
\begin{aligned}
a_s(\mathrm{Re}_u \mathrm{M}_v \mathrm{X}_w) &= \frac{u}{u+v+w}\left(\frac{M_{\mathrm{Re}}}{M_m}\right)^2 a_s(\mathrm{Re}) + \frac{v}{u+v+w}\left(\frac{M_{\mathrm{M}}}{M_m}\right)^2 a_s(\mathrm{M}) \\
&+ \frac{w}{u+v+w}\left(\frac{M_{\mathrm{X}}}{M_m}\right)^2 a_s(\mathrm{X}),
\end{aligned}
\tag{5.5}
$$

where $M_m = (u M_{\mathrm{Re}} + v M_{\mathrm{M}} + w M_{\mathrm{X}})/(u+v+w)$. For solid solution of $[\mathrm{Ba}(\mathrm{CoSb}_3)_4]_x$ $[\square(\mathrm{CoSb}_3)_4]_{1-x}$, Re $= (\mathrm{Ba}, \square)$, M $= \mathrm{Co}$, and X $= \mathrm{Sb}$. Therefore, $a_s(\mathrm{Re}_u \mathrm{M}_v \mathrm{X}_w) = 0.095x(1-x)$. According to Eq. (5.3) and using[127] $u_{p,g,\mathrm{A}} = 2934$ m/s, the thermal resistivity due to the point defects scattering is $k_{p,\mathrm{d}}^{-1} = 0.745[x(1-x)]$ m-K/W. According to the Matthiessen rule[124], the overall phonon conductivity $k_p(\text{solution})$ of the solution $[\mathrm{Ba}(\mathrm{CoSb}_3)_4]_x$ $[\square(\mathrm{CoSb}_3)_4]_{1-x}$ is given by

$$
k_p^{-1}(\text{solution}) = x k_{p,\mathrm{Ba}(\mathrm{CoSb}_3)_4}^{-1} + (1-x) k_{p,\mathrm{CoSb}_3}^{-1} + k_{p,d}^{-1}.
\tag{5.6}
$$

The variation of predicted overall phonon conductivity $k_p(\text{solution})$ of $\mathrm{Ba}_x(\mathrm{CoSb}_3)_4$ with respect to the filling fraction (at $T = 300$ K) is shown in Fig. 5.9, together with the experimental results [12]. In this calculation, both $k_{p,\mathrm{Ba}(\mathrm{CoSb}_3)_4}$ and k_{p,CoSb_3} are from the MD simulations. The overall agreement between the calculated values and the experimental results is fairly good. Figure 5.9 also shows that $k_{p,\text{solution}}$ is not very sensitive to the filling fraction x when $0.2 < x < 0.8$, which is partially due to the low phonon conductivity of $\mathrm{Ba}(\mathrm{CoSb}_3)_4$. Figure 5.9 shows the minimum
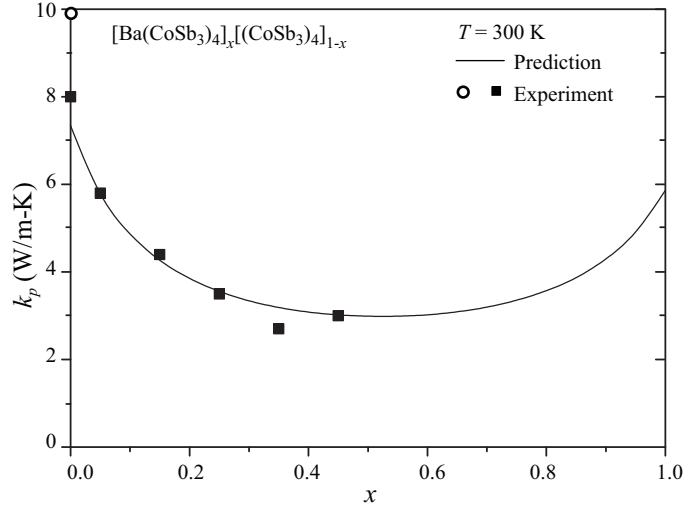
Figure 5.9: Variation of predicted phonon conductivity of $Ba_x(CoSb_3)_4$ (at $T = 300$ K), with respect to the filling fraction. The experimental results from Chen et al. [12] are also shown.

value does not occur exactly at $x = 0.5$, but depends on $k_{p,Ba(CoSb_3)_4}$ and $k_{p,CoSb_3}$. This solution model can also explain why the phonon conductivities of the filled skutterudites are independent of temperature at high temperatures and have lower peaks at low temperatures, since these are typical behaviors of solid solutions.

5.8 Summary and Conclusion

In this work, both the lattice vibrations and phonon transport in the empty $CoSb_3$ and filled $Ba(CoSb_3)_4$ skutterudites were investigated by performing first-principles calculations and MD simulations.

The filler-host coupling in filled $CoSb_3$ is found to be strong and its anharmonicity is minor. This contradicts with the traditional thought that fillers act as randomly-

moving "rattlers" that have weak bonds with the host. The lattice structures of both empty $CoSb_3$ and fully-filled $Ba(CoSb_3)_4$ are relaxed using DFT calculations. The comparison of the two relaxed structures shows that the insertion of Ba changes the lattice constants and almost all the bond lengths. The interatomic force constants for the two relaxed structure are also calculated using DFT and RFT. The results shows that the interatomic longitudinal force constant, except for Sb-Co bonds, is significantly affected by the presence of the Ba filler.

The MD simulations also shows that without changing the interatomic interactions for the host, the addition of filler can not reduce the phonon conductvity for filled skutterudites. This contradicts with the traditional "rattler" theory. The decrease in the phonon conductivity in the fully-filled skutterudites seems more likely due to the weaker bonds and lattice distortion resulting from the presence of the filler. This is confirmed by the MD simulations with the force field developed on the basis of DFT and RFT calculations. It is also found that the change in the acoustic cutoff frequency can be used to estimate the effects of filler on the phonon conductivity of skutterudites.

The results for the partially-filled $Ba_x(CoSb_3)_4$ skutteruidites may be better understood if they are considered as the solid solutions of the empty $CoSb_3$ and the fully-filled $Ba(CoSb_3)_4$. The predictions using the point defect scattering theory show a good agreement with the experimental results. This indicates the importance of alloying in reducing the phonon conductivity of skutterudites.

Chapter 6

Summary and Conclusion

6.1 Contribution

This work investigates the atomic-level thermal transport in compact,linked-cage, layered, and filled-cage crystals. The relationship between phonon conductivity and lattice structure has been studied theoretically and explained for understanding the nature of phonon transport in crystalline solids. Using this, we developed metrics and guidelines for the design of materials with desired thermal transport properties.

A comprehensive, multiscale approach which combines the *ab initio* calculations, MD/G-K, BTE, and the kinetic theory, has been developed for the investigation of thermal transport at atomic scale. Use of quantum mechanics makes it possible to avoid many assumptions required in other methods and provides more fundamental and unbias information at the atomic level. The obtained information also allows for examination of these assumptions and guides the construction of new models. MD/G-K, BTE and kinetic theory, are mainly of classical nature, but are efficient

for larger-scale system. The integration of these techniques allows for investigation of the bulk properties at the atomic scale, and for relating the micro structure to the macro phenomena.

This research is theoretical rather than experimental and the approach is through numerical simulation. However, experimental results are also intensively used. Challenges in both numerical results and experimental data are how to extract the information or relationship of interest and how to organize the information into a uniform framework. Therefore, analytic, theoretical modelling is used here to bridge this gap. Some significant contributions made here are summarized below:

- *Exploration of structural metrics of phonon conductivity.* An atomic structure-based model is developed for the understanding the relationship between the atomic structure and phonon transport in compact crystals at high temperatures. The thermal conductivity is predicted on the basis of the Debye temperature and the Grüneisen parameter from the atomic configuration of the structure. The elemental electronegativity and mass, and the arrangement of bonds are found to be the dominant factors in determining the phonon conductivity contribution from the long-range acoustic phonons. In linked-cage crystals, the phonon mean free path is limited by the cage-bridge structure and is equal to the cage size.

- *Development of force fields for MOFs, Bi_2Te_3, and skutterudites* Though the research on MOFs, Bi_2Te_3, and skutterudites are of academic and practical importance, the MD simulations for them are rare, due to the challenge in de-

163

veloping suitable classical force fields. Based on the *ab initio* calculations, we have developed the interatomic potentials for these structure. Comparison with available experimental results shows suitability of these potentials for investigating thermal transport in these structures.

- *Filler versus "rattler" role for filled skutterudites.* The filler in filled-cage crystals is traditionally thought of being a "rattler" with randomly "rattling" movements and strongly scattering phonons. As shown in Chapter 5, the coupling between the filler and host is strong and of minor anharmonicity, even at large displacements from the cage center. MD simulation shows that without filler-affected change in the host potentials, the insertion of a filler actually makes the structure more rigid and increases the phonon conductivity. The decrease in the phonon conductivity of a fully-filled skutterudite is due to softening of the host bonds, resulting from presence of filler. For partially-filled skutterudites, alloy effects are found to be very important in suppressing the phonon transport.

6.2   Future work

There are four natural extensions of the work presented here that should be pursued.

- The fitting of force field with energy surface scanned by the *ab initio* calculations, as used here, is not very efficient. The discrete points on the energy surface are few, and may not contain all the important information. To obtain dense energy surface, the calculations become formidable. In practice, not all

164

the points on the energy surface are necessary for obtaining good interatomic potentials. The manner in choosing the special energy surface points and extracting useful information on the interatomic potentials, is critical in both calculation efficiency and quality.

- Materials with nanostructures, e.g., supperlattice and nanowire, have exhibited great potentials in promising fields, such as thermoelectric and thermal insulation/conduction. Some atomic-level techniques developed in this work can also be applied to those nanostructures. It will be of great importance to understand the phonon and electron transport in these structures.

- The Green-Kubo fluctuation-dissipation method is normally used together with classical MD simulation. The challenge of finding suitable force fields for classical MD simulations limits the existing and future application of this method. The Green-Kubo method is based on the fluctuation-dissipation theory, which is also valid for system with quantum effects. In recent years, *ab initio* MD simulations, which avoid the fitting for the classical interatomic potentials, is attracting attentions. Combining the Green-Kubo method with *ab initio* MD simulations will greatly expands applications for both of these.

- This work focuses on bulk, single crystals. As well known, doping or alloying may significantly change both phonon and electron transport. This freedom makes it possible to improve performance of existing materials. The techniques developed here can also be used in exploring the structural metrics in these doped materials or alloys.

6.3   Outlook

Theoretical work is important, because it provides insight into the nature of physical phenomena. However, it can never replace experimental research. Experiments make no assumption, and new physical phenomena are always found in experiments. The challenge in experiments is how to explain the results and how to extract information of interest. The combination of theory and experiment will take advantage of both sides and benefit both sides.

Appendix A

Grüneisen Parameter for L-J

Oscillator

For L-J oscillators, the vibrational energy E_l and the mean atomic separation $\langle r_l \rangle$ of the motion with the principle quantum number l of this oscillator can be expressed as [52]

$$
\begin{aligned}
E_l &= \hbar\omega(l + \frac{1}{2}) - C_e\hbar^2\omega^2(l + \frac{1}{2})^2, C_e = \frac{5(m+n+3)^2}{48\varphi_\circ mn} \\
\langle r_l \rangle &= r_\circ + C_r r_\circ \hbar\omega(l + \frac{1}{2}), C_r = \frac{3(m+n+3)}{2\varphi_\circ mn},
\end{aligned}
\tag{A.1}
$$

where $-\varphi_\circ$ is the equilibrium potential energy.

The statistical mean vibration energy $E(\omega)$ and interatomic separation $\bar{r}(\omega)$ for frequency ω can then be given as [51]

$$
E(\omega) = F - T(\frac{\partial F}{\partial T})_V, F = -\hbar\omega \ln Z
\tag{A.2}
$$

$$
\begin{aligned}
\bar{r}(\omega) &= \frac{\sum_{l=0}^{\infty} \langle r_l \rangle e^{-E_l/k_\mathrm{B}T}}{\sum_{l=0}^{\infty} e^{-E_l/k_\mathrm{B}T}} \\
&= r_\circ + \frac{C_r r_\circ \hbar\omega}{2} + \frac{C_r r_\circ \hbar\omega}{e^{\hbar\omega/\hbar\omega} - 1},
\end{aligned}
\tag{A.3}
$$

where $Z = \sum_{l=0}^{\infty} e^{-E_l/k_{\mathrm{B}}T}$, is the partition function of the oscillator. Using the Debye approximation, the total vibrational energy E can be given as

$$
\begin{aligned}
E &= \int_0^{\omega_{\mathrm{D}}} E(\omega) D_p(\omega) \mathrm{d}\omega, \\
&\simeq E_o + 9N k_{\mathrm{B}} T x_D^{-3} f(x_D) - \\
&\quad 9 C_e N (k_{\mathrm{B}} T)^2 x_D^{-3} f_1(x_D) \\
f(x_{\mathrm{D}}) &= \int_0^{x_{\mathrm{D}}} \frac{x^3 \mathrm{d}x}{e^x - 1}, x_{\mathrm{D}} = T_{\mathrm{D}}/T \\
f_1(x_{\mathrm{D}}) &= \int_0^{x_{\mathrm{D}}} \frac{x^4(1 + e^x)\mathrm{d}x}{(e^x - 1)^2},
\end{aligned}
\tag{A.4}
$$

where $D_p(\omega)$ is the phonon density of states, and ω_{D} is the Debye frequency and E_{o} is the zero point energy.

Similarly, the mean interatomic separation r_e can be written as

$$
\begin{aligned}
r_e &= \frac{1}{3N} \int_0^{\omega_{\mathrm{D}}} D_p(\omega) \overline{r}(\omega) \mathrm{d}\omega \\
&= r_{\mathrm{o}} + r_1 + 3 k_{\mathrm{B}} T C_r r_{\mathrm{o}} \left(\frac{T}{T_{\mathrm{D}}}\right)^3 f_1(x_D),
\end{aligned}
\tag{A.5}
$$

where r_1 is the deviation due to the zero-point vibration, and r_2 is related to the thermal vibration and anharmonicity of the potential. $r_{e,o} = r_{\mathrm{o}} + r_1$ is the equilibrium separation at $T = 0$ K.

The Mie-Grüneisen equation of state is [51]

$$
p + \frac{\mathrm{d}U}{\mathrm{d}V} = \gamma \frac{E_v}{V},
\tag{A.6}
$$

where p is the pressure, U is the lattice potential energy, E_v is the total vibration energy excluding the zero-point energy E_{o}, and V is the volume.

For small perturbation,

$$
\frac{\mathrm{d}U}{\mathrm{d}V} \simeq B_{\mathrm{o}} \frac{V - V_{\mathrm{o}}}{V_{\mathrm{o}}} = 3 B_{\mathrm{o}} \frac{r - r_o}{r_{\mathrm{o}}}.
\tag{A.7}
$$

where B_{o} is the bulk modulus at zero temperature, and V_{o} is the initial volume. Since $B_o = U_o mn/(9V_o)$ [51] and $\gamma = \gamma'$ (the crystal contains only one bond type), by setting $r_{e,o} = r_o$, Eqs. (A.7), (A.4) and (A.5) give

$$\gamma' \simeq \gamma_{\mathrm{o}}'[1 + C_e k_{\mathrm{B}} T \frac{f_1(x_{\mathrm{D}})}{f(x_{\mathrm{D}})}], \ \gamma_{\mathrm{o}}' = \frac{m+n+3}{6}. \tag{A.8}$$

Appendix B

Thermal Conductivity

Measurement for MOF-5

B.1 Crystal Preparation

We synthesize large single cubic crystals by mixing 8.38 g $Zn(NO_3)2{\cdot}4H_2O$ (32.0 mmol) and 1.77 g terephthalic acid (10.7 mmol) dissolved in 100 mL DEF in a glass beaker and sonicating the mixture for 15 minutes. The solution is dispensed evenly into 20 scintillation vials (20-mL size) by using a plastic syringe equipped with a PTFE filter (Whatman, 0.45 μm pore size). The vials are then tightly capped and placed in an isothermal oven. The reactions are stopped after being heated at 368 K for 72 hours. The mother liquor in each vial is decanted while warm and the product is washed with fresh DEF (3 $\times$ 5 mL for each vial). In a typical batch as described above, 5-6 large single cubic crystals (size 1-2 mm) are obtained. The cubic crystals are confirmed to be MOF-5 by the coincidence of experimental PXRD pattern with

the simulated one and by examination of these crystals under an optical microscope [133, 15, 134].

After obtaining the large single cubic crystals, solvent-exchange is carried out to remove the high-boiling-point DEF in the crystals. The suitable crystals are collected in a 20-mL scintillation vial. After the DEF solvent is removed as clean as possible by using a pipette, this open vial is placed in a desiccator saturated with chloroform vapor, which slowly condenses into the vial and accumulates to 5 mm tall in 3 days. After the removal of the accumulated chloroform, two different methods are adopted for further solvent-exchange. One is to fill the vial with chloroform liquid and then cap it (direct addition of chloroform liquid). The solvent volume is replaced twice after a 1-day and a 2-day immersion respectively, and is kept at rest for another 2 days. The total time of chloroform-exchange of large MOF-5 single crystals is 3 days in desiccator and 5 days on bench. The other is to repeat the vapor diffusion exchange (slow condensation of chloroform vapor) 3 times in 7 days. The latter method is easier for obtaining clear crystals.

The effectiveness of exchanging DEF solvent is confirmed by the disappearance of characteristic amide carbonyl peaks in FT-IR spectra.

Table B.1 shows the characteristics of the crystal samples used in the conductivity measurement. Both the stored (old) solvent and the fresh solvent are purified and both solvent-exchange methods are used.

Table B.1: Characteristics of the samples used.

Sample	Size, mm^3	Chemical preparation
◇	$0.94 \times 1.13 \times 1.32$	old solvent, solvent-exchange: direct addition of chloroform liquid
□	$1.71 \times 1.17 \times 1.79$	fresh solvent, solvent-exchange: slow condensation of chloroform vapor
○	$1.33 \times 0.83 \times 1.50$	fresh solvent, solvent-exchange: slow condensation of chloroform vapor
△	$0.75 \times 1.13 \times 1.20$	fresh solvent, solvent-exchange: slow condensation of chloroform vapor

B.2 Thermal Conductivity Measurement

The thermal conductivity of the MOF-5 samples is measured based on the Fourier law [13], using the longitudinal, steady-state heat flow method.[135, 136] Since MOF-5 has a cubic structure, its thermal conductivity is isotropic and can be obtained by the measurement in only one direction.

Figure B.1(a) shows the apparatus used for the measurement and Fig. B.1(b) shows the thermal circuit diagram for the heat flow paths.

To avoid the formation of small cracks resulting from the adsorption of water vapor, the MOF-5 sample is prepared in a sealed airbag with filling prepurified nitrogen atmosphere. The dimensions of the sample are measured using a microscope. Two fine copper-constantan thermocouples (the diameters of the copper and constantan wires are 30 μm and 10 μm, respectively) are attached to the surface of the sample, using SE4422, a fast-drying thermally conductive adhesive produced by Dow Corning. The distance d between the thermocouples is also measured using the microscope. Here d is defined as the distance between the two thermocouple center points. Then the sample is mounted between a small heater and the copper heat sink of a cryostat, as shown in Fig. B.1(a).
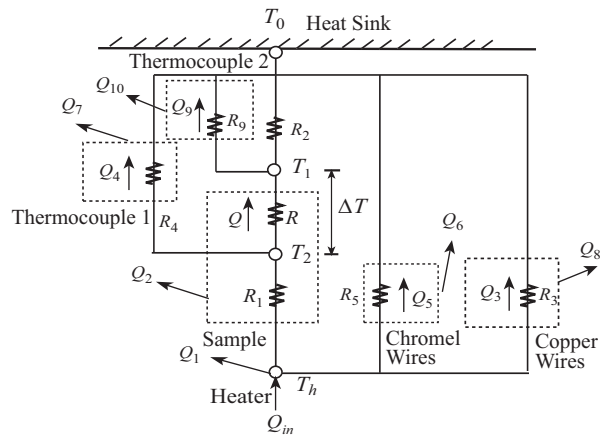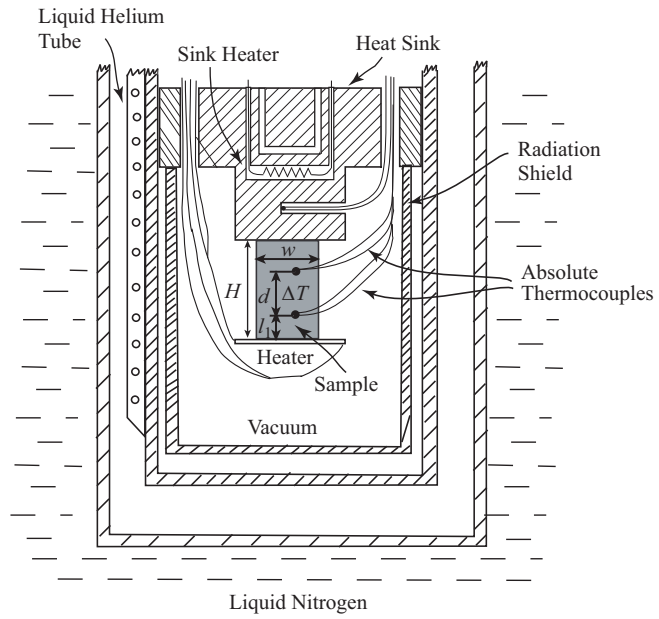
Figure B.1: (a) Apparatus for the measurement of thermal conductivity; (b) The thermal circuit diagram [13] for the heat flow path through the sample and various other paths.

173

Two copper wires with diameters of 30 μm are used for current input to the heater, and two chromel wires with diameters of 10 μm are used to measure the heater voltage. The lengths of the copper and chromel wires are all 25 cm (long enough to minimize the conduction loss). The cryostat is then evacuated until the pressure is reduced to 10^{-7} torr.

Liquid nitrogen is used to cool the sample from 300 K to about 100 K. Then liquid helium is used to cool the sample to 6 K. Thereafter, the temperature of the sample is raised incrementally back to 300 K. The thermal conductivity is measured during the procedure. The cooling rate using liquid helium is fast and the resulting thermal stress may result in the formation of defects within the sample, which can affect the low temperature results.

The specification of the thermal conductivity involves two steps. First, at each predetermined temperature point, a 1 mA DC current is input into the heater. After 5 to 10 minutes (to allow for steady, stable readings), when the outputs of the thermocouples become stable, the input current J_h, the voltage $\triangle\varphi_h$ and the temperature difference ΔT are recorded. Second, the heat loss is measured. After finishing the first step, the sample is detached from the heat sink, and left suspended by thermocouple wires, while keeping the heater attached to its bottom surface. The sample is then placed back into the cryostat and the cryostat is evacuated again. The heat loss is measured at the same temperatures as in the first step. The input current of the heater is adjusted by trial and error to raise the temperature of the sample to the same average temperature measured in the first step. The current $J_{e,2}$ and voltage $\triangle\varphi_{h,2}$ of the heater are recorded and the heat loss Q_{loss} is calculated by $Q_{loss} = J_{e,2}\triangle\varphi_{h,2}$.

Then the thermal conductivity k_p is calculated by

$$k_p = \frac{(J_h \triangle \varphi_h - Q_{loss})d}{A \triangle T},$$ (B.1)

where A is the cross section area perpendicular to the heat flow.

B.3 Heat Loss Model

The heat loss generally takes a long time to measure, and sometimes such a measurement is challenging at low temperatures. It is more efficient to calculate the heat loss using a model. This model can also guide minimizing the error due to the heat loss.

From Fig. B.1(b), Q_{loss} is the summation of Q_1 to Q_8, i.e.,

$$Q_{loss} = \sum_{i=1}^{8} Q_i,$$ (B.2)

where Q_1 is the radiation heat loss from the heater surface, Q_2 is the radiation heat loss from the sample surface, Q_3, Q_4, and Q_5 represent the conduction through the copper wires (heater), thermocouple wires, and chromel wires, and Q_6, Q_7 and Q_8 are the radiation from the chromel wires, thermocouple wires and the copper wires (heater) surface.

We assume the temperature varies linearly along the surface. Then each Q_i ($i = 1, 2, ..., 8$) can be calculated from

$$Q_1 = \sigma \varepsilon_h A_h (T_h^4 - T_0^4), T_h = \frac{l_1(T_1 - T_2)}{d} + T_2$$

175

$$Q_2 = \sigma\varepsilon_s \int_0^{l_1+d} 2(w+l)((T_1 + \frac{(T_2-T_1)x}{d})^4 - T_0^4)\mathrm{d}x$$

$$Q_3 = 2k_{cu}\frac{\pi D_{cu}^2}{4}\frac{(T_h-T_0)}{l_{cu,h}}$$

$$Q_4 = k_{cu}\frac{\pi D_{cu}^2}{4}\frac{(T_2-T_0)}{l_{cu,s}} + k_{con}\frac{\pi D_{con}^2}{4}\frac{(T_2-T_0)}{l_{con,s}}$$

$$Q_5 = 2k_{ch}\frac{\pi D_{ch}^2}{4}\frac{(T_h-T_0)}{l_{ch,h}}$$

$$Q_6 = 2\sigma\varepsilon_{ch} \int_0^{l_{ch,h}} \pi D_{ch}\{[T_0 + \frac{(T_h-T_0)x}{d}]^4 - T_0^4\}\mathrm{d}x$$

$$Q_7 = \sigma\varepsilon_{cu} \int_0^{l_{cu,s}} \pi D_{cu}\{[T_0 + \frac{(T_2-T_0)x}{d}]^4 - T_0^4\}\mathrm{d}x +$$

$$\sigma\varepsilon_{con} \int_0^{l_{con,s}} \pi D_{con}\{[T_0 + \frac{(T_2-T_0)x}{d}]^4 - T_0^4\}\mathrm{d}x$$

$$Q_8 = 2\sigma\varepsilon_{cu} \int_0^{l_{cu,h}} \pi D_{cu}\{[T_0 + \frac{(T_h-T_0)x}{d}]^4 - T_0^4\}\mathrm{d}x, \qquad \text{(B.3)}$$

where σ is the Stefan-Boltzmann constant, A_h is the area of the heater, ε_h, ε_s, ε_{cu}, ε_{con}, and ε_{ch}, are the emissivities of the heater, sample, copper, constantan and chromel, respectively (all assumed constant). Also, k_{cu}, k_{con} and k_{ch} are the thermal conductivities of copper, constantan and chromel, respectively (all are temperature dependent). Here $l_{cu,h}$ and $l_{ch,h}$ are the lengths of the copper and the chromel wires connected to the heater, respectively, and $l_{con,s}$ and $l_{cu,s}$ are the lengths of the constantan and the copper wires of the thermocouples. Also, D_{cu}, D_{ch} and D_{con} are the diameters of the copper , the chromel and the constantan wires, respectively. The outputs of the thermocouples give the temperatures T_1 and T_2, T_0 is the temperature of the heat sink and the surroundings, and T_h is the temperature of the heater.

It is assumed that the effect of thermal expansion and the contact resistance are negligible, and that temperature varies linearly along the longitudinal direction. Based on the experimental data, the radiation through the transparent sample is

negligible (less than 1% of the total heat flow at 300 K).

Figure B.2 shows the ratio $Q_i/J_h \Delta \varphi_h$, as a function of ambient temperature T_0. The emissivities of the wires are fitted by measuring the thermal conductivities of the materials with a known thermal conductivity, for example, glass and teflon. For the emissivities, we have found 0.6 for the copper wires, 0.6 for the constantan wires, 0.6 for the chromel wires, and 1.0 for the heater. The emissivity of the sample is assumed to be 1.0.
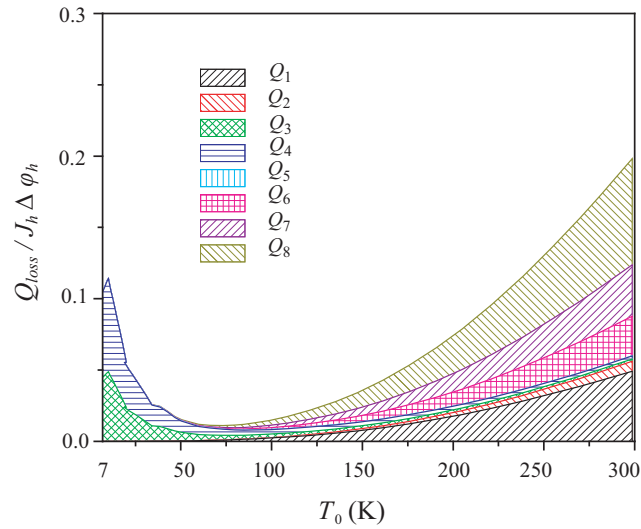

Figure B.2: Predicted contribution of the different heat losses as a function of ambient temperature, for a typical experiment. The geometric parameters in this heat loss model, are set as those for a typical sample at room temperature. The temperatures, T_1 and T_2, are set as the measured values at the ambient temperature T_0.

As shown in Fig. B.2, above 100 K, the total heat loss is dominated by surface radiation. The radiation effect increases sharply with increasing temperature and the total heat loss is up to 20% of the input power Q_{in} at 300 K. Among the radiation heat losses, Q_1 and Q_8 are the most significant, because the temperature of the heater is the

highest and the copper wires have the largest surface area. Between 40 K and 100 K, the total heat loss is relatively small. The conduction through the wires is significant below 40 K, due to the sharply increasing thermal conductivity of the copper with respect to decreasing temperature. The heat loss calculated by this model agrees well with the measured value.

References

[1] G. Herzberg, Molecuar Spectra and Molecular Structure IV. Constants of Diatomic Molecules, D. Van Nostrand company, Inc., 1979.

[2] G. A. Slack, Solid state Phys., Vol. 34, 1979.

[3] Z. Ni, Chemistry Department, University of Michigan, personal communication.

[4] B. L. Huang, A. J. H. McGaughey, M. Kaviany, Int. J. Heat Mass Tran. 50 (2007) 393.

[5] M. H. Francombe, Brit. J. Appl. Phys. 9 (1958) 415.

[6] J. O. Barnes, J. A. Rayne, Phys. Lett. 46A (1974) 317.

[7] J. O. Jenkins, J. A. Rayne, R. W. Ure, Phys. Rev. B 5 (1972) 3171.

[8] H. Rauh, R. Geick, H. Kohler, N. Nucker, N. Lehner, in Solid State Phys. 14 (1981) 2705.

[9] C. B. Satterthwaite, J. R. W. Ure, Phys. Rev. 108 (1957) 5.

[10] H.-W. Jeon, H.-P. Ha, D.-B. Hyun, J.-D. Shim, J. Phys. Chem. Solids 52 (1991) 579.

[11] J. L. Feldman, D. J. Singh, Phys. Rev. B 53 (1996) 6273.

[12] L. D. Chen, T. Kawahara, X. F. Tang, T. Goto, T. Hirai, J. S. Dyck, W. Chen, C. Uher, J. Appl. Phys. 90 (2001) 1864.

[13] M. Kaviany, Principles of Heat Transfer, John Wiley & Sons, Inc., New York, 2002.

[14] N. W. Ashcroft, N. D. Mermin, Solid State Physics, Thomson Learning, Inc., 1976.

[15] H. Li, M. Eddaoudi, M. O'Keeffe, O. M. Yaghi, Nature 402 (1999) 276.

[16] W. Kullmann, G. Eichhorn, H. Rauh, R. Geick, G. Eckold, U. Steigenberger, Phys. Stat. Sol.(b) 162 (1990) 125.

[17] K. N. R. Taylor, Brit. J. Appl. Phys. 12 (1961) 717.

[18] S. J. Youn, A. J. Freeman, Phys. Rev. B 63 (2001) 085112.

[19] P. Larson, Phys. Rev. B 68 (2003) 155121.

[20] T. J. Scheidemantel, C. Ambrosch-Draxl, T. Thonhauser, J. V. Badding, J. O. Sofo, Phys. Rev. B 68 (2003) 125210.

[21] M. Kim, A. J. Freeman, C. B. Geller, Phys. Rev. B 72 (2005) 035205.

[22] G. D. Mahan, in Solid State Phys. 51 (1997) 82.

[23] T. Schmidt, G. Kliche, H. D. Lutz, Acta Crystallogr. Sect. C: Cryst. Struct. Commun. 43 (1987) 1678.

[24] T. Kajitani, Y. Ono, Y. Miyazaki, M. Sluiter, L. Chen, T. Goto, Y. Kavazoe, 22nd International Conference on Thermoelectrics (2003) 81.

[25] A. Griesinger, K. Spindler, E. Hahne, International Journal of Heat and Mass Transfer 42 (1999) 4363.

[26] A. J. H. McGaughey, M. Kaviany, J. Comput. Theor. Nanos. 4 (2005) 896–927.

[27] P. Heino, J. Comput. Theor. Nanos. 4 (2007) 896–927.

[28] A. J. H. McGaughey, M. Kaviany, Phys. Rev. B 71 (2005) 184305.

[29] A. J. H. McGaughey, M. Kaviany, Int. J. Heat Mass Tran. 47 (2004) 1799.

[30] P. K. Schelling, S. R. Phillpot, P. Keblinski, Phys. Rev. B 65 (2002) 144306.

[31] J. Che, T. Cagin, W. Deng, W. A. Goddard, J. Chem Phys. 113 (2000) 68888.

[32] A. R. Leach, Molecular Modelling Principles and Applications, Addison Wesley Longman Limited, 1996.

[33] J. Callaway, Phys. Rev. 113 (1959) 1046.

[34] M. G. Holland, Phys. Rev. 132 (1963) 2461.

[35] A. J. H. McGaughey, M. Kaviany, Phys. Rev. B 69 (2004) 094303.

[36] S. G. Volz, G. Chen, Phys. Rev. B 61 (2000) 2651.

[37] Y. H. Lee, R. Biswas, C. M. Soukoulis, C. Z. Wang, C. T. Chan, K. M. Ho, Phys. Rev. B 43 (1991) 6573.

[38] C. L. Julian, Phys. Rev 137 (1965) A128.

[39] R. Berman, Thermal Conduction in Solids, Clarendon Press, Oxford, 1976.

[40] G. Herzberg, Molecuar Spectra and Molecular Structure II. Infrared and Raman Spectra of Polyatomic Molecules, D. Van Nostrand company, Inc., 1945.

[41] J. P. Biersack, J. F. Ziegler, Nucl. Instrum. Methods 194 (1982) 93.

[42] I. Feranchuk, A. Minkevich, A. Ulyanenkov, Eur. Phys. J. AP 19 (2002) 95–101.

[43] E. B. Wilson, J. C. Decius, P. C. Cross, Molecuar Vibrations: The Theory of Infrared and Raman Vibrational Spectra, D. Van Nostrand company, Inc., 1955.

[44] J. Paolini, J. Comput. Chem. 11 (1990) 1160–1163.

[45] L. Pauling, The Nature of Chemical bonds, Cornell Universtiy Press, 1960.

[46] C. Kittel, Introduction to Solid State Physics, John Wiley & Sons Inc., New York, 1996.

[47] D. Sirdeshmukh, P. Krishna, K. Subhadra, J. Mater. Sci. 38 (2003) 2001–2006.

[48] R. Astala, S. M. Auerbach, P. A. Monson, Phys. Rev. B 71 (2005) 014112.

[49] M. T. Dove, Introduction to Lattice Dynamics, Cambridge University Press, Cambridge, 1993.

[50] R. Zallen, M. Slade, Phys. Rev. B 18 (1978) 5775–5798.

[51] A. R. Ruffa, J. Chem. Phys. 83 (1985) 6405.

[52] F. G. Mateo, J. Zuniga, A. Requena, A. Hidalgo, J. Phys. B: At. Mol. Opt. Phys. 23 (1990) 2771.

[53] H. Septzler, J. Phys. Chem. Solids 33 (1972) 1727.

[54] D. G. Cahill, S. K. Watson, R. O. Pohl, Phys. Rev. B 46 (1992) 6131.

[55] M. Eddaoudi, J. Kim, N. Rosi, D. Vodak, J. Wachter, M. O'Keeffe, O. M. Yaghi, Science 295 (2002) 469.

[56] O. M. Yaghi, M. O'Keeffe, N. W. Ockwig, H. K. Chae, M. Eddaoudi, J. Kim, Nature 423 (2003) 705.

[57] J. L. C. Rowsell, O. M. Yaghi, Microporous Mesoporous Mater. 73 (2004) 3.

[58] N. L. Rosi, J. Eckert, M. Eddaoudi, D. T. Vodak, J. Kim, M. O'Keeffe, O. M. Yaghi, Science 300 (2003) 1127.

[59] J. L. C. Rowsell, A. R. Millward, K. S. Park, O. M. Yaghi, J. Am. Chem. Soc 126 (2004) 5666.

[60] J. L. C. Rowsell, E. C. Spencer, J. Eckert, J. A. K. Howard, O. M. Yaghi, Science 309 (2005) 1350.

[61] A. I. Skoulidas, D. S. Sholl, J. Phys. Chem. B 109 (2005) 15760.

[62] R. W. Grimes, D. J. Binks, A. B. Lidiard, Phil. Mag. A 72 (1995) 650.

[63] Gaussian 98 (Revision A.11), M. J. Frisch, *et al.*, Gaussian, Inc., Pittsburgh PA, 2001.

[64] J. D. Gale, A. L. Rohl, Mol. Simulat. 29 (2003) 291.

[65] R. Chelli, G. Cardini, P. Procacci, R. Righini, S. Califano, A. Albrecht, Int. J. Heat Mass Tran. 113 (2000) 6851.

[66] B. Boulard, J. Kieffer, C. C. Phifer, C. A. Angell, J. Non-Cryst. Solids 140 (1992) 350.

[67] P. Boulard, D. Bougeard, J. Chem. Phys. B 105 (2001) 36.

[68] J. Sauer, J. Dobler, ChemPhysChem 6 (2005) 1706.

[69] D. Wolf, P. Keblinski, S. R. Phillpot, J. Eggebrecht, J. Chem. Phys. 110 (1999) 8254.

[70] P. Demontis, S. Spanu, G. B. Suffritti, J. Chem. Phys. 114 (2001) 7980.

[71] D. Frenkel, B. Smit, Understanding Molecular Simulation: From Algorithms to Applications, Academic Press, San Diego, 1996.

[72] J. M. Haile, Molecular Dynamics Simulation Elementary Methods, John Wiley & Sons Inc., New York, 1992.

[73] A. D. Nashif, D. I. G. Jones, J. P. Henderson, Vibration Damping, John Wiley & Sons, New York, 1985.

[74] D. A. McQuarrie, Statistical Mechanics, University Science Books, Sausalito, 2000.

[75] M. Roufosse, P. G. Klemens, Phys. Rev. B 7 (1973) 5379.

[76] G. P. Srivastava, The Physics of Phonons, Adam Hilger, New York, 1990.

[77] B. Wolfing, C. Kloc, J. Teubner, E. Bucher, Phys. Rev. Lett. 86 (2001) 19.

[78] Y. Touloukian, Thermalphysical Properties of Matter, Plenum, New York, 1970.

[79] A. J. H. McGaughey, M. Kaviany, Int. J. Heat Mass Tran. 47 (2004) 1783.

[80] J. Li, L. Porter, S. Yip, Mater. Res. Soc. Symp. Proc. 255 (1998) 139.

[81] V. A. Konstantinov, J. Low Temp. Phys. 122 (2001) 459.

[82] P. Jund, R. Jullien, Phys. Rev. B 59 (1999) 13707.

[83] C.-K. Loong, Phys. Rev. B 45 (1992) 8052.

[84] L. W. da Silva, M. Kaviany, C. Uher, Journal of Applied Physics 97 (2005) 114903.

[85] D. R. Lide, CRC Handbook of Chemistry and Physics, CRC Press, Boca Raton, 1992.

[86] K. Torizuka, H. Tajima, T. Yamamoto, Physical Reviw B 71 (2005) 193101.

[87] S. Duclos, K. Brister, R. Haddon, A. Kortan, F. Thiel, Nature 351 (1991) 6325.

[88] R. Yu, N. Tea, M.B.Salamon, D. Lorents, R. Malhotra, Phys. Rev. Lett. 68 (1992) 2050–2053.

[89] J. R. Wiese, L. Muldawer, J. Phys. Chem. Solids 15 (1960) 13.

[90] H. J. Goldsmid, Thermoelectric Refrigeration, Plenum, New York, 1964.

[91] D. M. Zayachuk, Semiconductors 31 (1997) 173.

[92] D. L. Rode, Semicond. Semimetals 10 (1975) 1.

[93] H. Kohler, Molecular Simulation 74 (1976) 591.

[94] H. Kohler, Molecular Simulation 73 (1976) 95.

[95] S. Baroni, A. D. Corso, S. de Gironcoli, P. Giannozzi, C. Cavazzoni, G. Ballabio, S. Scandolo, G. Chiarotti, P. Focher, A. Pasquarello, K. Laasonen, A. Trave, R.Car, N. Marzari, A. Kokalj, http://www.pwscf.org/, 2007.

[96] H. Rydberg, M. Dion, N. Jacobson, E. Schroder, P. Hyldgaard, S. T. Simak, D. C. Langreth, B. I. Lundqvist, Phys. Rev. Lett. 91 (2003) 126402.

[97] D. A. Broido, A. Ward, N. Mingo, Phy. Rev. B 72 (2005) 014308.

[98] R. R. Rao, A. Ramanand, Acta Cryst. A33 (1977) 146.

[99] B. L. Huang, M. Kaviany, J. Appl. Phys. 100 (2006) 123507.

[100] Z. Yao, J. S. Wang, B. Li, G. R. Liu, Phys. Rev. B 71 (2005) 085417.

[101] P. A. Walker, Proc. Phys. Soc. 76 (1960) 113.

[102] H. Kaburaki, J. Li, S. Yip, H. Kimizuka, J. Appl. Phys. 102 (2007) 043514.

[103] J. M. Ziman, Electrons and Phonons, Oxford University Press, Ely House, London W. 1, 1962.

[104] G. K. H. Madsen, D. J. Singh, Comput. Phys. Commun. 175 (2006) 67.

[105] P. Blaha, K. Schwarz, G. K. H. Madsen, D. Kvasnicka, J. Luitz, WIEN2k, An Augmented Plane Wave+Local Orbitals Program for Calculating Crystal Properties, Karlheinz Schwarz, Techn. Uniersitat Wien,Austria, 2001.

[106] J. P. Perdew, K. Burke, M. Ernzerhof, Phys. Rev. Lett. 77 (1996) 3865.

[107] E. O. Kane, Semicond. Semimetals 1 (1966) 75.

[108] Y. I. Ravich, B. A. Efimova, V. I. Tamachenko, phys. stat. sol. (b) 43 (1971) 11.

[109] S. K. Mishra, S. Satpathy, O. Jepsen, J. Phys.: Condens. Matter 9 (1997) 461.

[110] S. K. Mishra, S. Satpathy, O. Jepsen, J. Phys.: Condens. Matter 9 (1997) 461.

[111] J. P. Singh, Electronic and Optoelectrionic Properties of Semiconductor Structures, Cambridge University Press, Cambridge, 2003.

[112] S. Shigetomi, S. Mori, J. Phys. Soc. Jpn. 11 (1956) 915.

[113] R. T. Delves, A. E. Bowley, D. W. Hazelden, H. J. Goldsmid, Proc. Phys. Soc. 78 (1961) 838.

[114] G. S. Nolas, J. L. Cohn, G. A. Slack, Phys. Rev. B 58 (1998) 164.

[115] G. P. Meisner, D. T. Morelli, S. Hu, J. Yang, C. Uher, Phys. Rev. Lett. 80 (1998) 3351.

[116] B. Sales, MRS Bull. 23 (1998) 15.

[117] V. Keppens, D. Mandrus, B. C. Sales, B. C. Chakoumakos, P. Dai, R. Coldea, M. B. Maple, D. A. Gajewski, E. J. Freeman, S. Bennington, Nature 395 (1998) 876.

[118] X. Gonze, J. M. Beuken, R. Caracas, F. Detraux, M. Fuchs, G. M. Rignanese, L. Sindic, M. Verstraete, G. Zerah, F. Jollet, M. Torrent, A. Roy, M. Mikami, P. Ghosez, J. Y. Raty, D. C. Allan, Comput. Mater. Sci. 25 (2002) 478.

[119] X. Shi, W. Zhang, L. D. Chen, J. Yang2, Phys. Rev. Lett. 95 (2005) 185503.

[120] J. L. Feldman, D. J. Singh, I. I. Mazin, D. Mandrus, B. C. Sales, Phys. Rev. B 61 (2000) R9209.

[121] P. Ghosez, M. Veithen, J. Phus.: Condens. Matter 19 (2007) 096002.

[122] H. D. Lutz, G. Kliche, Phys. Status Solidi B 112 (1982) 549.

[123] J. L. Feldman, P. Dai, T. Enck, B. C. Sales, D. Mandrus, D. J. Singh, Phys. Rev. B 73 (2006) 014306.

[124] Kaviany, Heat Transfer Physics, Cambridge University Press, 2008.

[125] X. Gonze, Phys. Rev. B 55 (1997) 10337.

[126] X. Gonze, Phys. Rev. B 55 (1997) 10355.

[127] T. Caillat, A. Borshchevsky, J.-P. Fleurial, J. Appl. Phys. 80 (1996) 4442.

[128] J. Dong, O. F. Sankey, C. W. Myles, Phys. Rev. Lett. 86 (2001) 2361.

[129] D. T. Morelli, G. P. Meisner, B. Chen, S. Hu, C. Uher, Phys. Rev. B 56 (1997) 7376.

[130] P. G. Klemens, Phys. Rev. 119 (1960) 507.

[131] J. Callaway, H. C. von Baeyer, Phys. Rev. 120 (1960) 1149.

[132] G. A. Slack, Phys. Rev. 126 (1962) 427.

[133] M. Eddaoudi, J. Kim, N. Rosi, D. Vodak, J. Wachter, M. O'Keeffe, O. M. Yaghi, Science 295 (2002) 469.

[134] J. L. C. Rowsell, A. R. Millward, K. S. Park, O. M. Yaghi, J. Am. Chem. Soc. 126 (2004) 5666.

[135] G. K. White, Experimental Techniques in Low Temperature Physics, Clarendon Press, Oxford, 1968.

[136] J. S. Dyck, W. Chen, C. Uher, L. D. Chen, X. F. Tang, T. Hirai, Journal of Applied Physics 91 (2002) 3698.